Novel Single-Band and Multi-Band Bandstop Filters for Modern Wireless Communication Systems

by

Mahbubeh Esmaeili
B.Sc., Iran University of Sience and Technology, Tehran, Iran 2005
M.Sc., Isfahan University of Technology, Isfahan, Iran 2010

A Dissertation Submitted in Partial Fulfillment of the
Requirements for the Degree of

DOCTOR OF PHILOSOPHY

in the Department of Electrical and Computer Engineering

Novel Single-Band and Multi-Band Bandstop Filters for Modern Wireless Communication Systems

by

Mahbubeh Esmaeili
B.Sc., Iran University of Sience and Technology, Tehran, Iran 2005
M.Sc., Isfahan University of Technology, Isfahan, Iran 2010

Supervisory Committee

Dr. J. Bornemann, Supervisor
(Department of Electrical and Computer Engineering)

Dr. P. So, Departmental Member
(Department of Electrical and Computer Engineering)

Dr. Y. Shi, Outside Member
(Department of Mechanical Engineering)

Supervisory Committee

Dr. J. Bornemann, Supervisor
(Department of Electrical and Computer Engineering)

Dr. P. So, Departmental Member
(Department of Electrical and Computer Engineering)

Dr. Y. Shi, Outside Member
(Department of Mechanical Engineering)

ABSTRACT

The objective of this thesis is to introduce novel procedures and guidelines to design bandstop microwave filters for modern terrestrial and satellite wireless communication systems. Among all available microwave filter technologies, planar structures of microstrip and substrate integrated waveguide (SIW) are chosen, due to ease of fabrication, low profile, weight and manufacturing cost. Particularly, SIW structures are more attractive because they have a better insertion loss, quality factor, and power handling capability in comparison to their microstrip counterparts, and can also be easily integrated into other planar circuitries.

A comprehensive hybrid analytic-optimization method is developed to synthesize any single-band as well as multi-band bandstop coupling matrix. In this method, the location of reflection zeros (RZs) and the attenuations in stopbands can be determined in advance.

Several novel single-band, dual-band, and triple-band bandstop filters are designed using regular and ridged SIW resonators, in-line coupled singlet resonators, cross-coupled resonators, and bandstop stubs. The designed filters have fractional bandwidths up to 23% . Moreover, a tunable ridged SIW bandstop resonator and a tunable CPW resonator, etched into the top plate of the SIW transmission line, are

introduced. Combining these two resonators, a dual-band SIW filter is designed that permits one of its stopband to be tuned while another stopband is fixed.

All introduced filters in this thesis are verified by commercial electromagnetic software, analytic investigations using Matlab codes, and measurements.

Contents

List of Tables

List of Figures

Symbols and Abbreviations

3D	Three Dimensional
ADC	Analog to Digital Converter
BPF	Bandpass Filter
BSF	Bandstop Filter
BST	Barium-Strontium-Titanate
BW	Bandwidth
CDMA	Code Division Multiple Access
CPW	Coplanar Waveguide
CST	Computer Simulation Technology
DAC	Digital to Analog Converter
DC	Direct Current
GSM	Global System for Mobile
HTS	High-Temperature Superconductors
IEEE	Institute of Electrical and Electronics Engineers
IL	Insertion Loss
Im	Imaginary Part
LCP	Liquid Crystal Polymer
LMDS	Local Multipoint Distribution System

LNA Low Noise Amplifier

LPP Lowpass Prototype

LTCC Low Temperature Co-fired Ceramic

MEMS Microelectromechanical System

MMDS Multichannel Multipoint Distribution Service

MMIC Monolithic Microwave Integrated Circuit

Max Maximum

Min Minimum

NRN Nonresonating Node

PBG Photonic Bandgap

PCS Personal Communication Service

Q Quality Factor

RF Radio Frequency

RL Return Loss

RX Receiver

RZ Reflection Zero

SAW Surface Acoustic Wave

SIW Substrate Integrated Waveguide

SMA Sub-Miniature Version A

TE Transverse Electric

TL Transmission Line

TRL	Thru-Reflect-Line
TX	Transmitter
TZ	Transmission Zero
UE	Unit Element
UHF	Ultra High Frequency
UMTS	Universal Mobile Telecommunications System
WLAN	Wireless Local Area Network
WiMAX	Worldwide Interoperability for Microwave Access

ACKNOWLEDGEMENTS

I would like to express my sincere gratitude and appreciation to my supervisor, Dr. Jens Bornemann, for his great support, help, and patience during my PhD research. I learned a lot from him, scientifically and personally.

I would like to deeply thank my lovely family: my parents, sisters and brother, for their constant love, support, and encouragement, especially when I was studying abroad.

Last but not least, I would like to thank my wonderful colleagues and friends, Zamzam, Lisa, Jan, Qianqian, Mehdi, and Mahdieh, for all the nice moments and fruitful discussions.

To...

my lovely and precious mother and father, Mehri and Mojtaba, for their endless kindness and support,
my lovely sisters and brother, Maryam, Suri, and Mohammad, for their love and encouragement.

Chapter 1

Introduction

1.1 Applications of Microwave Filters

The term microwave is used to refer to the frequency range from 300 KHz to 300 GHz. As shown in Fig. 1.1, the microwave spectrum is divided into several frequency bands and each of them is used for a specific application. The microwave spectrum is employed by many wireless commercial and military services such as cellular communication systems, navigation, radar and radio astronomy. Especially, there is a fast growing trend toward wireless communication services including development of fourth and fifth generation of wireless mobile systems as well as multimedia and high bandwidth applications. In such a crowded spectrum, microwave filters are used as essential components in front ends of any communication systems, to discriminate desired frequency components from unwanted ones, Fig. 1.2.

Filters are classified as lowpass, bandpass, high-pass and band-reject filters, based on their frequency responses. Depending on the in-band and out-of-band specifications of a filter, microwave filters are categorized as maximally flat or Butterworth, all-pole or Chebyshev type I, Chebyshev type II, general Chebyshev or pseudo-elliptic, elliptic or Cauer, and Bessel filters. While Butterworth filters have the best uniform amplitude responses, Bessel filters are well-known for their linear phase characteristics.

Generally, a microwave filter is described by its center frequency, bandwidth, return loss (attenuation in bandstop filters), group delay specification and location of transmission zeros (reflection zeros in bandstop filters). When designing a microwave filter, some features should be considered according to the required applications such

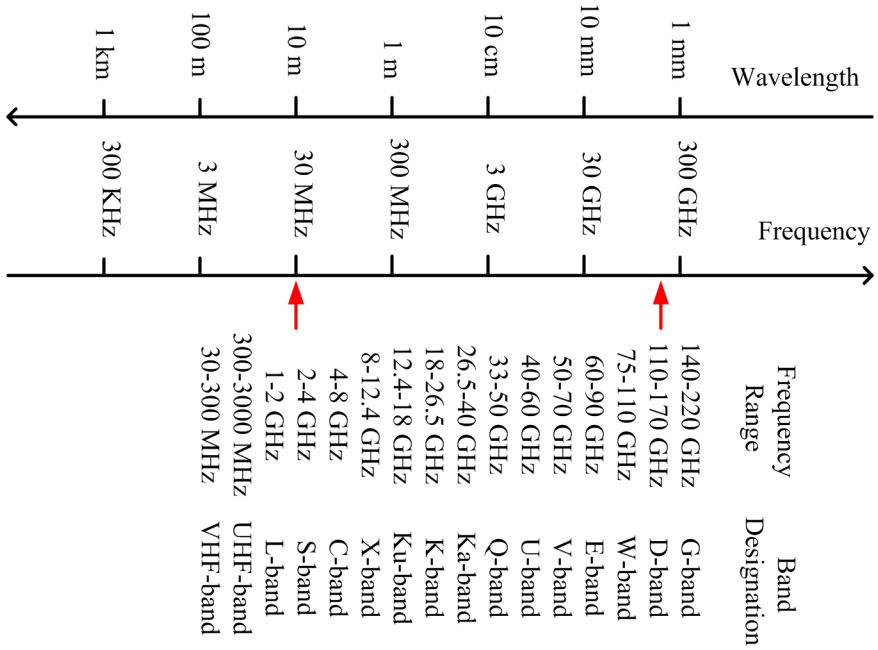

Figure 1.1: RF/Microwave spectrum.

as volume and mass, quality factor, spurious modes, manufacturing cost. Less obvious factors should be also taken into account such as tuning range, effect of unwanted coupling, sensitivities to coupling structures and power handling requirements. A trade-off between some filter specifications is always necessary in filter design procedures. For instance, for normal metallic cavities (non super conducting material), the quality factor Q is calculated by [1]

$$Q = kb\sqrt{f} \tag{1.1}$$

where b is the height of the cavity, f is the resonant frequency, and k is a constant and different for any given type of resonator. It is obvious that a higher order mode has a larger quality factor but at the cost of increasing the volume and spurious complexity. Higher quality factors are also achievable for fundamental resonant modes by increasing the overall size of the filter.

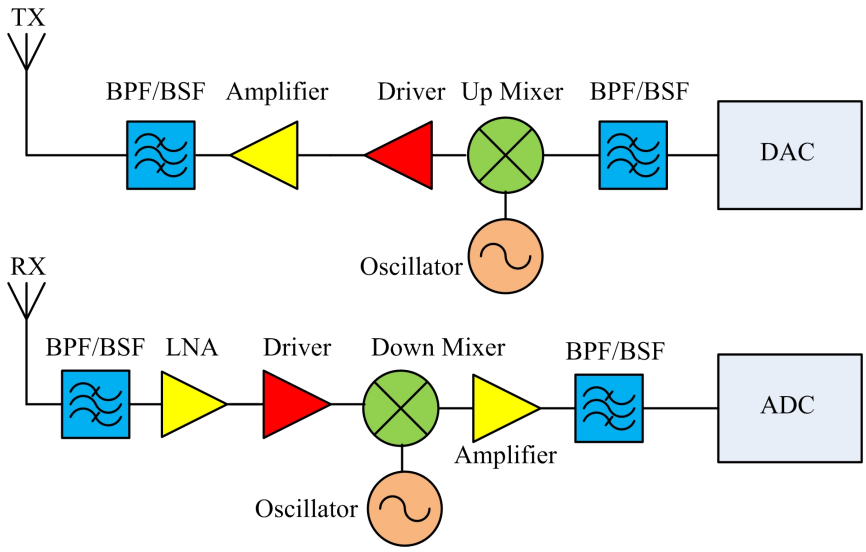

Figure 1.2: A general bock diagram for front ends of a typical wireless transmitter and receiver with bandpass (BPF) and bandstop (BSF) filters.

1.2 History of Microwave Filters

Microwave filter studies began in the years prior to world war II, and it was widely developed during the war and the years immediately after. The image parameter method, as one of the main two filter design methods, was developed in 1930s to design lowpass lumped filters used in radio and telephony, using ABCD parameters, though not in matrix form [2]. In the image parameter method, several two-port networks with equal terminal impedances are cascaded to realize passband and stopband specifications. Although the design process is simple, an arbitrary frequency response may not be possible.

The insertion loss method, the second main filter design approach, gives more degrees of freedom by a systematic way to synthesize desired transfer functions. This method was originally presented by Norton's constant-resistance filter pairs in 1937 and developed independently by Cocci (1938–1940), Darlington (1939), Cauer (1939–1941), and Piloty (1931–1941) [2].

In the 1950s, several laboratories were engaged in developing new microwave filter designs with emphasis on waveguide cavity filters, broad-band lowpass, bandpass coaxial filters, narrow-band tunable coaxial filters, based on lowpass lumped element network synthesis and insertion loss methods.

The direct coupled cavity filter theory, in contrast to quarter-wavelength coupled

resonators, was one of the main contributions of the Stanford Research Institute [3], which results in wider bandwidth by connecting resonators directly via capacitive or inductive elements.

One of the most important developments, during these years, were Richard transformations introduced in 1948 [4], and Kuroda's identities presented for the first time in Japanese language in 1955 [2], which enable designers to apply all well-developed lumped element theory to distributed circuits. Richard transformations are used to convert lumped elements to transmission line sections, and Kuroda's identities use redundant transmission line sections to make more practical and feasible filters by separating transmission line stubs physically, transforming shunt stubs to series stubs or vice versa and changing impractical characteristic impedances to practical ones.

The first cross-coupled resonator filter was designed in 1948 to produce multiple paths between input and output, resulting in transmission zeros (TZs) in the transfer function or group delay flattening [2]. Most developments in generalized and complex filter designs took place after 1965.

Many of the efforts to develop a wide range of microwave filters before 1970s are presented by Matthaei, Young and Jones in [5], including fundamental concepts, techniques, data and theories which the design process is based on. Especially, some data for maximally flat, Butterworth and Chebyshev lowpass filters are tabulated in handbook form.

1.3 Advanced Microwave Filters

Advanced filter design methods emerged with the first satellite telecommunication systems in the early 1970s and continued with the development of more wireless communication networks. Limited and crowded usable spectrum results in demanding filters with more stringent specifications such as linear in-band response and sharp transition from in-band to out-of-band using arbitrary placed TZs. The advances in the synthesis of microwave filters, to satisfy these new demands, can be categorized in two main ways.

The first approach enhanced the old classical filter design techniques. Almost all classical techniques, developed by the early 1970s, are based on Cohn's paper in the late 1950s [3]. This classical approach is based on the extraction of electrical elements, such as lumped inductors, lumped capacitors and transmission line section values, for a specific polynomial filtering function, followed by appropriately associating these pa-

rameters with the filters' physical dimensions. Final tuning or optimization is usually necessary. These classical approaches were appropriate and adequate for the available technologies and applications needed at the time, although they were not successful enough for stringent filter specifications with more complicated structures. Therefore, researchers tried to introduce more accurate and enhanced equivalent circuits, by including the electromagnetic behavior of the structure's elements. References [6–10] are good examples of these efforts.

The second approach introduced the coupling matrix synthesis method [11]. The coupling matrix is a representation of a network that can be used as an alternative to one-by-one electrical element extraction methods. In this technique, each element of the matrix is associated with an individual physical parameter of the filter. The effect of frequency-dependent coupling matrix elements, as well as lossy and dispersive resonators, can be simply accommodated in the coupling matrix while synthesizing it for a given filter performance. Therefore, different features can be assigned to different matrix element if the filter comprises different technologies [12].

The two main advanced filter design approaches, mentioned above, are well accompanied by new mathematical methods for synthesizing general transfer functions with arbitrary located TZs. To implement TZs, new configurations are also introduced in the filter design field including advanced cross-coupled and multi-mode resonators, modular filter blocks and extracted pole technique as well as new concepts such as nonresonating and detuned nodes.

In addition, full-wave electromagnetic (EM) simulators, based on numerical techniques in EM and implemented on powerful computers, are widely used in both advanced filter synthesis and optimization. Modern EM simulators enable designers, as accurately as possible, to make connections between equivalent circuit or coupling matrix elements and filters' physical parameters. Then electromagnetic optimization tools, included in these simulators, are used in the second step to compensate for limitations of the synthesis.

Advances in wireless communication systems not only affected and enhanced the filters' design methods, they dramatically developed new technologies. Depending on the microwave filter applications, different technologies are used. Military applications usually require wideband tunable devices which led to the development of wideband waveguide or coaxial resonators. Satellite communication systems need microwave filters with high selectively and linear phase. These requirements resulted in the development of dual-mode waveguide and dielectric resonator filters. Advanced

coaxial, dielectric resonator and superconducting filters are used for spreading cellular wireless base stations. Nowadays, cellular radio handsets, used by millions of people over the world, need very small filters with high selectivity, low loss and very low manufacturing cost which results in great advances in integrated ceramic, surface and bulk acoustic wave, microelectromechanical system (MEMS), and low temperature cofired ceramic (LTCC) filters. Table 1.1 summarizes filter technologies, for different frequency bands, with their typical applications.

Table 1.1: Filter technologies and their applications vs. frequency bands

Band	**UHF**	**L/S**	**C**	**X/Ku**	**Ka**
Technology	SAW Helical Dielectric Combline Planar Waveguide	Combline SAW Dielectric Planar HTS Waveguide	Dielectric Waveguide HTS Planar Combline	Dielectric Waveguide Planar	Waveguide Dielectric Planar
Application	Cellular Satcom	PCS Satcom MMDS	Satcom	Satcom	LMDS Satcom

1.4 Motivation for This Thesis

In the past decade, one of the areas which has attracted more attention, is bandstop filter design. Historically, bandstop filters have been less investigated by researchers in comparison to their bandpass counterparts. In addition, most of the realized bandstop filters are microstrip filters with narrow bandwidth. Combining new technologies and topologies to design bandstop filters with smaller size, wider stopband, wider passband and higher power is an attractive topic in the time of modern wireless systems [13].

Dual-band and multi-band bandstop filters are also captivating due to their capability to reject several frequency bands by using only one structure, resulting in reducing filter sizes and manufacturing costs. Currently, dual-band bandpass filters are used by GSM and CDMA mobile phones operating at 900 MHz and 1.8 GHz, as well as by WLAN networks, based on IEEE 802.11a/b/g standards, working at 2.4 and 5.2 GHz [14]. Triple-band bandpass filters are used by triple-band Universal Mobile Telecommunications System (UMTS) devices operating at 900, 1800, and 1900 MHz frequency bands in Europe. Likewise, North and South American devices work

at 800 or 950, 1800, and 1900 MHz frequencies. In addition, tri-band filters are used in WiMAX systems, operating at 2.3-2.7 GHz, 3.3-3.9 GHz and 5.15-5.85 GHz, in IEEE 802.16e standard [15]. In some applications, it is advantageous to design, e.g., a triple-bandstop filter to replace a dual-bandpass filter. In this case, more resonators might be needed at band edges, and similar performance characteristics, e.g. insertion loss, are obtained. Dual- and triple-bandstop filters can also be used to eliminate dual-band or triple-band wireless services where they are not desired.

Another interesting topic, in the advanced filter design area, is tunable filters which are in high demand in both wireless and satellite applications. For instance, using tunable filters enables operators to add new generation networks to their services. In addition, space and weight limitations cause serious constraints. By employing tunable filters, multi-band and multi-standard functions are accommodated to fit into one component. Likewise, reduced-size payload, hardware time sharing, multi-mode and multi-functional operation are the advantages of using tunable filters in modern satellite systems [16]. The majority of the conducted researches are on tunable bandpass microstrip filters, and tunable bandstop filters remain one of the attractive research fields.

In this research, we aim to introduce new advanced design methods for single-band and multi-band bandstop filters with improved features such as simplicity of the design and tuning process, less weight and manufacturing cost, bandwidth and power-handling improvement. We focus on the pseudo-elliptic bandstop filters in planar technologies including microstrip and substrate integrated waveguide (SIW) filters, due to their small size, low profile and fabrication cost. Especially, SIW filters are more attractive because they combine the advantages of high quality factor of waveguide filters with the low profile of microstrip filters, and they can be easily implemented within a planar circuitry.

Reconfigurable SIW bandstop filters are also investigated due to their influence on signal-to-noise ratio and interference rejection.

In this thesis, we will synthesis, simulate, prototype and measure some new microstrip and SIW single-band, dual-band and tri-band bandstop filters. In addition, a new dual-bandstop SIW filter is presented which permits one of its stopbands to be electronically tuned, using varactor diodes.

1.5 Thesis Contributions

The main contributions of this thesis are

- Developing a general coupling matrix synthesis technique for single-band or multi-band bandpass and bandstop pseudo-elliptic filters.
- Designing a triple-band bandstop SIW filter incorporating cross-coupled resonators.
- Introducing a dual-band bandstop filter employing in-line resonators and the nonresonating mode concept.
- Presenting a single-band ridged SIW bandstop filter based on partial-height resonating post in thick substrate.
- Designing a dual-band multi-mode SIW bandstop filter using bandstop stubs.
- Utilizing L- and T-shaped resonators to design a new wideband microstrip bandstop filter operating in X-band.
- Designing a ridged tunable SIW resonator, and an SIW dual-band bandstop filter with one electronically tunable stopband.

These contributions are reflected in the following peer-reviewed publications:

- M. Esmaeili, J. Bornemann, "Quasi-elliptic triple-stopband filter based on six cross-coupled SIW resonators," *IEEE Microw. Compon. Lett.*, Vol. 25, No. 12, pp. 802-804, 2015.
- M. Esmaeili, J. Bornemann, "Substrate integrated waveguide triple-passband dual-stopband filter using six cascaded singlets," *IEEE Microw. Compon. Lett.*, Vol. 24, pp. 439-441, 2014.
- M. Esmaeili, J. Bornemann, "Substrate integrated waveguide bandstop filter using partial-height via-hole resonators in thick substrate," *IET Microw. Antennas Propag.*, Vol. 9, pp. 1307-1312, 2015.
- M. Esmaeili, J. Bornemann, "Substrate integrated waveguide dual-stopband filter," *Microwave Opt. Technol. Lett.*, Vol. 56, pp. 1561-1563, 2014.

- M. Esmaeili, J. Bornemann, "Microstrip stopband filter using L- and T-shaped resonators," *Proc. Asia-Pacific Microw. Conf.*, pp. 1-3, 2015.

- M. Esmaeili, J. Bornemann, "Novel tunable bandstop SIW resonators and their application to design a dual-band bandstop filter with one tunable stopband," *IEEE Microw. Compon. Lett.*, submitted for publication.

Moreover, I contributed to a substrate integrated waveguide tunable phase shifter design.

- D. Formiga Mamedes, M. Esmaeili, J. Bornemann, "K-band substrate integrated waveguide variable phase shifter," *Proc. European Conf. Antennas Propag.*, pp. 1-4, 2016.

1.6 Thesis Outline

The outlines for each chapter are described as follows.

Chapter 1 contains an overall overview of microwave filters, their importance, application, history and recent advances. The thesis motivations and contributions are also presented in this chapter.

Chapter 2 provides a general coupling matrix synthesis method for single-band and multi-band bandstop filters.

Chapter 3 presents a dual-band and a triple-band bandstop filter based on nonresonating nodes and cross-coupled resonators, respectively. For both filters, their corresponding coupling matrices are extracted.

Chapter 4 describes the design process of a dual-band triple-mode and a single-band ridged SIW bandstop filter, based on the extracted pole technique. An equivalent circuit, properly describing the behavior of the ridged SIW filter, is also presented. In addition, this chapter describes how to design a single-band bandstop microstrip filter in X-band, with two TZs in the stopband and two reflection zeros (RZs) at the upper and lower passbands, using L- and T-shaped resonators.

Chapter 5 contains the general idea behind electronically tunable filters and presents two single-band and dual-band tunable bandstop filters in SIW technology.

Chapter 6 summarizes the results and findings presented in this thesis and presents possible future works regarding the analysis and design of advanced conventional or tunable bandstop microwave filters.

Chapter 2

Bandstop Coupling Matrix Synthesis

Direct-coupled and cross-coupled bandstop filters can be modeled by a coupling matrix that presents an one-by-one correspondence between the matrix's elements and the physical dimensions of the resonators. In this chapter, the general transversal coupling network, applicable to both bandpass and bandstop filters, is outlined. An optimization technique is also developed to synthesize single-band as well as multi-band bandstop filtering functions, with any arbitrary located reflection zeros (RZs).

2.1 Coupled-Resonator Networks and Coupling Matrices

The inter-resonator couplings in microwave filters are usually described by a coupling matrix which contains the coupling values between resonators that are assumed constant over the operating bandwidth of the filter. Fig. 2.1 shows a typical lowpass equivalent circuit of coupled-resonator networks. Circuit theory analysis techniques are required to extract the coupling matrix of this two-port network.

Applying Kirchhoff's Current Law to the circuit shown in Fig. 2.1, the loop currents, $[I]_{N1}$, are governed by the following matrix equation [17]

$$[\Omega U - jR + M][I] = [A][I] = -j[e] \tag{2.1}$$

Here, R_{NN} is a matrix whose non-zero elements are $R_{11} = R_1$ and $R_{NN} = R_2$ (Fig.

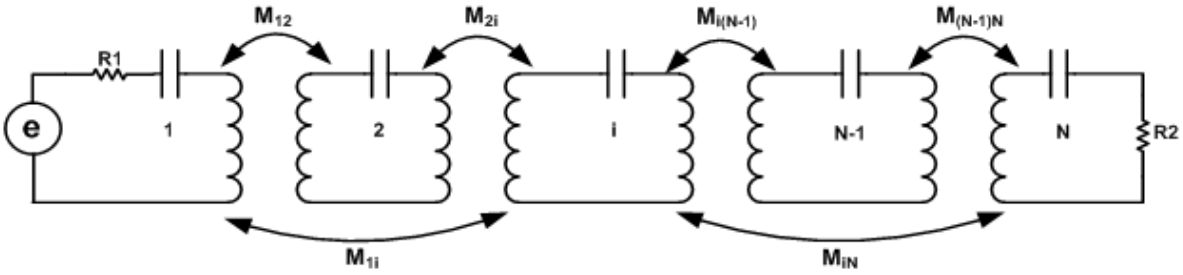

Figure 2.1: General configuration of coupled-resonator networks.

2.1). M_{NN} is a symmetric coupling matrix, containing the coupling coefficients M_{pq}, and $[e]_t = [1, 0, 0, ..., 0]_{1\times N}$ is the excitation vector, where t is the transposition operator. The diagonal elements of the coupling matrix show the offset of the resonant frequency of each resonator, and off-diagonal elements represent the coupling values between adjacent and non-adjacent resonators. The normalized frequency Ω is used to indicate the lowpass characteristic of the circuit. A lowpass-to-bandpass frequency conversion is defined as below to convert a lowpass response to a bandpass one

$$s = j\Omega = \frac{f_0}{BW}\left(\frac{f}{f_0} - \frac{f_0}{f}\right) \tag{2.2}$$

where f_0 and BW are center frequency and bandwidth of the bandpass filter, respectively. Matrix U_{NN} is a diagonal matrix whose element are unity if all nodes are resonators as in conventional direct- and cross-coupled filters. The scattering parameters of this circuit can be calculated by employing conventional circuit theory [17]

$$S_{21} = -j2\sqrt{R_1 R_2}\left[A^{-1}\right]_{N1} \tag{2.3}$$

$$S_{11} = 1 - 2R_1 I_1 = 1 + j2R_1\left[A^{-1}\right]_{11} \tag{2.4}$$

where exponent -1 denotes the matrix inversion operator, and $[A]$ is $[\Omega U - jR + M]$.

2.2 Coupling Matrix Extraction

Reflection, S_{11}, and transmission, S_{21}, coefficients of any filter are determined by rational functions as

$$S_{11} = \frac{F(s)}{E(s)} \qquad S_{21} = \frac{P(s)}{\epsilon E(s)} \tag{2.5}$$

where $E(s)$, $F(s)$ and $P(s)$ are polynomials of order N , N , and N_Z, respectively. N is the order of the filter and N_Z is the number of finite TZs that is smaller than or equal to N.

There are two main approaches to synthesize a coupling matrix for a filter if its responses are know in the form of rational functions, as presented in (2.5). The first method is based on direct optimization of a coupling matrix's elements until it meets the desired filtering function specifications. The second approach is a combination of analytic and optimization techniques. In this method, first, a transversal $(N+2) \times (N+2)$ coupling matrix is synthesized satisfying the desired filtering function, and then this transversal coupling matrix is converted to a folded one, by optimization techniques, to match the filter topology while representing the same responses. These two approaches are outlined in this section.

2.2.1 Coupling Matrix Extraction Based on Optimization

A coupling matrix can be directly synthesized by optimization techniques if the filtering function is known in advance. Among all optimization algorithms, gradient methods are very powerful algorithms for finding global and local minima using both cost functions and their gradients [18]. The cost function below can be used for optimizing the location of TZs and RZs as well as return loss levels [19]

$$\begin{aligned} K = & \sum_{i=1}^{N} \left|S_{11}\ (s_{zi})\right|^2 + \sum_{i=1}^{N_z} \left|S_{21}\ (s_{pi})\right|^2 \\ & + \left(\left|S_{11}(s=-j) - \frac{\epsilon}{\sqrt{1+\epsilon^2}}\right|\right)^2 + \left(\left|S_{11}(s=j) - \frac{\epsilon}{\sqrt{1+\epsilon^2}}\right|\right)^2 \end{aligned} \tag{2.6}$$

where s_{zi} and s_{pi} are locations of RZs and TZs in the filtering function. The parameter ϵ is also related to return loss, RL, by

$$\epsilon = \frac{1}{\sqrt{10^{\frac{-RL}{10}} - 1}} \left(\frac{P(s)}{F(s)}\right)|_{s=j} \tag{2.7}$$

Employing a gradient-based optimization algorithm involves the gradients of S_{11} and S_{21} which are related to coupling matrix elements by [19]

$$\frac{\partial S_{11}}{\partial M_{pq}} = -j4R_1 P_{pq} \left[A^{-1}\right]_{1p} \left[A^{-1}\right]_{q1} \tag{2.8}$$

$$\frac{\partial S_{21}}{\partial M_{pq}} = j2\sqrt{R_1 R_2} P_{pq} \left(\left[A^{-1}\right]_{Np} \left[A^{-1}\right]_{q1} + \left[A^{-1}\right]_{Nq} \left[A^{-1}\right]_{p1} \right). \tag{2.9}$$

The topology matrix, $[P]$, is defined by $P_{ij} = 1$ if $M_{ij} \neq 0$ and $P_{ij} = 0$ if $M_{ij} = 0$. When $p = q$, (2.8) and (2.9) are modified as

$$\frac{\partial S_{11}}{\partial M_{pp}} = -j2R_1 P_{pp} \left[A^{-1}\right]_{p1} \left[A^{-1}\right]_{p1} \tag{2.10}$$

$$\frac{\partial S_{21}}{\partial M_{pp}} = j2\sqrt{R_1 R_2} P_{pp} \left[A^{-1}\right]_{Np} \left[A^{-1}\right]_{p1} \tag{2.11}$$

Let us assume that $R_2 = rR_1$ and R_1 is an independent variable. Then, the gradient of S_{11} and S_{21} with respect to R_1 are calculated from equations

$$\frac{\partial S_{11}}{\partial R_1} = j2 \left[A^{-1}\right]_{11} + 2R_1 \left(\left[A^{-1}\right]_{11} \left[A^{-1}\right]_{11} + r \left[A^{-1}\right]_{N1} \left[A^{-1}\right]_{N1} \right) \tag{2.12}$$

$$\frac{\partial S_{21}}{\partial R_1} = -j2\sqrt{r} \left[A^{-1}\right]_{N1} + 2R_1\sqrt{r} \left(\left[A^{-1}\right]_{N1} \left[A^{-1}\right]_{11} + r \left[A^{-1}\right]_{NN} \left[A^{-1}\right]_{N1} \right) \tag{2.13}$$

Having both cost function and its gradient in terms of coupling elements, we are able to optimize any coupling matrix using any gradient-based optimization algorithm such as Newton, Gauss-Newton, and Steepest-descent methods [18].

2.2.2 Transversal Coupling Matrix Extraction

For the N-resonator transversal array shown in Fig. 2.2a, the $(N+2) \times (N+2)$ transversal coupling matrix, depicted in Fig. 2.3, may be analytically extracted. The idea is forcing the admittance matrix obtained from the scattering parameters to match that one calculated for the coupled resonators shown in Fig. 2.2a. The short-circuit parameters y_{21} and y_{22} are constructed directly from the transfer and reflection polynomials for $S_{11}(s)$ and $S_{21}(s)$ [20]. For a double-terminated network with source and load terminations of 1 Ω

$$\begin{aligned} y_{22}(s) &= \frac{n_1(s)}{m_1(s)} \\ y_{21}(s) &= \frac{p(s)}{\epsilon\, m_1(s)} \qquad\qquad N = even. \end{aligned} \tag{2.14}$$

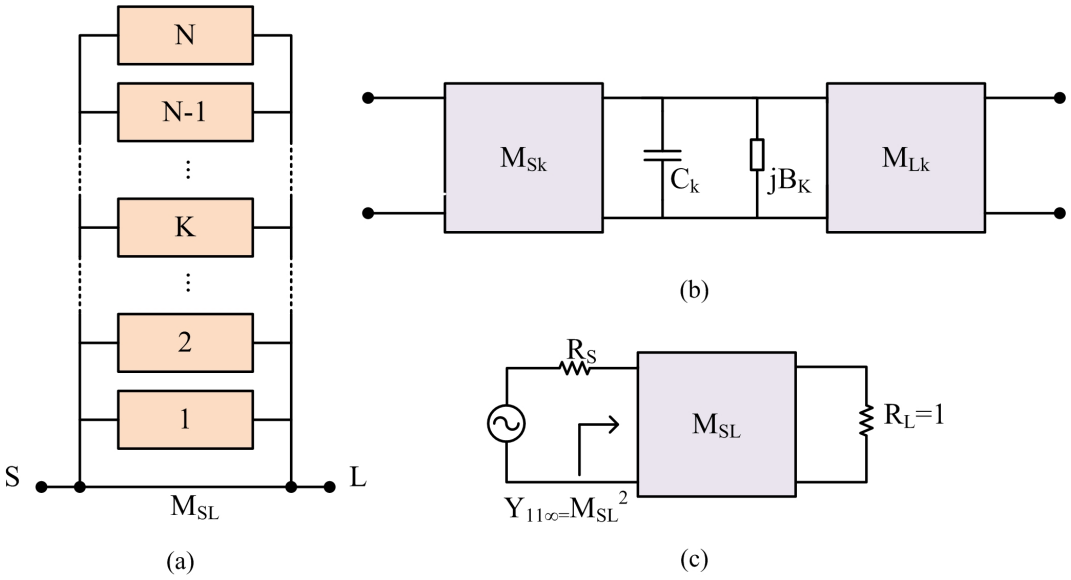

Figure 2.2: a) Transversal array of N coupled resonators; b) K_{th} transversal section, c) equivalent of transversal array at $s = \pm\infty$.

$$\begin{aligned} y_{22}(s) &= \frac{m_1(s)}{n_1(s)} \\ y_{21}(s) &= \frac{p(s)}{\epsilon\, n_1(s)} \qquad\qquad N = odd \end{aligned} \tag{2.15}$$

where

$$m_1 = Re(e_0 + f_0) + jIm(e_1 + f_1)s + Re(e_2 + f_2)s^2 + ... \tag{2.16}$$

$$n_1 = jIm(e_0 + f_0) + Re(e_1 + f_1)s + jIm(e_2 + f_2)s^2 + ... \tag{2.17}$$

and $e_i, i = 0, 1, ..., N$ and $f_i, i = 0, 1, ..., N$ are coefficients of $E(s)$ and $F(s)$, respectively.

Applying partial fractional expansion, the admittance parameters are expressed in terms of their residues r_{11k} and r_{21k}, and their purely real eigenvalues λ_k for $k = 1, 2, ...N$

$$[Y_N] = \begin{bmatrix} y_{11}(s) & y_{12}(s) \\ y_{21}(s) & y_{22}(s) \end{bmatrix} = j \begin{bmatrix} 0 & K_0 \\ K_0 & 0 \end{bmatrix} + \sum_{k=1}^{N} \frac{1}{(s - j\lambda_k)} \begin{bmatrix} r_{11} & r_{12} \\ r_{21} & r_{22} \end{bmatrix} \tag{2.18}$$

where $K_0 = 0$, except for the fully canonical case when the number of TZs equals the order of the filter, $N_z = N$.

The short-circuit admittance parameters can be also derived from the transversal

	S	1	2	3	..	k	..	N-1	N	L
S		M_{S1}	M_{S2}	M_{S3}	..	$M_{S,k}$	..	$M_{S,N-1}$	M_{SN}	M_{SL}
1	M_{1S}	M_{11}								M_{1L}
2	M_{2S}		M_{22}							M_{2L}
3	M_{3S}			M_{33}						M_{3L}
:	:				. .					:
k	M_{kS}					M_{kk}				M_{kL}
:	:						. .			:
N-1	$M_{N-1,S}$							$M_{N-1,N-1}$		$M_{N-1,L}$
N	M_{NS}								$M_{N,N}$	M_{NL}
L	M_{LS}	M_{L1}	M_{L2}	M_{L3}	..	M_{Lk}	..	$M_{L,N-1}$	M_{LN}	

Figure 2.3: N+2 fully canonical coupling matrix for the transversal array shown in Fig. 2.2a (unspecified elements are zeros).

coupling network. For each transversal element, presented in Fig. 2.2b, an $ABCD$ transition matrix is obtained as

$$[ABCD]_k = -\begin{bmatrix} \frac{M_{LK}}{M_{SK}} & \frac{(sC_k+jB_k)}{M_{SK}M_{LK}} \\ 0 & \frac{M_{SK}}{M_{LK}} \end{bmatrix} \tag{2.19}$$

that can be directly converted to equivalent short-circuit y-parameters

$$\begin{aligned} [y]_k = \begin{bmatrix} y_{11k}(s) & y_{12k}(s) \\ y_{21k}(s) & y_{22k}(s) \end{bmatrix} &= \frac{M_{sk}M_{Lk}}{(sC_k+jB_k)} \begin{bmatrix} \frac{M_{sk}}{M_{Lk}} & 1 \\ 1 & \frac{M_{Lk}}{M_{sk}} \end{bmatrix} \\ &= \frac{1}{(sC_k+jB_k)} \begin{bmatrix} M_{sk}^2 & M_{sk}M_{Lk} \\ M_{sk}M_{Lk} & M_{Lk}^2 \end{bmatrix} \end{aligned} \tag{2.20}$$

The two-port admittance matrix for the transversal coupling circuit is the sum of the y-parameter matrices for N individual transversal sections plus the admittance

matrix for the source-load coupling inverter M_{sL}

$$\begin{aligned}[Y_N] &= [y_{SL}] + \sum_{k=1}^{N} \begin{bmatrix} y_{11k}(s) & y_{12k}(s) \\ y_{21k}(s) & y_{22k}(s) \end{bmatrix} \\ &= j \begin{bmatrix} 0 & M_{SL} \\ M_{SL} & 0 \end{bmatrix} + \sum_{k=1}^{N} \frac{1}{sC_k + jB_k} \begin{bmatrix} M_{Sk}^2 & M_{SK}M_{LK} \\ M_{SK}M_{LK} & M_{Lk}^2 \end{bmatrix} \end{aligned} \tag{2.21}$$

Equating (2.18) and (2.21) yields

$$\begin{aligned} M_{Lk} &= \sqrt{r_{22k}} = T_{Nk} \\ M_{Sk} &= \frac{r_{21k}}{\sqrt{r_{22k}}} = T_{1k} \qquad\qquad k = 1, 2, ..., N. \end{aligned} \tag{2.22}$$

T_{Nk} and T_{1k} are called the eigenvectors of the admittance parameters. The source-load coupling, M_{SL}, is calculated form Fig. 2.2c when $s \to \infty$

$$\begin{aligned} |M_{SL}| &= \sqrt{\frac{1 - |s_{11\infty}|}{1 + |s_{11\infty}|}} \\ |M'_{SL}| &= \sqrt{\frac{1 + |s_{11\infty}|}{1 - |s_{11\infty}|}} \\ &= \left| \frac{1}{M_{SL}} \right| \end{aligned} \tag{2.23}$$

As shown in (2.23), always two analytic values for M_{SL} are calculated. While for bandstop filters both values are practical, for bandpass filters, always one of the two source-load coupling values is too large to be practically implemented.

The synthesized transversal matrix can be converted to desired coupled-resonator topologies using matrix transformations [21]. The limitation of the matrix transformations technique is that it is not applicable to all arbitrary topologies. The more general method is employing optimization techniques. The most important part of using optimization methods is defining appropriate cost functions as well as good initial values for starting the optimization process. One of the most effective cost functions, to extract the folded coupling matrix from the transversal one, is defined as [22]

$$C = \sum_{i=1}^{N} (\lambda_i^{P_1'} - \lambda_i^{P_1}) + \sum_{i=1}^{N-1} (\lambda_i^{P_2'} - \lambda_i^{P_2}) + \sum_{i=1}^{N-1} (\lambda_i^{P_3'} - \lambda_i^{P_3}) \tag{2.24}$$

where $\lambda_i^{P_1}$, $\lambda_i^{P_2}$, and $\lambda_i^{P_3}$ are ith eigenvalues of the transversal coupling matrix, its upper submatrix, and its lower submatrix, respectively. Similarly, $\lambda_i^{P_1'}$, $\lambda_i^{P_2'}$, $\lambda_i^{P_3'}$ are the ith eigenvalues of the folded coupling matrix, its upper submatrix, and its lower submatrix, respectively. Any matrix whose eigenvalues are different from its lower and upper submatices' eigenvalues and presents the desired topology, can be used as the optimization's starting point.

Optimization problems may be solved by employing $Matlab$ optimizer functions such as $lsqnonlin$ and $fsolve$ functions.

2.3 Bandstop Coupling Matrix Extraction from Bandpass Filtering Function

It is shown in [23] that the transversal coupling scheme shown in Fig. 2.2a can be used for modeling coupled-resonator bandstop filters as well. The main advantage of this result is that Chebyshev or pseudo-elliptic bandstop filters can be designed using bandpass coupled resonators without requiring to load a uniform transmission line with bandstop elements, spaced by odd multiples of quarter-wavelength transmission line sections.

The first step to synthesize bandstop coupling matrices, using the procedure outlined in Section 2.2, is obtaining bandstop filtering functions. A bandpass filtering function can change to a bandstop one by appropriately exchanging reflection, S_{11}, and transmission, S_{21}, functions. In bandstop filtering functions, the number of TZs equals the number of resonators which results in non-zero source-load coupling values.

As indicated in [23] and shown in (2.23), always two different source-load coupling values are obtained during the coupling matrix synthesis, for both bandpass and bandstop filters. A very interesting result for the bandstop case is that both values of M_{SL} are practical in contrast to the bandpass case where only the smaller coupling value is practical, except for second-order pandpass filters with TZs located close to the passband.

2.4 Multi-band Bandstop Coupling Matrix synthesis

The procedure to synthesize multi-band coupling matrices is the same as that for a single-band one. The only difference is synthesizing a multi-band filtering function instead of single-band one.

Multi-band bandstop transfer functions can be synthesized directly from the single-band lowpass prototype (LPP) by employing appropriate frequency transformations. In [24], a dual-band bandstop transfer function is obtained by applying a symmetric frequency mapping on a single-band LPP filtering function. Another symmetric frequency transformation is reported in [25] to construct a quad-band bandstop transfer function from the LPP.

In addition, multi-band bandstop filtering functions can be obtained by exchanging S_{11} and S_{21} of multi-band bandpass filters. Some researches are conducted on synthesizing multi-band bandpass filtering functions such as those presented in [26–29]. The recursive analytic method presented in [26] results in synthesizing symmetric or asymmetric multi-band bandpass filters, with equi-ripple passbands and stopbands and arbitrary placed TZs, by appropriately determining the locations of the TZs and RZs of filters. Two iterative techniques are also presented in [27] to design dual-band all-pole bandpass filters by adjusting the extrema and zeros of filtering functions. In [28], an analytic formula is introduced to synthesize multi-band bandpass filters by appropriately connecting several single band filters. In addition, a frequency transformation, for synthesizing either symmetric or asymmetric triple-band bandpass filters, is introduced in [29] which generates multiple passbands with the same number of poles and return loss levels in passbands.

In this research, the technique presented in [27], to synthesize dual-band all-pole bandpass filter, has been appropriately developed to design general multi-band bandpass filters, with arbitrary placed TZs out of passbands. Subsequently, the multi-band bandpass filtering function will be converted to that of the multi-band bandstop filter.

2.5 Illustrative Example: Triple-band Bandstop Coupling Matrix

To summarize the multi-band bandstop coupling matrix synthesis procedure and to present an implementation example, a coupling matrix is synthesized for a triple-band bandstop filter with $N = 8$ and the coupling topology shown in 2.5b. The filter specifications are outlined in Table 2.1.

The coefficients of S_{11}'s and S_{21}'s numerator and denominator polynomials shown in Table 2.2 generate the triple-band bandpass filter responses presented in Fig.2.4a.

The coefficients of S_{11}'s and S_{21}'s numerator and denominator polynomials of the triple-band bandstop filter are shown in Table 2.3 as well, representing the frequency responses shown in Fig. 2.5a. In addition, Table 2.4 contains the residues, eigenvalues and eigenvectors calculated from the polynomials' coefficients presented in Table 2.3. Finally, the transversal coupling matrix, exactly generating the scattering parameters shown in Fig. 2.5a, is presented in (2.25). The synthesized transversal coupling matrix in (2.25) can be transformed to the desired folded filter topology, as shown in (2.26), by employing (2.24) and appropriate optimization algorithms.

Table 2.1: Specifications of a triple-band bandstop filter

Filter's Specifications	band1	band2	band3
Number of TZs	3	2	3
Location of RZs	-1.40 -1.20 -0.50	-0.40 0.40	1.40 1.20 0.50
Equi-Ripple Frequency Band	(-1.00,-0.63)	(-0.10,0.10)	(0.63,1.00)
Minimum of Attenuation	18 dB	18 dB	18 dB

Table 2.2: Triple-band bandpass filter: coefficients of $E(s)$, $F(s)$ and $P(s)$ polynomials

S^i i	Coefficients of S_{11} and S_{21} Denominator polynomials $E(s)$ (e_i)	Coefficients of S_{11} Numerator Polynomial $F(s)$ (f_i)	Coefficients of S_{21} Numerator Polynomials $P(s)$ (p_i)
0	0.0244	0.0014	0.0242
1	0.1065	0	0
2	0.5262	0.2705	0.2779
3	0.8568	0	0
4	2.1463	1.3099	0.9147
5	1.8341	0	0
6	2.6833	2.0118	0.8188
7	1.0414	0	0
8	1.0000	0.9766	0.2149

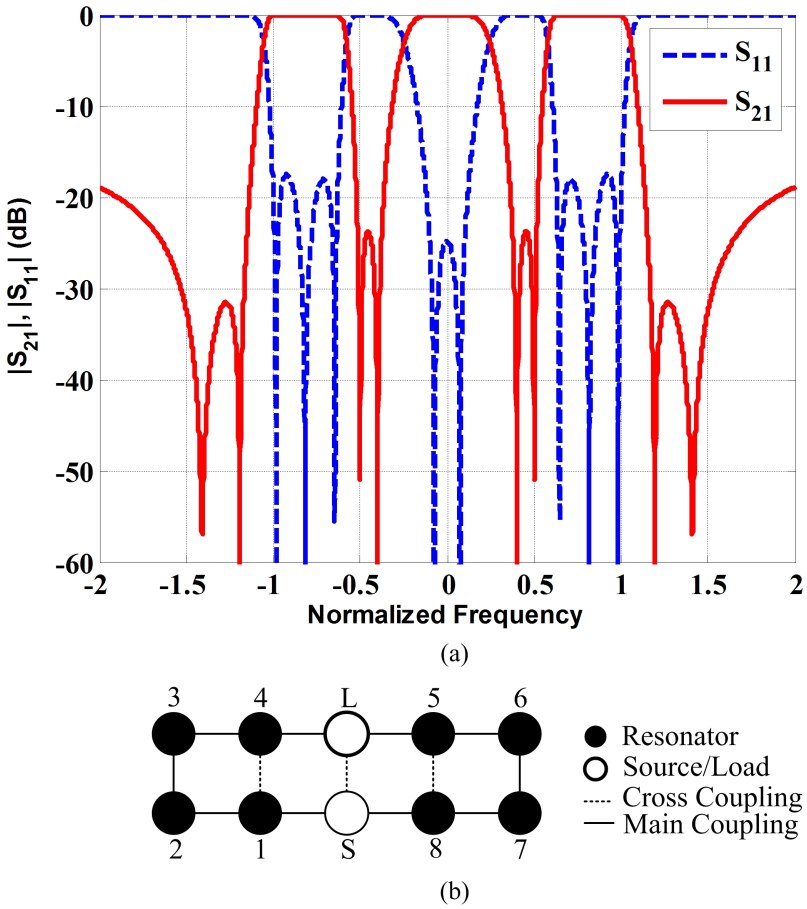

Figure 2.4: Triple-band lowpass bandpass filter; a) normalized frequency responses, b) coupling topology of the filter.

Table 2.3: Triple-band bandstop filter: coefficients of $E(s)$, $F(s)$ and $P(s)$ polynomials

S^i i	Coefficients of S_{11} and S_{21} Denominator polynomials $E(s)$ (e_i)	Coefficients of S_{11} Numerator Polynomial $F(s)$ (f_i)	Coefficients of S_{21} Numerator Polynomials $P(s)$ (p_i)
0	0.0244	0.0242	+j 0.0014
1	0.1065	0	0
2	0.5262	0.2779	+j 0.2705
3	0.8568	0	0
4	2.1463	0.9147	+j 1.3099
5	1.8341	0	0
6	2.6833	0.8188	+j 2.0118
7	1.0414	0	0
8	1.0000	0.2149	+j 0.9766

Table 2.4: Triple-band bandstop filter: residues, eigenvalues and eigenvectors

k	Eigenvalues λ_k	Residues r_{21k}	Residues r_{22k}	Eigenvectors $T_{Nk} = \sqrt{r_{22k}}$	Eigenvectors $T_{1k} = \frac{r_{21k}}{\sqrt{r_{22k}}}$
1	1.1974	-0.3012	0.3014	0.5490	-0.5487
2	-1.1974	0.3012	0.3014	0.5490	0.5487
3	1.0270	0.0313	0.0319	0.1785	0.1753
4	-1.0270	-0.0313	0.0319	0.1785	-0.1753
5	0.5552	0.0303	0.0305	0.1746	0.1737
6	-0.5552	-0.0303	0.0305	0.1746	-0.1737
7	0.2931	-0.0648	0.0649	0.2547	-0.2544
8	-0.2931	0.0648	0.0649	0.2547	0.2544

$$M = \begin{pmatrix} 0 & -0.5487 & 0.5487 & 0.1753 & -0.1753 & 0.1737 & -0.1737 & -0.2544 & 0.2544 & 0.8039 \\ -0.5487 & -1.1974 & 0 & 0 & 0 & 0 & 0 & 0 & 0 & 0.5490 \\ 0.5487 & 0 & 1.1974 & 0 & 0 & 0 & 0 & 0 & 0 & 0.5490 \\ 0.1753 & 0 & 0 & -1.0270 & 0 & 0 & 0 & 0 & 0 & 0.1785 \\ -0.1753 & 0 & 0 & 0 & 1.0270 & 0 & 0 & 0 & 0 & 0.1785 \\ 0.1737 & 0 & 0 & 0 & 0 & -0.5552 & 0 & 0 & 0 & 0.1746 \\ -0.1737 & 0 & 0 & 0 & 0 & 0 & 0.5552 & 0 & 0 & 0.1746 \\ -0.2544 & 0 & 0 & 0 & 0 & 0 & 0 & -0.2931 & 0 & 0.2547 \\ 0.2544 & 0 & 0 & 0 & 0 & 0 & 0 & 0 & 0.2931 & 0.2547 \\ 0.8039 & 0.5490 & 0.5490 & 0.1785 & 0.1785 & 0.1746 & 0.1746 & 0.2547 & 0.2547 & 0 \end{pmatrix} \tag{2.25}$$

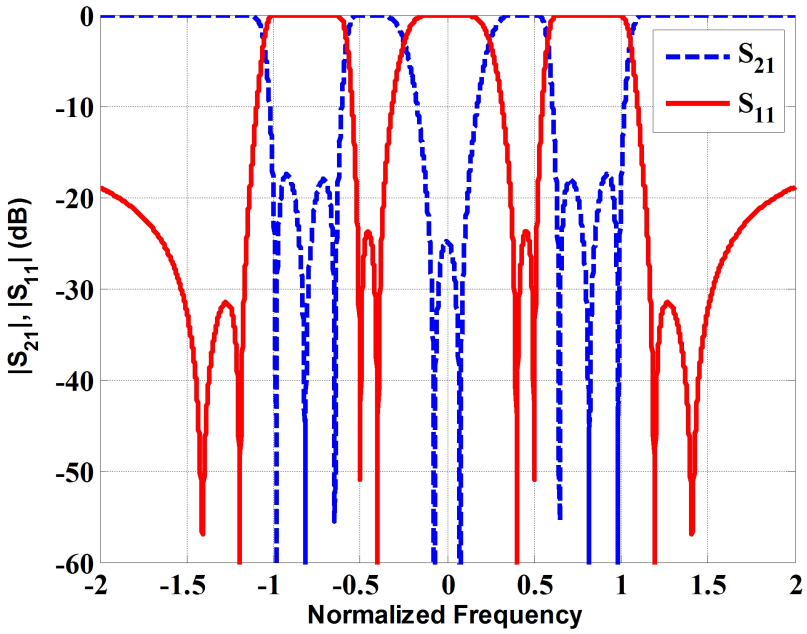

(a)

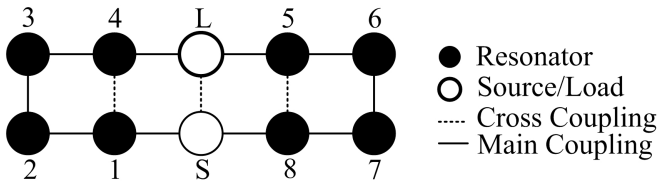

(b)

Figure 2.5: Triple-band lowpass bandstop filter; a) normalized frequency responses, b) coupling topology of the filter.

$$M = \begin{pmatrix} 0 & 0.0546 & 0 & 0 & 0 & 0 & 0 & 0 & 0.1017 & 0.1005 \\ 0.0546 & 0 & 0.0770 & 0 & -0.0171 & 0 & 0 & 0 & 0 & 0 \\ 0 & 0.0770 & 0 & -0.0746 & 0 & 0 & 0 & 0 & 0 & 0 \\ 0 & 0 & -0.0746 & 0 & 0.0777 & 0 & 0 & 0 & 0 & 0 \\ 0 & -0.0171 & 0 & 0.0777 & 0 & 0 & 0 & 0 & 0 & 0.0550 \\ 0 & 0 & 0 & 0 & 0 & 0 & 0.0631 & 0 & 0.1296 & 0.1018 \\ 0 & 0 & 0 & 0 & 0 & 0.0631 & 0 & -0.0494 & 0 & 0 \\ 0 & 0 & 0 & 0 & 0 & 0 & -0.0494 & 0 & 0.0632 & 0 \\ 0.1017 & 0 & 0 & 0 & 0 & 0.1296 & 0 & 0.0632 & 0 & 0 \\ 0.1005 & 0 & 0 & 0 & 0.0550 & 0.1018 & 0 & 0 & 0 & 0 \end{pmatrix} \tag{2.26}$$

In the following chapter, filters with up to $N = 12$ are presented and their pole locations organized in single-, double- or triple-band bandstop filters.

Chapter 3

Advanced Multi-Band Bandstop Filters

The coupling matrix concept, investigated in Chapter 2, can be used to design advanced multi-band bandstop filters. To realize coupling matrices as microwave filters, designers need to choose appropriate types of resonators and technologies.

In comparison with multi-stopband microstrip filters [30–32], multi-stopband substrate integrated waveguide (SIW) filters have higher quality factor, lower insertion loss and offer a shielded environment which make them more attractive towards higher frequencies. In addition, they can be integrated with other planar circuitries.

A few multi-passband filters are reported in SIW technology. A triple- and two dual-passband SIW filters with Chebyshev and quasi-elliptic responses are designed and prototyped in [33] based on cross-coupled resonators.

Multi-stopband filters, as opposed to multi-passband ones, have been theoretically investigated based on coupling matrix designs such as those presented in [24, 25].

Despite all multi-stopband coupling matrix investigations, multi-stopband filters in SIW or waveguide technology have not been reported, neither in direct-coupled nor cross-coupled topology. Therefore, in this chapter, we design, simulate, prototype and measure two multi-band quasi-elliptic SIW bandstop filters. The first filter is designed by employing cross-coupled rectangular resonators, presenting three stopbands separated by two passbands. Nonresonating modes and in-line cascaded singlets are used to design the second SIW bandstop filter which has two stopbands separated by one passband.

3.1 Triple-Stopband Dual-Passband Cross-Coupled Resonator Filter

Cross couplings between resonators are widely used to generate multiple paths between sources and loads which can result in creating transmission zeros (TZs) in passband filters at some frequencies. The number of generated TZs equals the number of resonators bypassed by the paths between loads and sources and created by the cross couplings. The multi-path idea can be also used to generate reflection zeros in bandstop filters. Coupling matrices appropriately present the multi-path concepts in microwave filters.

The signs of coupling values are associated with the nature of couplings between resonators. In general, the coupling coefficient of any two coupled resonators, as in Fig. 3.1, is defined as

$$k = \frac{\int\int\int \epsilon \vec{E}_1 . \vec{E}_2 dv}{\sqrt{\int\int\int \left|\vec{E}_1^2\right| dv \,.\, \int\int\int \left|\vec{E}_2^2\right| dv}} + \frac{\int\int\int \mu \vec{H}_1 . \vec{H}_2 dv}{\sqrt{\int\int\int \left|\vec{H}_1^2\right| dv \,.\, \int\int\int \left|\vec{H}_2^2\right| dv}} \tag{3.1}$$

where $\vec{E}$ and $\vec{H}$ are electric and magnetic field vectors at resonant frequencies, and the subscripts 1 and 2 refer to first and second resonator, respectively. The volume integrals are over the regions with permiability of μ and permittivity of ϵ. The first term and second term in (3.1) are called electric and magnetic couplings, respectively. It should be noted that k can be either positive or negative, as implied by (3.1).

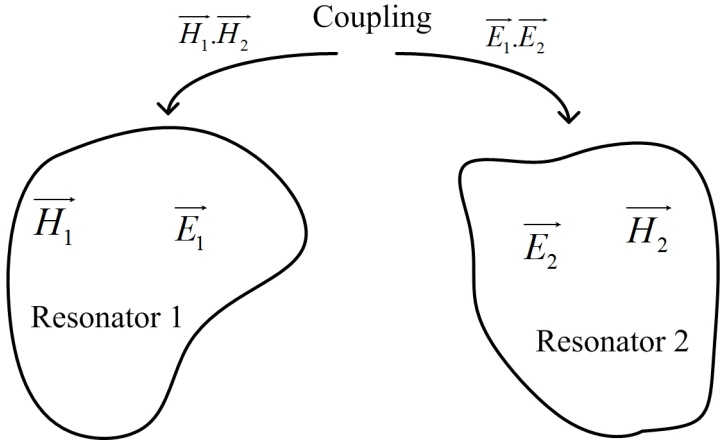

Figure 3.1: General coupling mechanism between two resonators with arbitrary shapes.

When calculating coupling coefficients using (3.1), one requires the knowledge of the electromagnetic field distributions at resonant frequencies and calculation of complicated volume integral that is not an easy task. Full electromagnetic simulators can be used to find some characteristic frequencies related to coupling coefficients. As indicated in [17], the transmission function of any two coupled resonators has two resonant frequencies, f_m and f_e, which are the resonant frequencies of the coupled structure when the symmetry plane between two coupled resonators is replaced by a magnetic and electric wall, respectively. The coupling coefficient can be calculated as

$$k = \frac{f_m^2 - f_e^2}{f_m^2 + f_e^2} \tag{3.2}$$

which is a circuit approximation to (3.1) and is widely used in practical filter design.

Negative and positive couplings are usually called *electric* and *magnetic* couplings, respectively. Electric and magnetic couplings, in coupled waveguide resonators, are implemented by capacitive and inductive apertures between coupled resonators, respectively. Inductive apertures in SIW resonators can be built by all-through via holes. SIW capacitive apertures have to be implemented by partial-hight via holes which result in manufacturing sensitivity, especially in thin substrates and at high frequencies. Therefore, new electric coupling structures in SIW technology have been presented to overcome difficulties of creating capacitive apertures in H-plane SIW filters. Some of these structures are reported in [34–39]. All these structures involve etching slots on the SIW's top copper and between two coupled resonators which make design and manufacturing processes more difficult. These are no longer *pure* SIW circuits since parts of the electromagnetic field extend above the SIW in the slotted regions. Therefore, such components are no longer completely shielded.

To demonstrate the difference between electric and magnetic couplings, two coupled rectangular SIW resonators with positive and negative couplings are shown in Fig. 3.2a and Fig. 3.2b , respectively, with their transmission functions. The negative coupling in Fig. 3.2b has been reported, for the first time, in [39]. The two coupled resonators are designed to resonate at 10 GHz. RT/ Duroid 6002 with permittivity of 2.94 and loss tangent of 0.0012 is chosen as substrate.

As illustrated in Fig. 3.3, the magnetic fields, in two magnetically coupled resonators, are in phase at the upper resonant frequency, f_m, and out of phase at the lower resonant frequency, f_e. On the contrary, the magnetic fields are out of phase at f_m, and in phase at f_e in two electrically coupled resonators, as shown in Fig. 3.4.

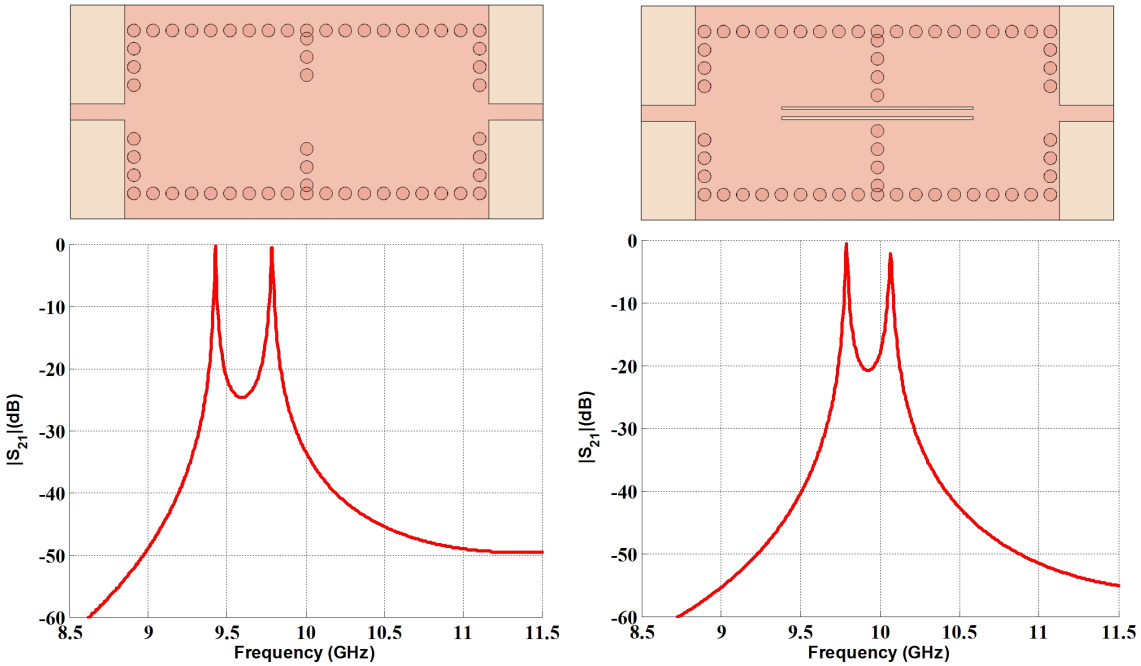

Figure 3.2: Coupling structure and transmission function of a) two magnetically coupled resonators, b) two electrically coupled resonators.

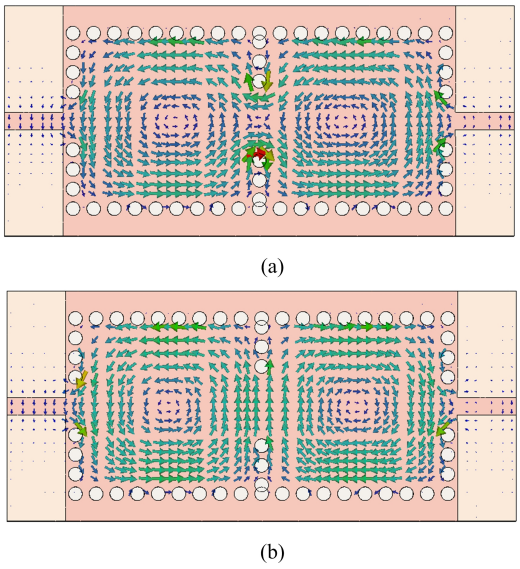

Figure 3.3: Magnetic field distributions in two magnetically coupled resonators; a) lower mode, b) upper mode.

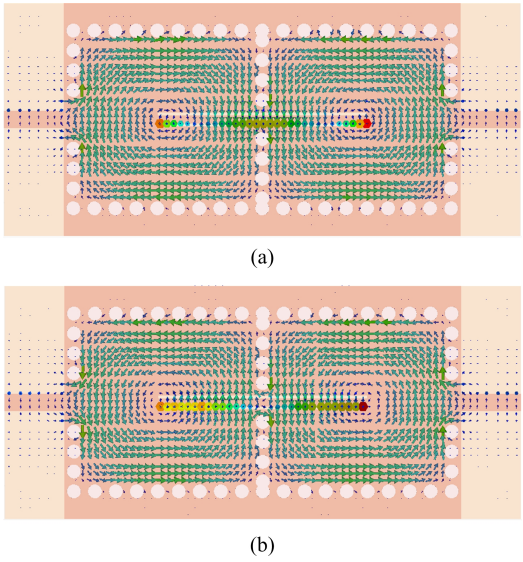

Figure 3.4: Magnetic field distributions in two electrically coupled resonators; a) lower mode, b) upper mode.

3.1.1 Filter Design

The designed triple-band bandstop filter consists of six cross-coupled resonators as shown in Fig. 3.5. The proposed bandstop filter has six transmission zeros (TZs) located in the stopbands, and six reflection zeros (RZs) located on both sides of the stopbands which result in sharp roll-offs. The center frequency, f_0, and overall bandwidth, BW, of the filter are chosen to be 19.5 GHz and 4.5 GHz, respectively. A coupling matrix representing the filter response is synthesized using the procedures outlined in Chapter 2, and shown in (3.3). Note that all resonators are synchronously tuned and all the coupling coefficients are positive.

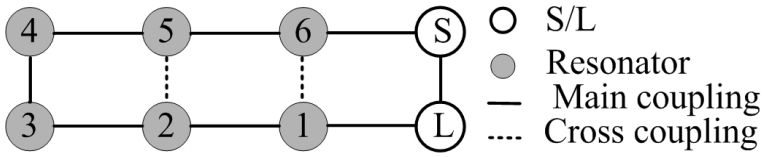

Figure 3.5: Coupling topology of the triple-band bandstop SIW filter.

$$\begin{pmatrix} 0 & 0.6140 & 0 & 0 & 0 & 0 & 0 & 0.6114 \\ 0.6140 & 0 & 0.6970 & 0 & 0 & 0 & 0.3717 & 0 \\ 0 & 0.6970 & 0 & 0.4866 & 0 & 0.1637 & 0 & 0 \\ 0 & 0 & 0.4866 & 0 & 0.1469 & 0 & 0 & 0 \\ 0 & 0 & 0 & 0.1469 & 0 & 0.4866 & 0 & 0 \\ 0 & 0 & 0.1637 & 0 & 0.4866 & 0 & 0.6970 & 0 \\ 0 & 0.3717 & 0 & 0 & 0 & 0.6970 & 0 & 0.6140 \\ 0.6114 & 0 & 0 & 0 & 0 & 0 & 0.6140 & 0 \end{pmatrix} \tag{3.3}$$

The symmetry of the filter's topology in Fig. 3.5 implies a symmetric coupling matrix with $M_{S1} = M_{6L}$, $M_{12} = M_{56}$ and $M_{23} = M_{45}$, as shown in (3.3). Note that similar to a single-band bandstop filter, the source-load coupling is required. However, since the number of RZs is equal to the number of resonators, the source-load coupling value is different from unity [23]. First, the initial size of the resonators are calculated based on their resonant frequencies [33]

$$f_0 = \frac{c}{2\sqrt{\epsilon_r}}\sqrt{\frac{1}{a^2} + \frac{1}{l^2}} \tag{3.4}$$

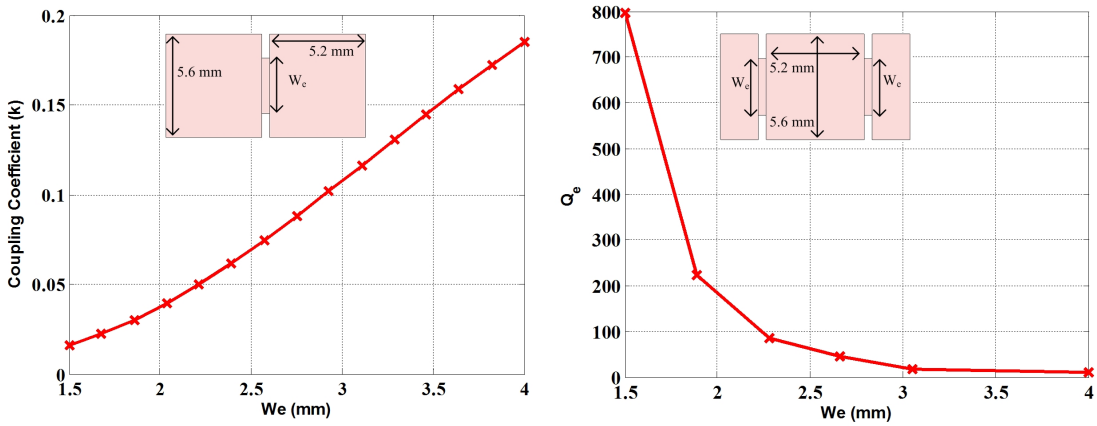

(a) (b)

Figure 3.6: a) Positive coupling coefficient of the coupled resonators, b) external quality factor of the input/output resonator.

where a and l are the waveguide resonator's width and length, respectively. c is the wave velocity in free space, and ϵ_r is the dielectric constant. The eigenvalue solver of CST is used to simulate a pair of coupled TE_{101} resonators and obtain two split resonant frequencies, f_1 and f_2. The coupling coefficient, k_{ij}, versus aperture width is presented in Fig. 3.6a. Then the normalized coupling coefficients in (3.3) are calculated by

$$m_{ij} = k_{ij}\frac{f_0}{BW} \tag{3.5}$$

Using the curve shown in Fig. 3.6a, the size of each aperture located between two coupled resonators is appropriately chosen to obtain its corresponding coupling coefficient.

The external quality factor of a single double-loaded resonator is obtained by

$$Q_e = \frac{f_0}{\Delta f_{3dB}} \tag{3.6}$$

where f_0 is the frequency at which the resonator transmission coefficient is maximum, and Δf_{3dB} is the 3 dB bandwidth corresponding to f_0. On the other hand, the external quality factor is related to the source-resonator coupling, M_{SR}, by

$$Q_e = \frac{F_0}{BW}\frac{1}{M_{SR}^2} \tag{3.7}$$

Here F_0 and BW are the center frequency and bandwidth of the filter, respectively.

Then the filter is designed in H-plane waveguide technology using the commercial software package μWave Wizard. Note that μWave Wizard is one of the fastest electromagnetic simulators, based on mode matching technique, that can be used to analyze certain conventional waveguide and substrate integrated waveguide components, but it is not applicable to design all microwave devices. The source waveguide's width, a_e, is determined by the cutoff frequency of the filter, f_c, which is chosen appropriately based on the center frequency and bandwidth of the filter [33]

$$a_e = \frac{c}{2f_c\sqrt{\epsilon_r}} \tag{3.8}$$

Following this step, the designed filter in waveguide technology is properly translated to SIW using [40]

$$a_{SIW} = a_{wave} + p(0.766e^{\frac{0.448d}{p}} - 1.176e^{\frac{-1.214}{p}}) \tag{3.9}$$

where a_{SIW} and a_{wave} are the physical dimensions in SIW and waveguide technology, respectively. d is the via hole diameter in the SIW filter, and p is the center-to-center spacing between two adjacent vias.

Fig. 3.7a shows the final SIW filter with waveguide ports. The cut-off frequency of the waveguide port is 15.8 GHz, and RT/Duroid 6002 with dielectric constant of 2.94, loss tangent of 0.0012, and thickness of 0.508 mm is chosen as substrate. The diameters of all via holes are 0.5 mm, and the minimum center-to-center pitch between any two adjacent vias is greater than 0.7 mm and less than 1 mm to prevent manufacturing difficulties as well as power leakage. The simulated response of the filter is shown in Fig. 3.7b and compared with that calculated from the coupling matrix shown in (3.3).

Generally, the coupling matrix elements are frequency-dependent [41–43]. Although a coupling matrix with frequency-independent elements is acceptable for narrowband applications, the frequency-independent coupling matrix synthesized in this paper presents a triple-stopband filter with almost equi-ripple stopbands and passbands that provides a good starting point for the filter design. The full-wave frequency simulator of CST takes into account all frequency components to calculate the frequency responses of the filter. This is the reason for some simulated TZs and RZs, as well as levels of some return losses in the passbands and attenuations in the stopbands, not precisely matching those obtained from the coupling matrix. It should

be noted, however, that there is still acceptable agreement between the locations of the TZs and RZs obtained from CST and the coupling matrix for the designed filter, even though the overall fractional bandwidth is 23%.

The left-most and the right-most RZs in Fig. 3.7b are attributed to the distance between the source/load aperture and the rest of the filter as well as its size. Corresponding TZs in a passband design are observed in [44], and it is demonstrated that they can be added to the coupling matrix by introducing detuned resonators.

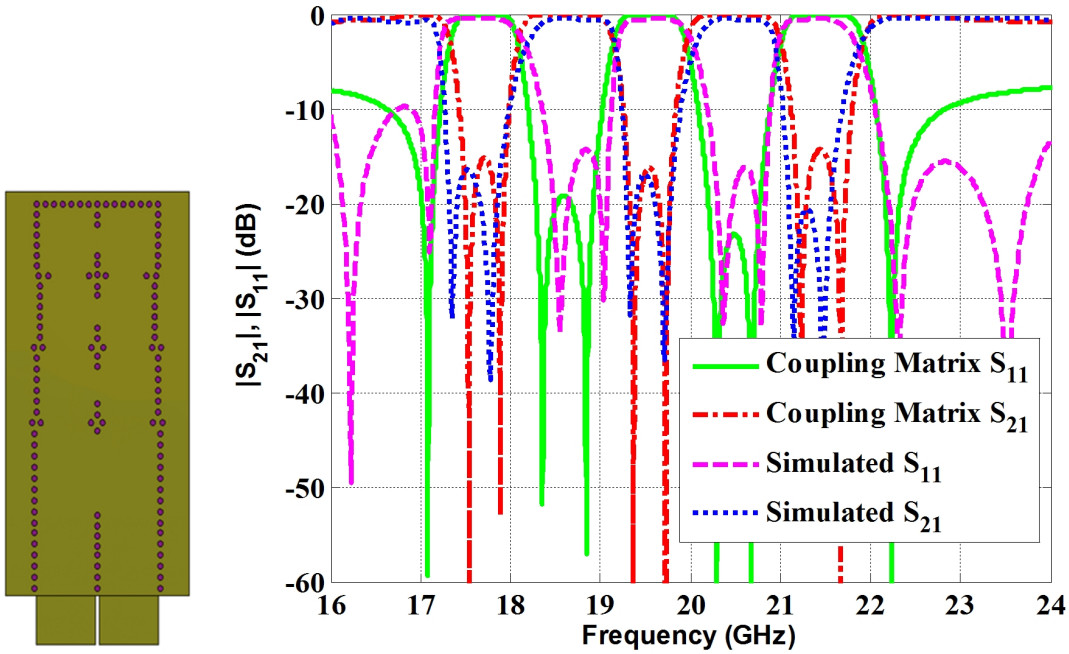

Figure 3.7: a) Triple-band bandstop filter with waveguide ports; b) scattering parameters of the filter; simulated versus coupling matrix.

3.1.2 Experimental Results

A top view of the prototyped filter, with bent microstrip ports and SIW-to-microstrip transitions, is depicted in Fig. 3.8a. A Thru-Reflect-Line (TRL) calibration kit is used to deembed the effects of the microstrip lines and their transitions to coaxial ports. Fig. 3.8b shows the comparison between simulated and measured results. Good agreement is observed. The locations of the simulated TZs and RZs in the stopbands and passbands are well reproduced in the measurements. The insertion loss in the two

passbands is measured better than 1.54 dB, and the return loss in both passbands is better than 17 dB. In addition, the attenuation in the first, second and third stopband are better than 12 dB, 15.5 dB and 12.5 dB, respectively. The measured responses show a very small upward frequency shift. We attribute this frequency shift to the via holes which, when fabricated using a drill size of 0.5 mm, turn out to be slightly larger than the nominal value. The larger diameters of the via holes decrease the resonators effective widths and lengths and cause a small increases in the resonant frequencies of the resonators. Moreover, this shift is within the permittivity tolerances of 2.94 $\pm$ 0.04.

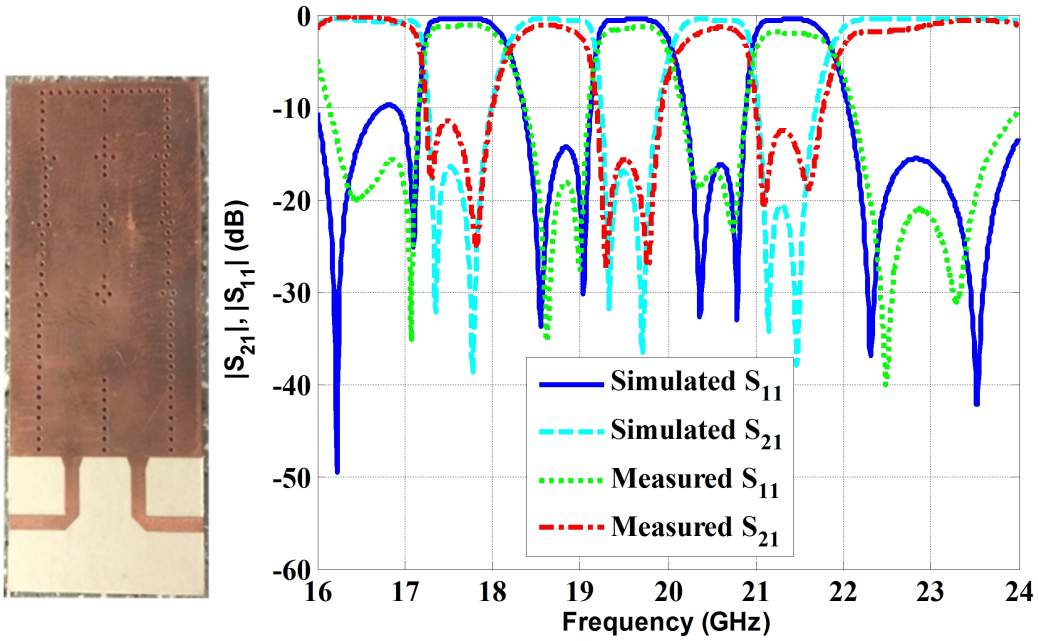

(a) (b)

Figure 3.8: a) Prototyped triple-band bandstop filter with bent microstrip ports; b) comparison between measured and simulated scattering parameters of the filter.

3.2 Dual-Stopband Triple-Passband Filter Using Cascaded Singlets and Nonresonating Modes

Small size is one of the most important features of microwave filters. Using dual-mode or multi-mode resonators is a very well-known method for filter size reduction [45–47]. In multi-mode filters, each resonator contributes to generate more than one

attenuation pole. Therefore, the number of physical resonators is smaller than the order of the filter, hence filter size reduction is achieved.

The multi-mode concept can be also extended to nonresonating nodes (NRNs). In general, a nonresonating node can be represented by any propagating or evanescent mode. Using the NRN concept in a filter considerably reduces the size of the filter. Beside compactness, NRNs create direct paths which bypass resonators and enable us to have N TZs with N resonators [48].

The coupling matrix extraction method, outlined in Chapter 2, is general and can be also used for filters involving NRNs with a small modification in (2.1). As shown in (2.1), the frequency-dependent part of matrix A, U, represents the resonating nodes in the circuits. Thus for a filter which has only resonating nodes, matrix U will be the identity matrix. When NRNs are involved, their corresponding values in the matrix U are set to zero. The remaining procedure of the coupling matrix synthesis for filters using NRNs is identical to that of the conventional coupling matrix.

The concept of using the interaction of two modes to create TZs was demonstrated in [49] for the design of conventional iris-coupled resonator filters which produce TZs in the upper stopband through the use of asymmetric irises between cavities. The NRN model in [50] explains the creation and location of TZs. As demonstrated in Fig. 3.9, the TE_{10} mode at the input waveguide excites not only the TE_{201} resonating mode. A part of the electromagnetic energy is also coupled to the TE_{10} propagating mode. This propagating mode creates a direct path between the output and input and therefore creates a TZ.

The size of the input and output apertures and their relative positions determine the location of the TZ [48]. The typical responses of the structures shown in Fig. 3.9a and Fig. 3.9b are presented in Fig. 3.10a and Fig. 3.10b, respectively. If both input and output waveguides are offset in the same direction, as in Fig. 3.9a, the magnetic fields of the TE_{10} mode are out of phase at the input and the output which implies a negative bypass coupling. The coupling matrix synthesized for the structure shown in Fig. 3.9a is presented in (3.10) confirming the negative source-load coupling to generate a TZ below the passband, as in Fig. 3.10a.

$$\begin{pmatrix} 0 & 0.3765 & -0.1696 \\ 0.3765 & 0.7097 & 0.3560 \\ -0.1696 & 0.3560 & 0 \end{pmatrix} \tag{3.10}$$

On the contrary, when the input and the output waveguides are offset in different

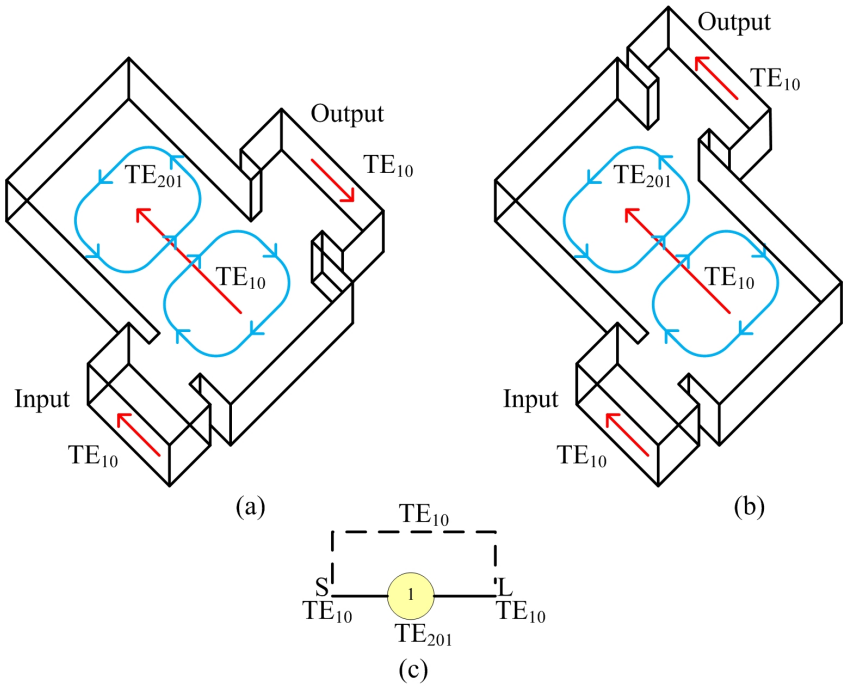

Figure 3.9: Single rectangular cavity employing both resonating and nonresonating modes; a) symmetric input and output apertures, b) asymmetric input and output apertures, c) corresponding circuit topology.

direction, as in Fig. 3.9b, the magnetic fields at the input and output are in phase. This mechanism generates a positive source-load coupling, as presented in (3.11), and shifts the transmission zero from below the passband to above the passband, as in Fig. 3.10b.

$$\begin{pmatrix} 0 & 0.3765 & 0.1696 \\ 0.3765 & -0.7097 & 0.3560 \\ 0.1696 & 0.3560 & 0 \end{pmatrix} \tag{3.11}$$

Some passband filters based on NRNs are reported in the literature. In [51], Amari and Rosenberg investigate the possibility of generating TZs by using NRNs, but without involving any coupling between resonators. Their method relies on the extracted-pole technique and multi-mode resonators which are connected by NRNs. Their approach can be used to design filters with the maximum number of TZs. An analytical method for synthesizing in-line pseudo-elliptic bandpass filters based on NRNs is reported in [52]. In this method, TZs are extracted at internal NRNs, and the location of each TZ is independently introduced and controlled by one resonator. The proposed method offers infinite number of solutions for a specific filter, and a

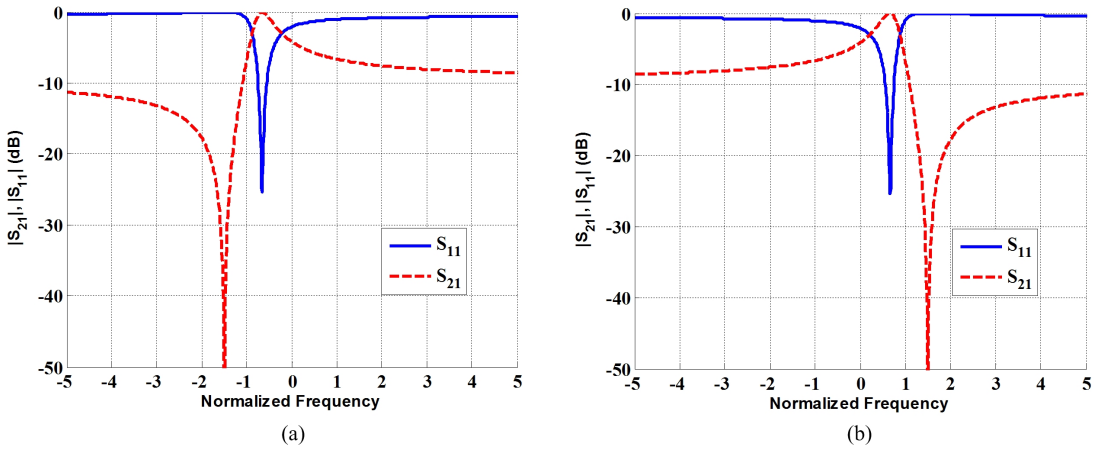

Figure 3.10: a) Typical frequency responses of the singlet resonators shown in a) Fig. 3.9a with a TZ located at $-j1.5$, and b) Fig. 3.9b with a TZ located at $+j1.5$.

five-pole combline filter with two TZs is presented as an example. A single-cavity dual-mode SIW filter with NRNs is also reported in [53]. In the designed filter, with two TZs at both side of the passband, the NRNs are implemented by etching a co-planar waveguide (CPW) on the top layer of the SIW. A new class of dual-mode E-plane waveguide filters using both TM modes and NRNs is introduced in [54]. In these filters, cross couplings between resonating modes are used with NRNs to create very compact and selective filters.

To reduce the manufacturing tolerances, sensitivities of filters, and have more controls on filters' specifications, modular coupling configurations like cascaded singlets, triplets, and quadruplets are interesting. In [51], a six-pole filter is designed, using two triple-mode cavities cascaded by a NRN, and realized in E-plane waveguide technology. An analytical method for designing Chebyshev bandpass filter based on cascaded singlets and including NRNs is introduced in [55]. The procedure is based on the extracted-pole technique and applicable when all TZs are located on the imaginary axis. Cascaded singlets are also used in two-layer microstrip and E-plane waveguide technology to realize bandpass filters [50].

Some research has been conducted on conventional or modularized bandstop filters involving NRNs. In [56], a bandstop microstrip filter is designed based on the cross-coupled resonators model. The NRNs are used in a box configuration which enable designers to modularize the filter and generate the TZs. Two different in-line bandstop configuration based on the extracted-pole techniques are also reported in [9]. In one of them, the NRNs, in an in-line configuration, create a direct path between source

and load. In another one, phase shifters are placed between the NRNs to model the dispersion effects. These two models have been realized in microstrip and E-plane waveguide technology and show good performance.

In this section, we introduce a new and different method to realize a dual-stopband, triple-passband filter based on cascaded singlet in SIW technology.

3.2.1 Filter Design

As described in [48], each singlet can produce one TZ as well as one RZ. Since SIW prototyping is envisioned, the TE_{201} mode is used as resonance while the TE_{10} mode creates the bypass coupling, thus producing a TZ. Using this concept, to create the triple-passband, dual-stopband filter, we first design a 13×13 coupling matrix based on Fig. 3.11b which represents six cascaded singlets, as in (3.12).

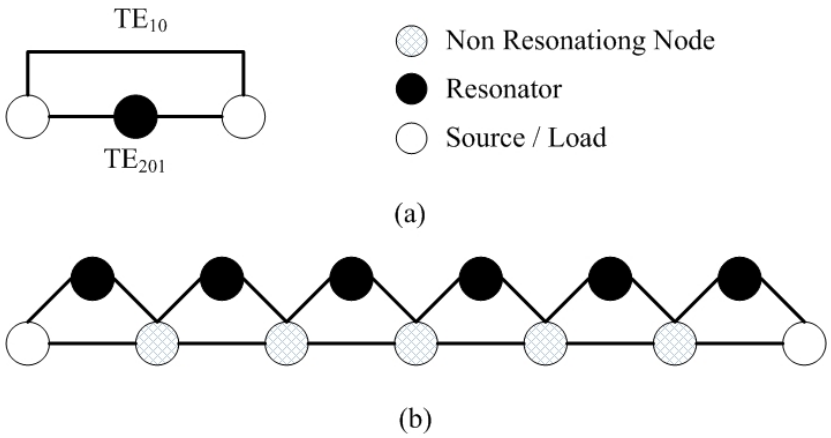

Figure 3.11: a) Configuration of a singlet; b) a passband filter consisting of six singlets.

This coupling matrix is synthesized based on the procedure described in Chapter 2, with some modification to take into account the NRNs. Two stopband center frequencies are selected as 10.25 GHz and 11.23 GHz, with bandwidths of 0.32 GHz and 0.20 GHz, respectively. The center frequencies of the three passbands are 9.72 GHz, 10.76 GHz and 11.76 GHz with bandwidths of 0.39 GHz, 0.37 GHz and 0.39 GHz, respectively. The scattering parameters of this coupling matrix is also shown in Fig. 3.12.

$$M = \begin{pmatrix}
0 & -0.1661 & 0.7353 & 0 & 0 & 0 & 0 & 0 & 0 & 0 & 0 & 0 & 0 \\
-0.1661 & -0.4764 & 0.2853 & 0 & 0 & 0 & 0 & 0 & 0 & 0 & 0 & 0 & 0 \\
0.7353 & 0.2853 & -0.3691 & 0.1724 & 0.8111 & 0 & 0 & 0 & 0 & 0 & 0 & 0 & 0 \\
0 & 0 & 0.1724 & 0.5383 & 0.3447 & 0 & 0 & 0 & 0 & 0 & 0 & 0 & 0 \\
0 & 0 & 0.8111 & 0.3447 & -0.2251 & -0.1412 & -0.6662 & 0 & 0 & 0 & 0 & 0 & 0 \\
0 & 0 & 0 & 0 & -0.1412 & -1.4119 & -0.3439 & 0 & 0 & 0 & 0 & 0 & 0 \\
0 & 0 & 0 & 0 & -0.6662 & -0.3439 & -0.3814 & -0.4715 & 0.4883 & 0 & 0 & 0 & 0 \\
0 & 0 & 0 & 0 & 0 & 0 & -0.4715 & 0.8531 & 0.4876 & 0 & 0 & 0 & 0 \\
0 & 0 & 0 & 0 & 0 & 0 & 0.4883 & 0.4876 & -0.6400 & -0.2377 & 0.88754 & 0 & 0 \\
0 & 0 & 0 & 0 & 0 & 0 & 0 & 0 & -0.2377 & 0.1582 & 0.7064 & 0 & 0 \\
0 & 0 & 0 & 0 & 0 & 0 & 0 & 0 & 0.8754 & 0.7064 & -0.5268 & -0.3979 & 1.3261 \\
0 & 0 & 0 & 0 & 0 & 0 & 0 & 0 & 0 & 0 & -0.3979 & -0.4287 & -0.3142 \\
0 & 0 & 0 & 0 & 0 & 0 & 0 & 0 & 0 & 0 & 1.3261 & -0.3142 & 0
\end{pmatrix} \tag{3.12}$$

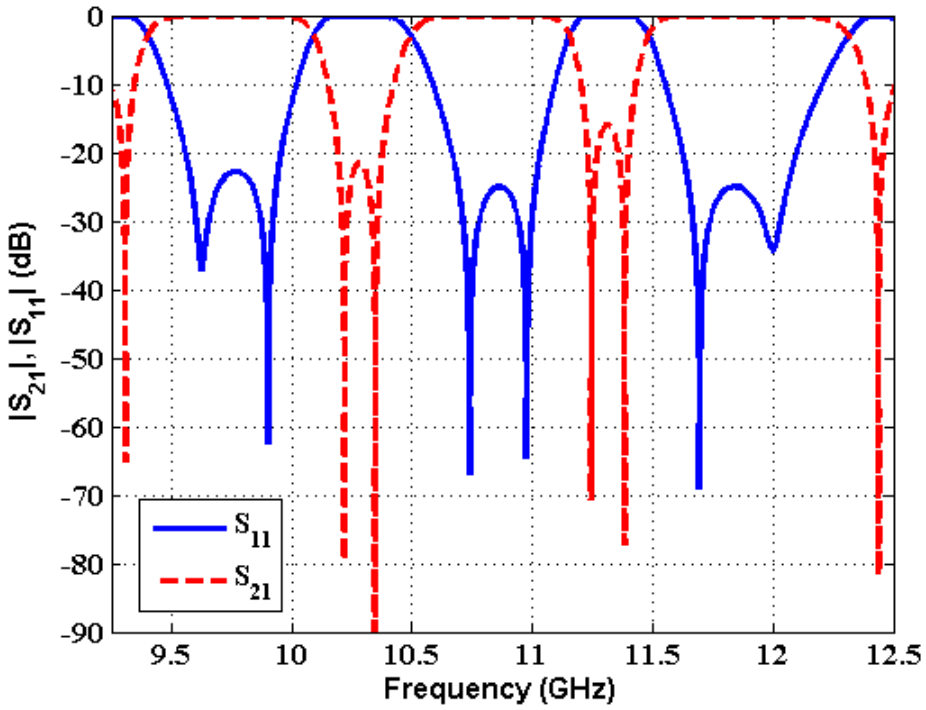

Figure 3.12: Frequency responses of the coupling matrix shown in (3.12).

The second step is to design a six-pole bandpass filter by cascading six singlets

as shown in Fig. 3.11b, using the commercial software package μWave Wizard. The center frequency, bandwidth and return loss of such a wideband filter are 10.75 GHz, 2.35 GHz and 23 dB, respectively. As expected this structure produces six TZs. Each singlet is responsible for one TZ which can be almost independently moved to the left or right side of the passband, or even into the passband. The location of each TZ depends on the relative locations of the input and output apertures of its corresponding singlets. Any changes in the input/output aperture size and location have also a very small effect on the other singlets, but it is not very significant, and some optimization can eliminate these effects. This feature can be used to change the wideband passband filter to a triple-passband, double-stopband one.

In the third step, the designed six-pole wideband bandpass filter is optimized based on the coupling matrix synthesized in the first step to realize a double-stopband, triple-passband filter. For use in a planar application, all filter dimensions are translated to a SIW model, using (3.9).

Finally, the frequency-domain solver of CST is used to simulate and optimize the filter shown in Fig. 3.14a. The chosen substrate for this filter is RT/Duroid 6002 with dielectric constant of 2.94, thickness of 0.508 mm and dielectric loss tangent of 0.0012. The diameter of all via holes is 1 mm, and the cutoff frequency of the input waveguide is 6.5 GHz.

During the optimization process, the length of the second resonator was increased which causes the fundamental TE_{102} mode to start resonating in addition to the TE_{201} mode. To include this resonance, the filter coupling configuration in Fig. 3.11b is updated in Fig. 3.13. Therefore, we synthesized a new 14×14 coupling matrix and continue the optimization of the physical dimensions of the filter based on the new coupling matrix. The normalized coupling matrix of the updated topology shown in Fig. 3.13 is presented in (3.13).

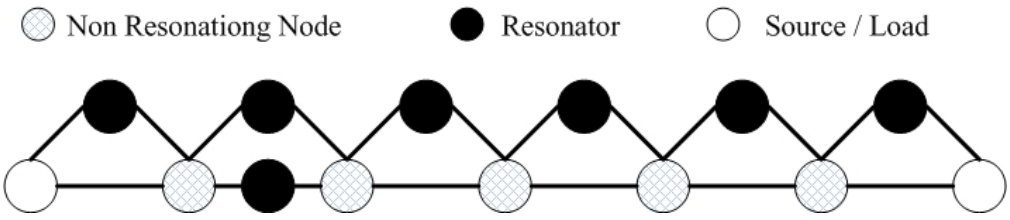

Figure 3.13: Updated coupling scheme of the triple-passband, dual-stopband filter designed in Fig. 3.11b.

The scattering parameters associated with (3.13) are plotted in Fig. 3.14b with

the simulated results. Good agreement between simulated scattering parameters and those calculated from the coupling matrix is observed, especially in terms of TZ and RZ locations. Since the coupling matrix elements are assumed frequency-independent, it is difficult to reach the same return loss in all passbands as well as the attenuation in all stopbands. But simulation includes full-wave frequency-dependent response of the filter. That is the reason for the differences between simulated scattering parameters and those calculated from the coupling matrix in terms of the return loss levels in the passbands and the attenuations in the stopbands.

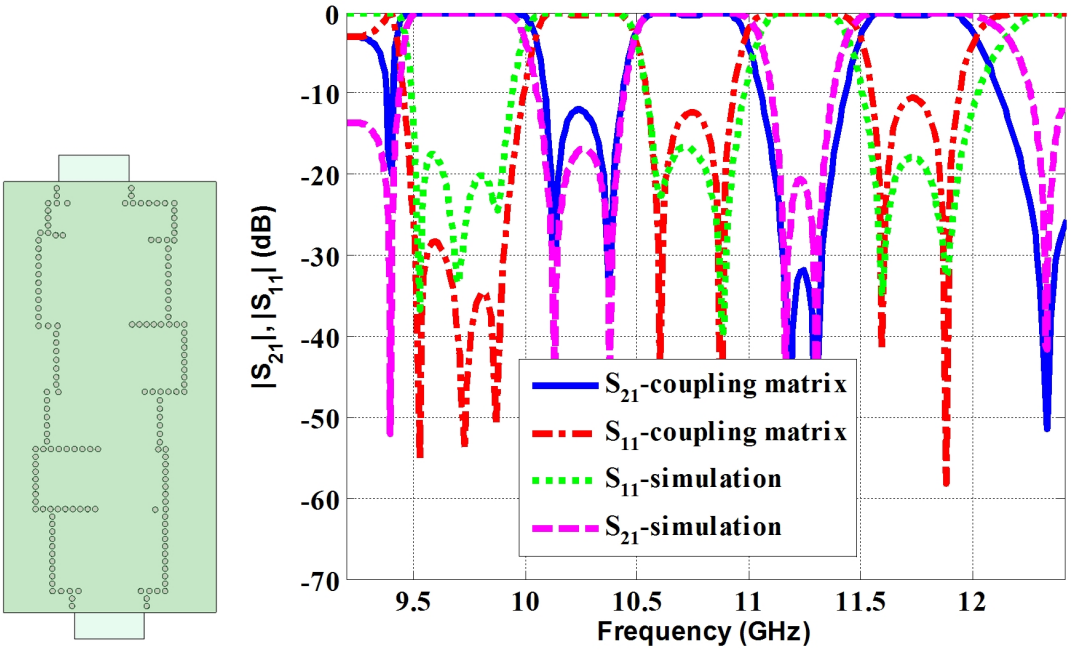

Figure 3.14: a) Triple-passband, dual-stopband filter with waveguide ports; b) scattering parameters of the filter; simulated response (CST) versus coupling matrix (3.13).

$$M = \begin{pmatrix}
0 & -0.0375 & 1.3865 & 0 & 0 & 0 & 0 & 0 & 0 & 0 & 0 & 0 & 0 & 0 \\
-0.0375 & 1.1138 & 0.3772 & 0 & 0 & 0 & 0 & 0 & 0 & 0 & 0 & 0 & 0 & 0 \\
1.3865 & 0.3772 & 0.6685 & -0.4119 & 0.9886 & 0 & 0 & 0 & 0 & 0 & 0 & 0 & 0 & 0 \\
0 & 0 & -0.4119 & -0.7181 & 0 & -0.3733 & 0 & 0 & 0 & 0 & 0 & 0 & 0 & 0 \\
0 & 0 & 0.9886 & 0 & 0.2976 & 0.4316 & 0 & 0 & 0 & 0 & 0 & 0 & 0 & 0 \\
0 & 0 & 0 & -0.3733 & 0.4316 & -0.3177 & -0.7379 & 0.6762 & 0 & 0 & 0 & 0 & 0 & 0 \\
0 & 0 & 0 & 0 & 0 & -0.7379 & -1.4926 & 0.1423 & 0 & 0 & 0 & 0 & 0 & 0 \\
0 & 0 & 0 & 0 & 0 & 0.6762 & 0.1423 & -0.1711 & 0.3045 & 0.8229 & 0 & 0 & 0 & 0 \\
0 & 0 & 0 & 0 & 0 & 0 & 0 & 0.3045 & -0.4520 & 0.2532 & 0 & 0 & 0 & 0 \\
0 & 0 & 0 & 0 & 0 & 0 & 0 & 0.8229 & 0.2532 & -0.4707 & -0.2082 & 0.6983 & 0 & 0 \\
0 & 0 & 0 & 0 & 0 & 0 & 0 & 0 & 0 & -0.2082 & 0.0931 & 0.4429 & 0 & 0 \\
0 & 0 & 0 & 0 & 0 & 0 & 0 & 0 & 0 & 0.6983 & 0.4429 & -0.2820 & -0.2948 & 1.2374 \\
0 & 0 & 0 & 0 & 0 & 0 & 0 & 0 & 0 & 0 & 0 & -0.2948 & 0.3563 & 0.3727 \\
0 & 0 & 0 & 0 & 0 & 0 & 0 & 0 & 0 & 0 & 0 & 1.2374 & 0.3727 & 0
\end{pmatrix} \tag{3.13}$$

3.2.2 Experimental Results

The triple-passband, dual-stopband filter has been prototyped as shown in Fig. 3.15a. Measurements were carried out with a vector network analyzer and Thru-Reflect-Line (TRL) calibration standards, which ideally calibrate out the coaxial (SMA)-to-microstrip and microstrip-to-SIW transitions.

The measured results are compared with simulated responses in Fig. 3.15b. Good agreement between simulated and measured transmission coefficients is achieved, especially with respect to the locations of the TZs and RZs. The measured passband return losses are 9.63 dB, 9.17 dB and 13.22 dB, with minimum insertion losses of 0.33 dB, 0.45 dB and 0.3 dB, respectively. The minimum measured attenuations in the two stopbands are 15.48 dB and 18.56 dB which agree reasonably well with the simulations. The slight upward frequency shift is well within the limit of the substrates permittivity of 2.94 ± 0.04. Moreover, the vias appear to have been drilled slightly larger than the nominal value of 1 mm. That reduces the effective resonator widths and length, and thus the filter's responses shift upward in frequency. The remaining differences, especially in return loss levels, are attributed to the differences in soldering coaxial connectors to the calibration standards and the filter structure.

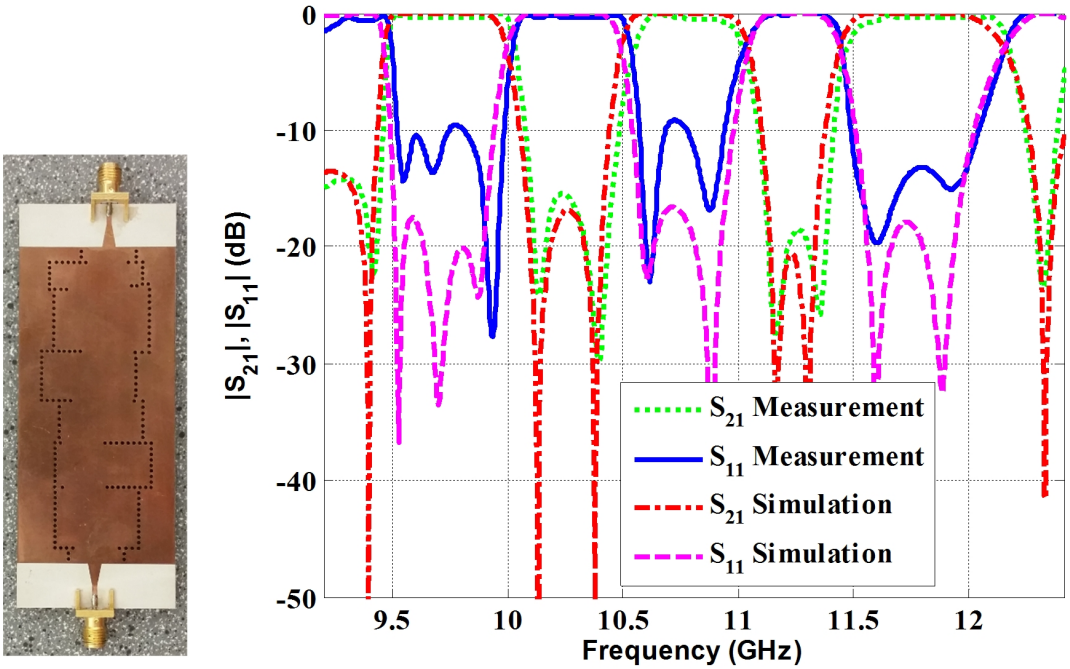

(a) (b)

Figure 3.15: a) Triple-passband, dual-stopband SIW filter with coaxial ports and microstrip-to-SIW transitions; b) comparison between measured and simulated scattering parameters of the filter.

Chapter 4

Enhanced Bandstop Filters Based on Conventional Design Methods

Although significant advances in microwave filter designs have been achieved over the last few decades, many of the design procedures for RF and microwave filters are still based on Cohn's paper [3]. This classical approach has three main steps. First, an equivalent circuit prototype, consisting of lumped and/or distributed elements, is synthesized using mathematical models. Then the prototype elements are appropriately related to physical elements of the filter. Finaly, optimizations of the filter dimensions are usually performed. One of the advances in the filter design field is introducing enhanced equivalent circuits for filters by including the electromagnetic behavior of filter elements in their equivalent circuits.

Different conventional methods are used to design bandstop filters, including traditional approaches such as bandstop stubs [57–59] and defected ground structures [32, 60, 61]. Newer methods include nonresonating nodes filters, extracted-pole techniques [9, 62], and signal interference methods [63–65].

In this chapter, we synthesize, prototype and measure several new bandstop filters in microstrip and substrate integrated waveguide (SIW) technologies.

4.1 Microstrip Bandstop Filters Using T- and L-Shaped Resonators

Among all available bandstop filter technologies, microstrip filters have the lowest manufacturing cost and weight which make them suitable for low-power applications.

Recent developments of microstrip filters have been driven by technologies such as high temperature superconductors (HTS), ferroelectrics, microelectromechanical systems (MEMS), hybrid or monolithic microwave integrated circuits (MMICs), photonic bandgap (PBG) materials/structures, and low temperature cofired ceramics (LTCCs).

Topologies of microstrip filters depend on the filters' characteristics such as Chebyshev or elliptic, bandwidth, size and power handling. In addition, in microstrip filters, an appropriate substrate should be chosen based on the desired filter size, higher order modes, surface mode effects, dielectric losses, temperature stability and power handling (dielectric strength and thermal conductivity). The operating frequency of a microstrip filter should be kept below the cut-off frequency of the first higher order mode calculated by [17]

$$f_c = \frac{c}{\sqrt{\epsilon_r}(2W + 0.8h)} \tag{4.1}$$

where c is the velocity of light in the free space, and ϵ_r is the dielectric constant of the substrate. W and h are the width of the microstrip and substrate thickness, respectively. The operating frequency should be also below the frequency of f_s [17]

$$f_s = \frac{ctan^{-1}(\epsilon_r)}{\sqrt{2}\pi h\sqrt{(\epsilon_r - 1)}} \tag{4.2}$$

At frequency of f_s, the surface mode is strongly coupled to the dominant mode of the microstrip, because the phase velocities of the two modes are close.

The maximum power handled by a microstrip line is calculated by

$$P_{max} \propto \frac{V_0^2}{2Z_0} \tag{4.3}$$

where V_0 is the maximum breakdown voltage of the substrate and Z_0 is the characteristic impedance of the microstrip. Narrower band filters result in higher electric field density and consequently lower maximum power handling.

Most of the traditional microstrip bandstop filters suffer from narrow bandwidth [66–68]. Therefore, some wideband microstrip bandstop filters have been reported recently containing short- or open-ended parallel coupled-line sections. In [69], a compact wideband bandstop filter with three transmission zeros (TZs) in the stopband is introduced. The filter is constructed by using single quarter-wavelength resonators and a section of anti-coupled lines with short circuits at one end. Another general circuit configuration for wideband bandstop filters based on cross-couplings is pre-

sented in [70]. A very compact wideband bandstop filter is also reported in [71] using two coupled-line sections in parallel. An interesting bandstop filter is introduced in [72] based on signal interference techniques. The structure in [72] is formed by an open-ended coupled-line section connected in parallel to a transmission line. Another novel transmission line configuration is proposed in [73] to design a sharp-rejection wideband bandstop filter. A compact parallel-coupled transmission line section, connected at both ends, is presented in [63] to obtain a wideband bandstop filter with five transmission zeros in the stopband.

In this section, we introduce relatively wideband bandstop filters consisting of a microstrip transmission line loaded with a T-shaped and two L-shaped resonators. The analytic investigation shows that the filter produces two transmission zeros (TZs) in the stopband as well as three reflection zeros (RZs) in the lower and upper passbands. This method is a good substitute for wideband bandstop filter designs using parallel coupled-line sections, especially when tight coupling values are not realizable due to manufacturing limitations. In addition, the design process is simpler than filters using coupled-line sections with shorted transmission lines. Despite the C- and S-band wideband bandstop microstrip filters mentioned before, the new filters presented in this section are designed to work at X- and Ku-band frequencies.

4.1.1 Filter Design

A microstip transmission line loaded with a commensurate L resonator is modeled by a coupled line section connected to a commensurate open circuit stub at one end. Fig. 4.1a shows the circuit and Fig. 4.1b presents the extracted equivalent circuit in the p-domain [57].

The variable p is simply converted to regular frequency, f, by applying

$$p = jtan(\frac{\pi}{2}\frac{f}{f_0}) \tag{4.4}$$

where f_0 is the frequency at which the commensurate length, L, is $\lambda_0/4$. Quantities n, Z_1, Z_2 and Z are the equivalent circuit parameters calculated from the physical characteristics of the circuit including the spacing between coupled lines, width and length of the L resonator's arms, substrate height, dielectric constant and thickness of metalization. For details, the reader is referred to [57]. The unit element (UE) is a transmission line section with characteristic impedance $Z_1 = 1/Y_1$ and length L,

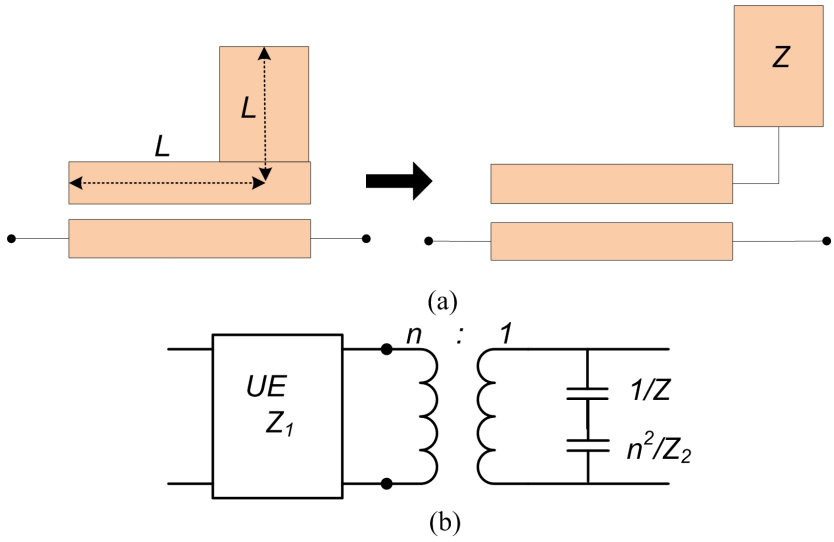

Figure 4.1: a) Commensurate L resonator; b) its equivalent circuit in the p-domain.

whose admittance matrix is

$$[Y]_{UE} = \begin{bmatrix} \frac{Y_1}{p} & -\frac{\sqrt{1-p^2}Y_1}{p} \\ -\frac{\sqrt{1-p^2}Y_1}{p} & \frac{Y_1}{p} \end{bmatrix} \tag{4.5}$$

The ABCD matrix of the unit element is calculated using its admittance matrix, $[Y]_{UE}$

$$\begin{bmatrix} A & B \\ C & D \end{bmatrix}_{UE} = \begin{bmatrix} \frac{-Y_{22}}{Y_{21}} & \frac{-1}{Y_{21}} \\ \frac{-(Y_{22}Y_{11}-Y_{21}Y_{12})}{Y_{21}} & \frac{-Y_{11}}{Y_{21}} \end{bmatrix} \tag{4.6}$$

Fig. 4.2a shows a microstrip filter on RT/Duroid 6002 substrate with thickness of 0.508 mm. It consists of two identical commensurate L resonators separated by a section of transmission line. Its equivalent circuit is depicted in Fig. 4.2b. The characteristic impedance of the microstrip line section is Z_0=50 Ω, and the dimensions of the resonators are chosen appropriately to create a stopband at 9.80 GHz. The transmission matrices of the right transformer, $[ABCD]_n$, the total capacitance connected in parallel to each transformer, $[ABCD]_{Ct}$, and the 50-Ω transmission line

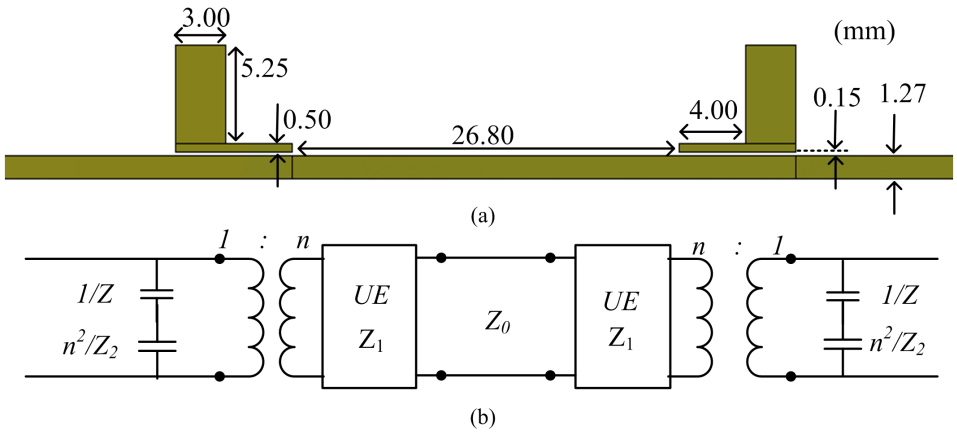

Figure 4.2: a) Bandstop filter created by two commensurate L resonators; b) its equivalent circuit.

section located between them, $[ABCD]_{TL}$, are given by

$$\begin{aligned}
\begin{bmatrix} A & B \\ C & D \end{bmatrix}_n &= \begin{bmatrix} n & 0 \\ 0 & \frac{1}{n} \end{bmatrix} \\
\begin{bmatrix} A & B \\ C & D \end{bmatrix}_{ct} &= \begin{bmatrix} 1 & 0 \\ Y_{ct} & 1 \end{bmatrix} \\
\begin{bmatrix} A & B \\ C & D \end{bmatrix}_{TL} &= \begin{bmatrix} cos\theta_{TL} & jZ_0 sin\theta_{TL} \\ jY_0 sin\theta_{TL} & cos\theta_{TL} \end{bmatrix}
\end{aligned} \tag{4.7}$$

where θ_{TL} is the electrical length of the 50-Ω transmission line section and the quantity Y_{ct} is the admittance of total capacitance $ct = \frac{n^2}{(n^2 Z + Z_2)}$. The scattering parameters of this circuit are obtained by applying the $ABCD$ matrix analysis

$$\begin{bmatrix} A & B \\ C & D \end{bmatrix} = \begin{bmatrix} A_{ct} & B_{ct} \\ C_{ct} & D_{ct} \end{bmatrix} \begin{bmatrix} A_n & B_n \\ C_n & D_n \end{bmatrix}^{-1} \begin{bmatrix} A_{UE} & B_{UE} \\ C_{UE} & D_{UE} \end{bmatrix} \begin{bmatrix} A_{TL} & B_{TL} \\ C_{TL} & D_{TL} \end{bmatrix} \begin{bmatrix} A_{UE} & B_{UE} \\ C_{UE} & D_{UE} \end{bmatrix} \begin{bmatrix} A_n & B_n \\ C_n & D_n \end{bmatrix} \begin{bmatrix} A_{ct} & B_{ct} \\ C_{ct} & D_{ct} \end{bmatrix} \tag{4.8}$$

The scattering parameters of the $ABCD$ matrix in (4.8) are shown in Fig. 4.3 along with simulated results in CST. The structure produces two identical TZs in the stopband and several out-of-band RZs due to the length of the transmission line between the two L resonators. Some discrepancies are observed at frequencies far from the center frequency f_0. The differences are due to the fact that the presented equivalent circuit in Fig. 4.2b is more accurate at frequencies close to the center frequency f_0.

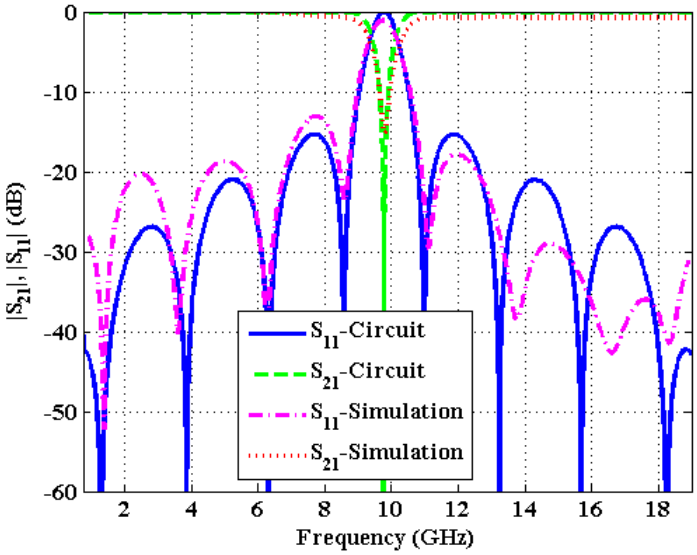

Figure 4.3: Equivalent circuit and CST responses of the filter in Fig. 4.2.

A T-shaped resonator and its equivalent circuit are obtained by treating it as two back-to-back L resonators as shown in Fig. 4.4. The dimensions of the T resonator are chosen to obtain a stopband at 9.5 GHz. The equivalent circuit response of this T resonator is compared to that of CST in Fig. 4.5, and good agreement is observed.

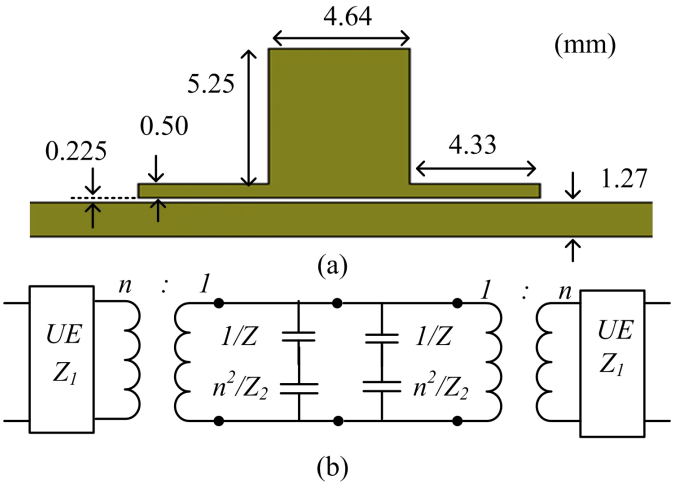

Figure 4.4: a) The inverse T resonator; b) its equivalent circuit.

ABCD matrix analysis shows that combining the two L resonators in Fig. 4.2 with the T resonator in Fig. 4.4 results in a new bandstop filter with two TZs in the stopband and three RZs in the upper and lower passbands. The locations of three of

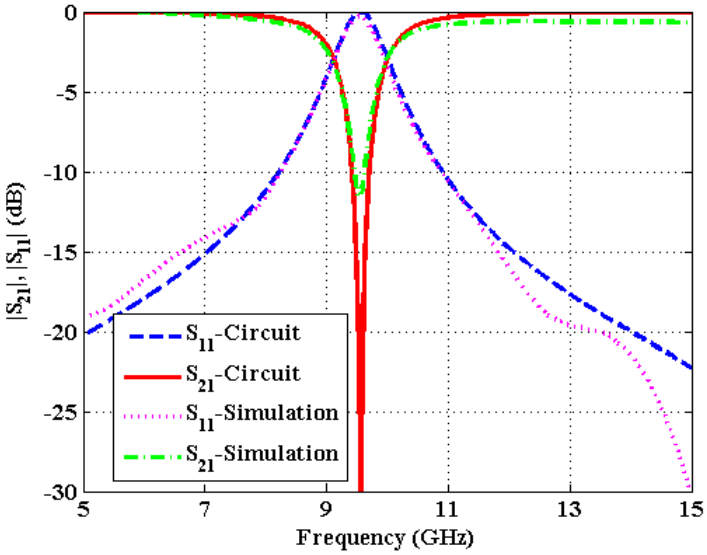

Figure 4.5: Equivalent circuit and CST responses of the filter in Fig. 4.4.

the RZs presented in Fig. 4.3 can be effectively controlled by the physical dimensions of the filter so that a return loss better than 10 dB is achievable in the passbands. Note that the other RZs shown in Fig. 4.3 move to frequencies far from the stopband (as is shown for one of them in Fig. 4.7).

Fig. 4.6 represents the final design of the filter. In comparison to Fig. 4.2 and Fig. 4.4, a few dimensions are slightly optimized. The simulated scattering parameters of

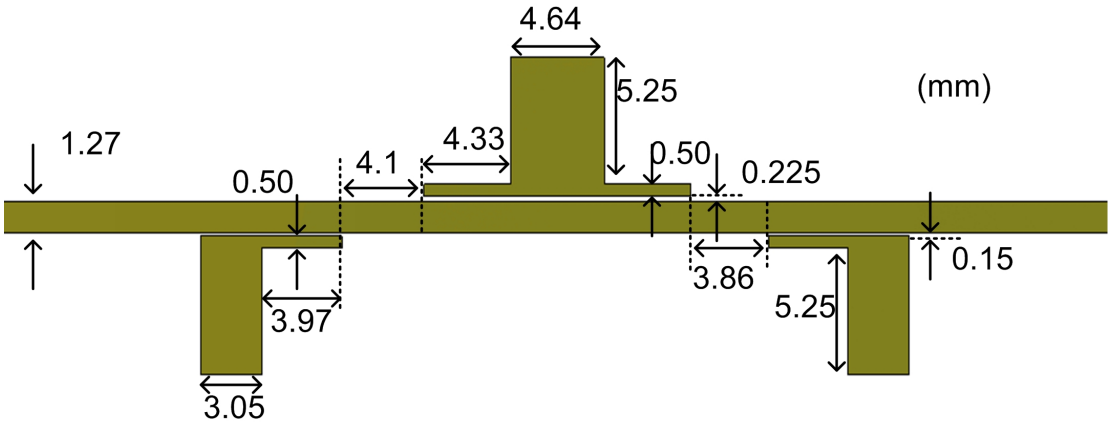

Figure 4.6: Final configuration of the designed filter.

the proposed filter are shown in Fig. 4.7 with the equivalent-circuit response for comparison. The CST simulation confirms the location of RZs and TZs predicted by

the equivalent circuit model. The center frequency of the filter is 9.72 GHz which is in between the resonant frequencies of the T and L resonators. The fractional bandwidth of the filter is 10.9%.

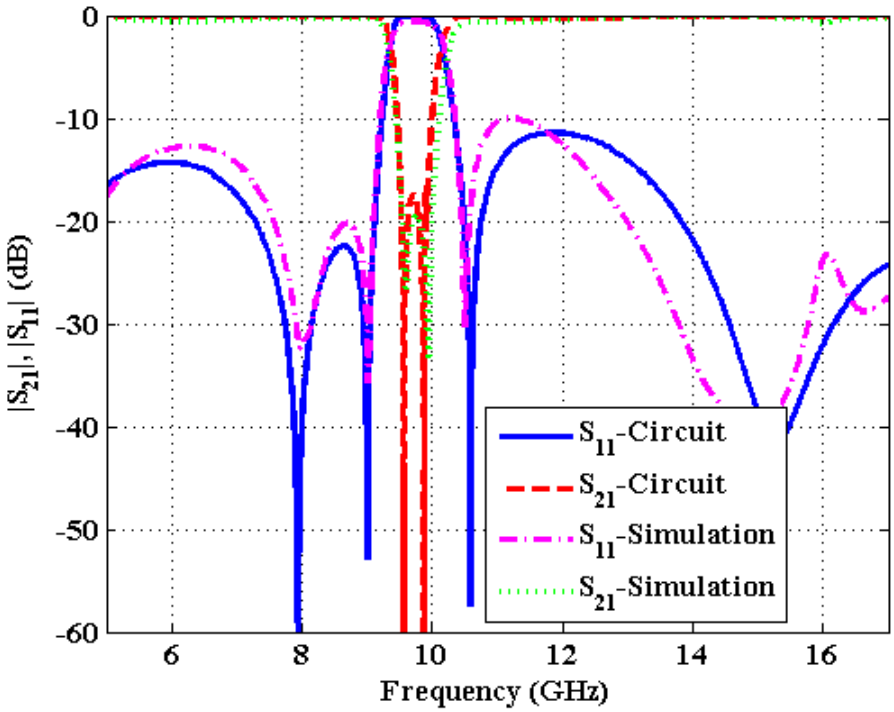

Figure 4.7: Equivalent circuit and CST responses of the filter in Fig. 4.6.

4.1.2 Experimental Results

A top view of the prototyped filter is depicted in Fig. 4.8a. A Thru-Reflect-Line (TRL) calibration kit is used to deembed the effects of transitions to coaxial ports. Fig. 4.8b shows the comparison between simulated and measured results. Good agreement is observed. The locations of the simulated TZs and RZs are well reproduced in the measurements. The measured stopband attenuation is better than 16 dB, and the return loss in the lower passband is better than 12 dB while that in the upper passband is better than 10 dB.

The analytic investigation is carried out based on commensurate resonators. However, CST simulations show that also non-commensurate L- and T-shaped resonators are capable of creating relatively wideband bandstop filters with three RZs. A non-commensurate filter, with center frequency of 14.77 GHz and bandwidth of 0.97 GHz,

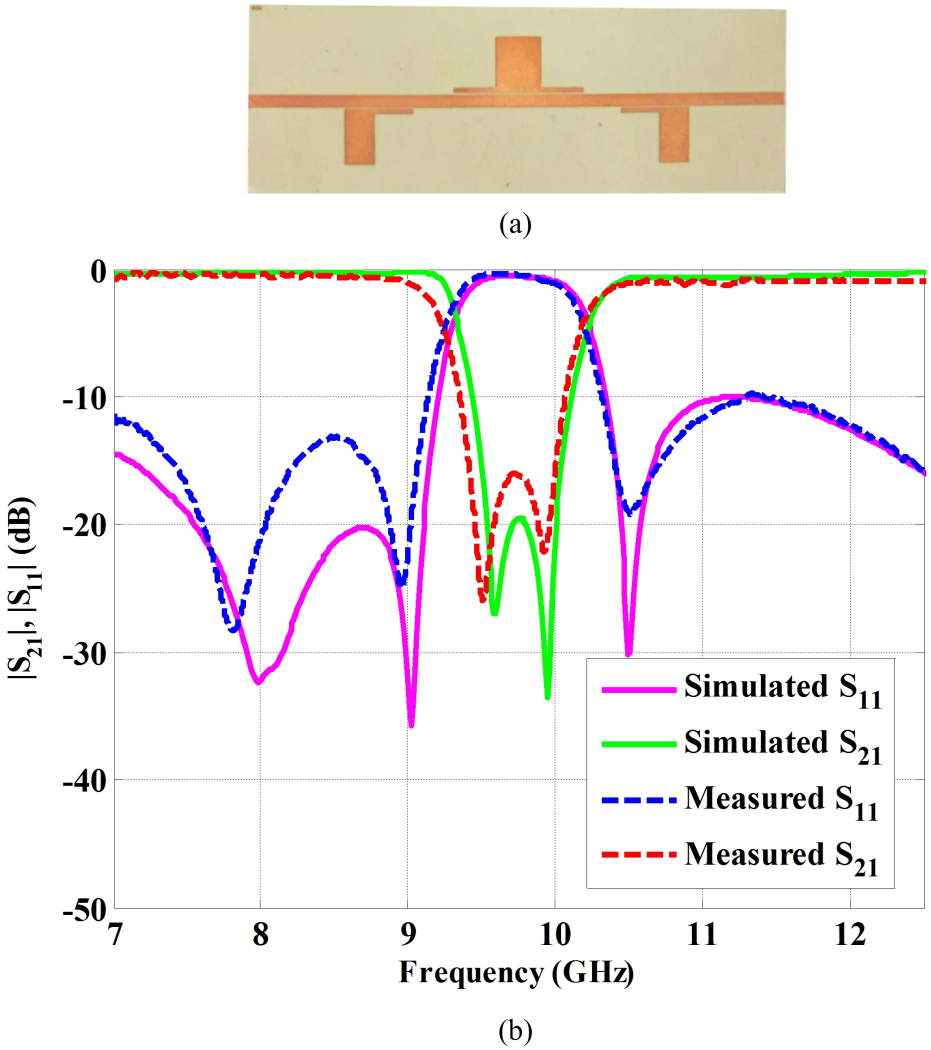

Figure 4.8: a) Prototyped commensurate microstrip wideband bandstop filter; b) simulated and measured responses of the filter.

is designed and prototyped as shown in Fig. 4.9a. Fig. 4.9b compares the measured responses of the filter with simulations. The locations of the simulated TZs and RZs are well confirmed by measurements. The stopband attenuation is better than 22 dB. The return loss in both lower and upper passbands is better than 10 dB.

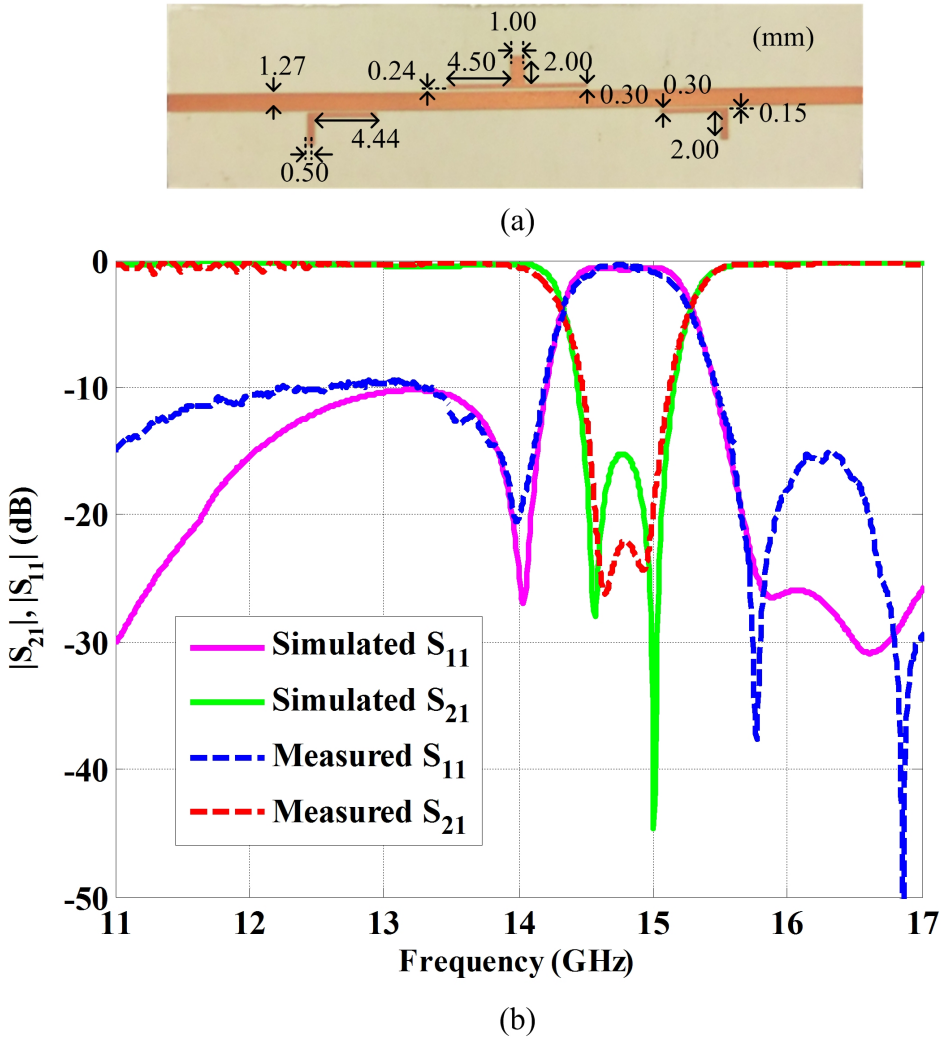

Figure 4.9: a) Prototyped non-commensurate microstrip bandstop filter; b) simulated and measured responses of the filter.

4.2 Dual-Band SIW Bandstop Filter Using H-Plane Stubs

Conventional bandstop stubs are one of the oldest methods for creating bandstop filters [5]. Quarter-wavelength open-circuited stubs look like series LC bandstop resonant circuits (Fig. 4.10a). Thus, as shown in Fig. 4.10b, a narrow bandstop filter can be realized by cascading quarter-wavelength open-circuited stubs spaced by quarter-wavelength transmission line sections. This traditional bandstop filter has usually large physical dimensions, and the first higher resonance appears at three times the fundamental resonant frequency. Series stubs are not practical in H-plane waveguide (SIW) technology but are usually used in E-plane waveguide filters.

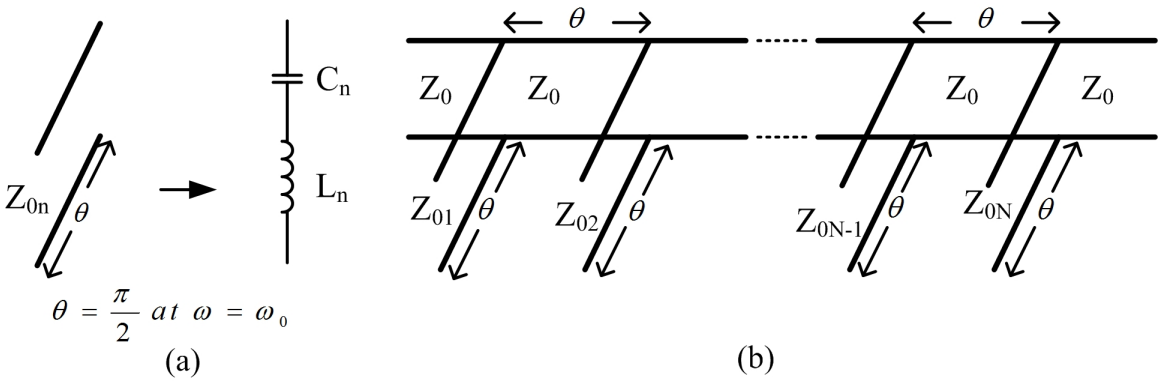

Figure 4.10: a) Equivalent circuit of a quarter-wavelength open-circuited stub; b) bandstop filter using shunt transmission line resonators.

The bandstop stub can be used in different physical shapes other than its conventional shape to realize bandstop filters with modified characteristics. A compact wideband bandstop filter is reported in [58] based on a combination of bandstop stub and spurline. Due to the inherent compact characteristics of the spurline, this filter has a better rejection performance than an open-stub filter. In [30], open stubs are used in the stepped-impedance form to realize a narrow dual-band bandstop filter in microstip technology. Another dual-band bandstop microstrip filter is presented in [31] based on composite shunt open stubs. An algorithm for the analysis of waveguide bandstop filters using partially filled H-plane stubs is introduced in [74]. In [75], the authors change the conventional open stubs to T-shape ones to create a more compact bandstop filter with second harmonic suppression. A very wideband microstrip bandstop filter using double resonant stubs is investigated in [76]. In [77], a

compact pseudo-elliptic bandstop filter is presented using three stubs with different length. A uniplanar wideband bandstop filter is also reported in [78] using two bent open stubs.

In this section, we use bandstop H-plane stubs in a new configuration to create a dual bandstop filter in SIW technology. In our design, three stubs with slightly different lengths are connected to a transmission line with three coupling apertures. The second and third resonant harmonics of each stub contribute to creating two stopbands.

4.2.1 Equivalent Lumped Element Circuit for Dual-Band Bandstop Filters

Each bandstop resonator element is modeled by a shunt LC circuit as shown in Fig. 4.11a. For the design of a dual-stopband filter with three TZs in each stopband, we cascade six shunt LC circuits resonating at different centre frequencies. All shunt LC circuits are separated by 90° transmission lines (Fig. 4.11b). Given the resonance frequency ω_0 and 3 dB bandwidth of each resonator ω_c, L_i and C_i for each shunt LC circuit can be calculated from

$$\begin{aligned} \omega_{0i} &= 1/\sqrt{L_i C_i} \\ C_i &= \frac{\omega_c}{2Z_0(\omega_0^2 - \omega_c^2)} \end{aligned} \tag{4.9}$$

An optimization process is applied to obtain two stopbands at centre frequencies of 10 GHz and 12.2 GHz with corresponding bandwidth of 360 MHz and 500 MHz, respectively. While C_i and L_i determine the locations of the TZs, coupling factors M_i determine the positions of the RZs by scaling the total admittance of each shunt LC circuit by the factor M_i. Table 4.1 shows the final inductor, capacitor and coupling values after optimization.

To implement such a filter in SIW technology, we use CST Microwave Studio to simulate a loaded uniform SIW line with three quarter-wavelength H-plane stubs spaced by quarter-wavelength sections (Fig. 4.12a). Each stub is connected to the main SIW waveguide by an inductive apperture. RT/Duroid 6002 with ϵ_r=2.94, loss tangent of 0.0012, and height of 3.048 mm is chosen as substrate. The diameters of all via holes are 1 mm. The second and third higher order modes of each H-plane stub resonator contribute to the first and second stopbands, as shown in Fig. 4.13.

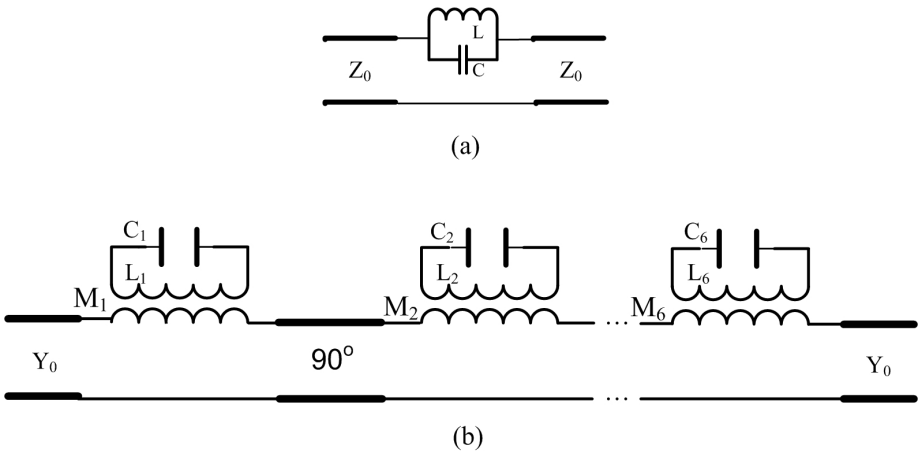

Figure 4.11: a) Single bandstop resonator; b) equivalent lumped element circuit of the dual-band bandstop filter.

We insert a partial-height via hole into the SIW circuit to improve the return loss of the passband located between the two stopbands (Fig 4.12b).

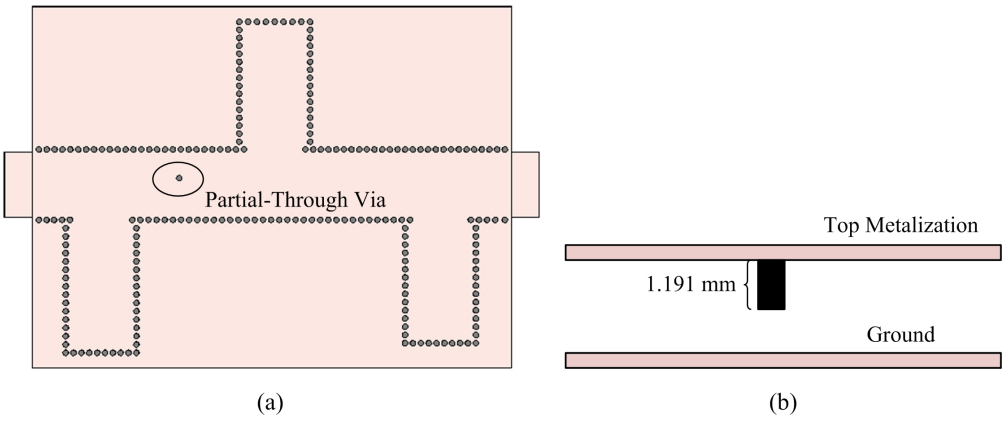

Figure 4.12: Dual-band bandstop SIW filter, containing the partial-height via hole, with waveguide port; a) top view of the filter, b) side view of the partial-height via hole.

The responses of the equivalent circuit in Fig. 4.11b are compared with simulated results in Fig. 4.14. The two stopbands and their TZs are well reproduced in the simulations. In the equivalent circuit, very simple LC circuits have been chosen to represent the resonators, while simulated results present the full-wave frequency-dependent response of the filter. That explains some discrepancies between simulated results and equivalent circuit results, especially in the passband. Fig. 4.15 demonstrates the ability of the capacitive post to slightly improve the passband return loss

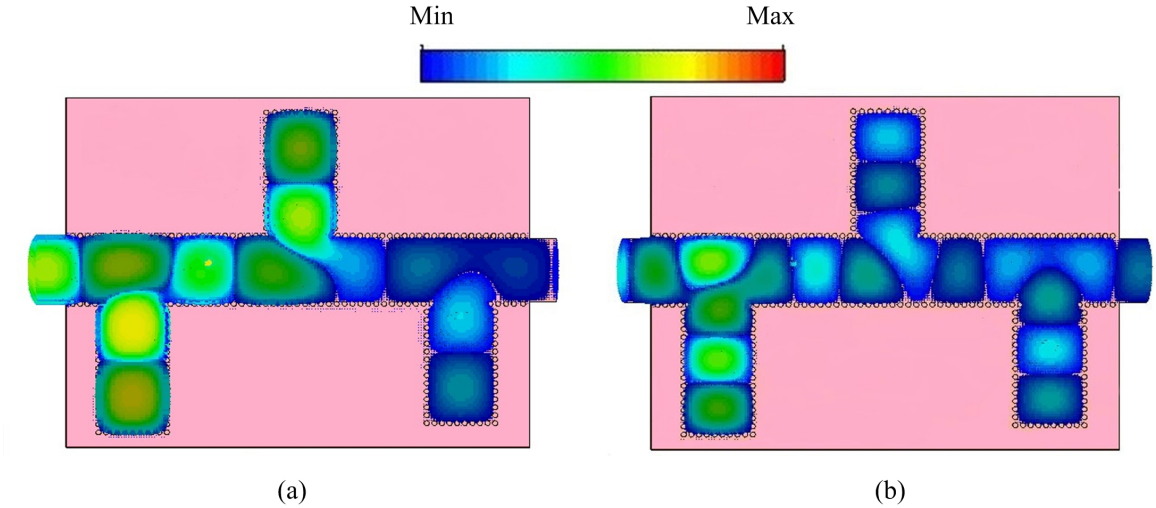

Figure 4.13: Electric field distributions in the designed filter; a) at 10 GHz, b) at 12.2 GHz

without affecting the stopband performance.

Table 4.1: Parameters values of the equivalent circuit in Fig. 4.11b.

i	C_i (pF)	L_i (μH)	M_i
1	5.34	48.84	1.34
2	2.98	84.81	1.35
3	2.69	91.36	1.11
4	2.44	72.56	0.90
5	1.72	97.85	0.95
6	3.64	44.64	0.88

4.2.2 Simulated and Measured Results

The designed dual-stopband SIW filter is prototyped, and a photograph of it is depicted in Fig. 4.16a. Note that microstrip-to-SIW transitions in Fig. 4.16a are used for measurement purposes. These transitions have wider 50 Ω microstrip widths due to the thick substrate used. For measurements, a Thru-Reflect-Line (TRL) calibration kit is used to deembed the effects of coaxial connectors and microstrip-to-SIW transitions.

The measured and simulated performances are compared in Fig. 4.16b. It is observed that the experimental results reproduce the locations of TZs and RZs with

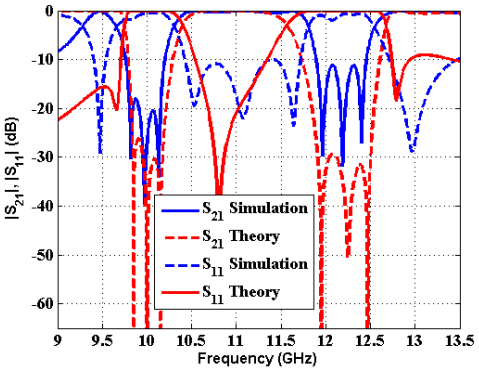

Figure 4.14: Scattering parameters of the dual-band bandstop filter; comparison between the equivalent circuit and simulation (CST) responses.

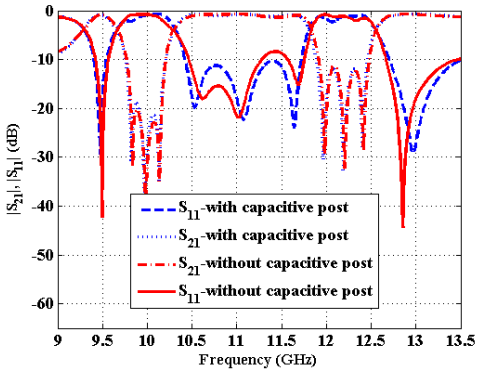

Figure 4.15: Simulated scattering parameters (CST) of the dual-band bandstop SIW filter with and without capacitive post.

good accuracy. Moreover, the attenuation in both stopbands as well as the passband return loss are well represented.

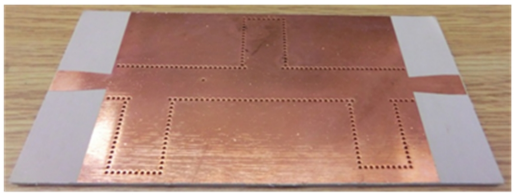

(a)

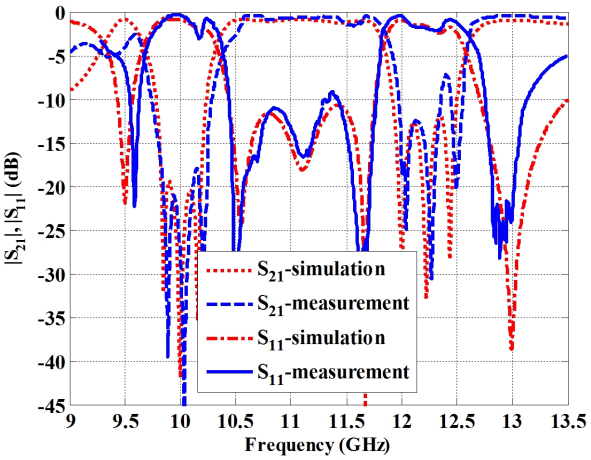

(b)

Figure 4.16: a) Photograph of the fabricated dual-band bandstop filter in SIW technology; b) comparison between measured and simulated scattering parameters of the filter.

4.3 Extracted-Pole Technique and Its Application to Wideband Ridged Bandstop Filter Design

The concept of substrate integrated waveguide (SIW) has developed into a mature technology that continues to replace all-metal waveguide components in many applications [79]. Due to its planar nature, SIW circuits have so far been limited to comparison with and substitution of H-plane waveguide components. In waveguide technology, many advantages are derived from ridged waveguides, especially in wideband filter applications [80–83].

Although all-metal ridged waveguide filters have good insertion loss characteristics, they are bulky and are difficult to integrate into planar microwave or millimetre-wave circuits. In addition, they are relatively expensive to manufacture. SIW technology, as alternative, enables designers to produce planar circuits which can be integrated with other planar structures. They also have better insertion loss characteristics than conventional planar circuits such as microstrip or coplanar waveguide. Due to the possible use of standard printed-circuit board facilities, manufacturing costs of SIW filters are much lower than comparable all-metal waveguide filters.

To translate the ridged waveguide principle to SIW, a ridged SIW waveguide is introduced in [84] with partial-height via holes in the center of the SIW and fully plated-through vias as side walls. Another ridged SIW is introduced in [85], which is similar to the structure presented in [84], with an additional metallic strip, connecting the ends of the partial-height via holes. The modified structure presented in [85] shows wider bandwidth compared with that introduced in [84]. The bandwidths of the prototyped structures in [85] are three times wider than classical rectangular waveguides or SIWs, and their sizes are reduced by half in comparison with a SIW with the same cutoff frequency. However, filter components based on SIWs with partial-height via-holes, or so-called ridged SIWs, have not been presented so far.

Therefore, to demonstrate the feasibility of partial-height via holes in SIW filters, this section presents, for the first time, the design, simulation, prototyping and measurement of a three-pole SIW wideband and compact bandstop filter with partial-height via holes (modified ridged SIW). In the design procedure, the partial-height via holes are selected as resonators whose interactions can produce a large variety of couplings resulting in wideband bandstop filter realization. The design procedure is based on the extracted-pole technique which is reviewed in this section.

4.3.1 Extracted-Pole Technique

The extracted-pole technique is one of the most well-known methods to realize transmission zeros (TZs) that result in a sharp roll-off in bandpass filters. The main advantage of this technique is the independent generation and control of TZs. It is first introduced in 1980 to analytically synthesize symmetric bandpass filters with finite real TZs [86]. In the synthesized lowpass prototype, the real TZs are extracted from both ends of the two-port network and realized by simple resonators separated by phase shifters. The method in [86] is extended to asymmetric bandpass filters as well as symmetric ones in [87]. A method presented in [88] realizes an in-line bandpass filter with one or two TZs extracted at the input and output, but without using phase shifters between resonators. Instead, frequency-independent reactances at the input and output are used. This method is verified by designing several waveguide cavity filters. Macchiarella [89] obtains similar results by starting from triplets at the input and output and then carrying out a series of circuit transformations to convert the circuit into an in-line configuration. A more general extracted-pole method is introduced in [90] for synthesizing in-line bandpass filters with N TZs. This method is applied to the synthesis of several low-cost bandpass H-plane waveguide filters. The method presented in [90] is also used in [62] to design a four-pole SIW bandpass filter, albeit without partial-height (ridged) via holes.

As opposed to bandpass filters, only a few papers report on extracted-pole bandstop filters. A general extracted-pole technique for synthesizing bandstop filters with arbitrarily placed reflection zeros (RZs) is presented in [9]. In this method, the resonators are connected to the main line by inverters and separated by frequency-independent phase shifters in an in-line configuration. The frequency-independent phase shifters can be optimized prior to final realization to take into account their actual frequency dependence. Amari et al. [9] use their method to synthesize and prototype a third-order E-plane bandstop filter with three RZs above the stopband. A new band-reject element is introduced in [91] to realize broadband bandstop filters. The element is a partial-height post in an all-metal rectangular cavity. The length of the post and its offset from the waveguide center determine the locations of TZs and the amount of couplings, respectively. This new band-reject element permits to achieve a wide range of couplings, from weak to strong and causes a broad stopband with both symmetric and asymmetric responses. A second-order waveguide bandstop filter based on this method is prototyped in [91].

4.3.2 Lowpass Equivalent Circuit Extraction of the Ridged SIW Bandstop Filter

In this section, we design a third-order ridged SIW bandstop filter with three RZs located above the stopband. In this filter, the resonators are three partial-height plated via holes in a relatively thick substrate. The resonators are separated by phase shifters and coupled to the main SIW line by inverters. The heights of the partial-height via holes and their offset from the center of the main SIW line determine the locations of TZs and the coupling coefficients, respectively. Input and output couplings are also required for filter realization and realized as inductive irises by using additional plated-through via holes. For this design, the bandwidth, center frequency and attenuation in the stopband are 1.58 GHz, 10.74 GHz and 32 dB, respectively. The normalized passband RZs are at normalized angular frequencies of 2.4648, 3.5242 and 4.5839 using the well-known frequency conversion formula

$$s = j\Omega = \frac{f_0}{BW}\left(\frac{f}{f_0} - \frac{f_0}{f}\right) \tag{4.10}$$

where f_0 and BW are the center frequency and the bandwidth of the filter. The first step is to model a ridged SIW bandstop filter with a lowpass equivalent circuit based on the extracted-pole technique presented in [9], as shown in Fig. 4.17.

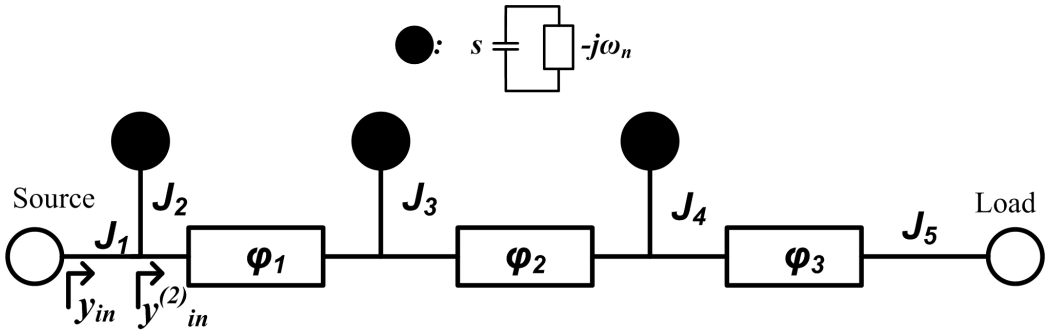

Figure 4.17: Equivalent lowpass circuit for third-order extracted-pole bandstop filters according to [9].

To extract the elements of the network, we need to determine the locations of the TZs. The reflection coefficient of a bandstop filter is related to the filtering function, $C_N(\omega)$, by

$$|S_{11}|^2 = \frac{1}{1 + \epsilon^2 C_N^2(\omega)} \tag{4.11}$$

The parameter ϵ is related to the bandstop attenuation, IL, by $\epsilon = \left(10^{\frac{-IL}{10}} - 1\right)^{\frac{-1}{2}}$. A Chebyshev filtering function is obtained from

$$C_N(\omega) = cosh\left[\sum_{n=1}^{n=N} cosh^{-1}\left(\frac{\omega - \frac{1}{\omega_n}}{1 - \frac{\omega}{\omega_n}}\right)\right] = \frac{P_N(\omega)}{F_{Nz}(\omega)} \tag{4.12}$$

where ω_n, N and N_z are the locations of RZs, number of TZs and number of finite RZs, respectively. P_N and F_{Nz} are polynomials of degree N and N_z which present the numerators of S_{21} and S_{11}, respectively. The filtering function can be calculated by a recursive formula given in [23], in rational function form. Once the filtering function is known, the denominators of S_{11} and S_{21}, $E(s)$, can be determined by (4.13), that is the unitary property of the scattering matrix.

$$|E(s)|^2 = |F(s)|^2 + |P(s)|^2 \tag{4.13}$$

Table 4.2 shows the coefficients of the reflection and transmission functions' numerators and denominators. The filter's TZs are located at normalized angular frequencies ω_1= 0.7639, ω_2=0.3046 and ω_3=0.9268.

Table 4.2: Ridged bandstop filter: coefficients of $E(s)$, $F(s)$ and $P(s)$ polynomials

S^i i	Coefficients of S_{11} and S_{21} Denominator polynomials $E(s)$ (e_i)	Coefficients of S_{11} Numerator Polynomial $F(s)$ (f_i)	Coefficients of S_{21} Numerator Polynomials $P(s)$ (p_i)
0	-7.1963 - j15.6548	70.7875 + j0.0000	0.7988 + j0.0000
1	9.3949 - j17.0142	0.0000 + j64.2476	0.0000 + j2.4387
2	6.8403 - j2.3593	-18.7960 + j0.0000	1.7316 + j0.0000
3	1.0000 + j0.0000	0.0000 - j1.7777	0.0000 + j3.7042

Given the locations of both RZs and TZs, the method presented in [9] is used to extract the parameters of the circuit shown in Fig. 4.17. This method uses the reflection coefficient and input admittance to extract the filter parameters shown in Fig. 4.17. The reflection coefficient can be rewritten in the form

$$S_{11}(s) = e^{j\phi_{11}}\kappa\frac{\bigcap_{i=1}^{i=Nz}(s - s_{zi})}{\bigcap_{i=1}^{i=N}(s - s_{pi})} = e^{j\phi_{11}}\frac{M(s)}{D(s)} \tag{4.14}$$

where S_{zi} are the locations of RZs at finite frequencies and S_{pi} are S_{11}'s poles. The phase term $e^{j\phi_{11}}$ does not affect the amplitude response of the reflection coefficient,

but it is very important in the synthesis procedure. It is shown in [9] that $e^{j\phi_{11}}$ and the scaling constant κ are calculated by

$$e^{j\phi_{11}} = \frac{D(s=j\omega_1)}{M(s=j\omega_1)} \qquad \kappa^2 = \frac{\bigcap_{i=1}^{i=N} |j - S_{pi}|^2}{(1+\epsilon^2)\bigcap_{i=1}^{i=Nzi}(1+\omega_{zi}^2)} \tag{4.15}$$

If the resistance of the source is set to unity, the input admittance of the network is

$$y_{in}(s) = \frac{1 - S_{11}(s)}{1 + S_{11}(s)} = \frac{D(s) - e^{j\phi_{11}}M(s)}{D(s) + e^{j\phi_{11}}M(s)} \tag{4.16}$$

On the other hand, the input admittance of the circuit in Fig. 4.17 is given by

$$y_{in}(s) = \frac{J_1^2}{(\frac{J_2^2}{s-j\omega_1}) + y_{in}^{(2)}(s)} \tag{4.17}$$

By equating (4.16) and (4.17) and applying the cyclic procedure in [9], the parameters of the circuit shown in Fig. 4.17 are extracted. Note that to start the parameter extraction procedure, we have to set the value of J_1. Different values can be chosen depending on other inverter values between the input and the output. For this filter, we choose J_1= 1. Then the final extracted parameters of the filter are: J_1=1, J_2=1.8968, J_3=2.5620, J_4=1.3938, J_5=0.7421, ϕ_1=49.0491°, ϕ_2=36.7040° and ϕ_3=75.6224° (c.f. Fig. 4.17).

4.3.3 Bandstop SIW Filter Realization Using Partial-Height Plated Via Holes as Resonators

In this section, we realize the extracted equivalent circuit, obtained in Section 4.3.2, in ridged SIW technology. The partial-height plated via holes in a thick substrate are used as resonating elements.

The initial values of the filter dimensions are obtained by relating the equivalent circuit elements to their appropriate corresponding physical parameters in the filter and force their responses to match [91]. The resonant frequencies of the resonators are mainly determined by the resonators' heights. Therefore, the height of each resonator is chosen properly to bring its corresponding TZs to the desired resonant frequency. Then the coupling value J is appropriately realized by adjusting the resonator's offset from the center of the main waveguide. Fig. 4.18a shows an off-centered partial-height

via in rectangular waveguide, and Fig. 4.18b shows its equivalent T-network. The

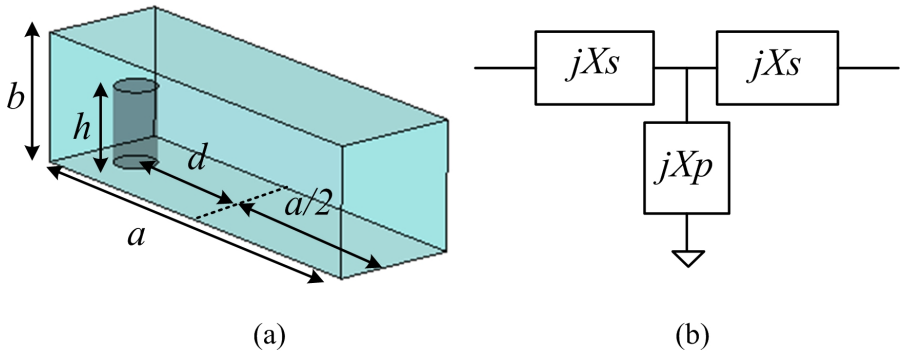

Figure 4.18: Off-centered partial-height via as resonant element; a) partial-height circular via in a waveguide, $a = 10.30$ mm, $b = 3.048$ mm, $h = 2.64$ mm, b) its equivalent T-network.

diameter of the via is 1 mm and its offset from the center of the waveguide is d. The waveguide is filled with RT/Duroid 6002 with dielectric constant of 2.94 and loss tangent of 0.0012. The scattering parameters of the structure shown in Fig. 4.18a, for different values of d, are presented in Fig. 4.19a.

As shown in Fig. 4.19a, the resonant frequency of the resonator is slightly changed by varying its offset from the center of the waveguide. The elements of the T-network, shown in Fig. 4.18b, are extracted using scattering parameters of the resonator in Fig. 4.18a by

$$\begin{aligned} \frac{jX_p}{Z_0} &= \frac{2S_{11}}{(1-S_{11})(1-S_{22})-S_{12}S_{21}} \\ \frac{jX_s}{Z_0} &= \frac{-2S_{11}+S_{12}S_{21}+(1+S_{11})(1-S_{22})}{(1-S_{11})(1-S_{22})-S_{12}S_{21}} \end{aligned} \tag{4.18}$$

As shown in Fig. 4.19b, the series element X_S is inductive in the vicinity of the resonant frequency and almost constant. However, the shunt element X_P is capacitive below the resonant frequency and inductive above it, for all different values of d.

The offset of a resonator, responsible for the normalized transmission zero ω_1, from the center of the waveguide is obtained by forcing the shunt element of the equivalent T-network to be

$$\frac{X_p}{Z_0} = \frac{\omega-\omega_1}{J_1^2} \qquad \omega = \frac{f_0}{BW}\left(\frac{f}{f_0}-\frac{f_0}{f}\right) \tag{4.19}$$

$$J_1^2 = \frac{1}{\left(\frac{\partial X_p(\omega)}{\partial \omega}\right)} \qquad at\ \ \omega=\omega_1 \tag{4.20}$$

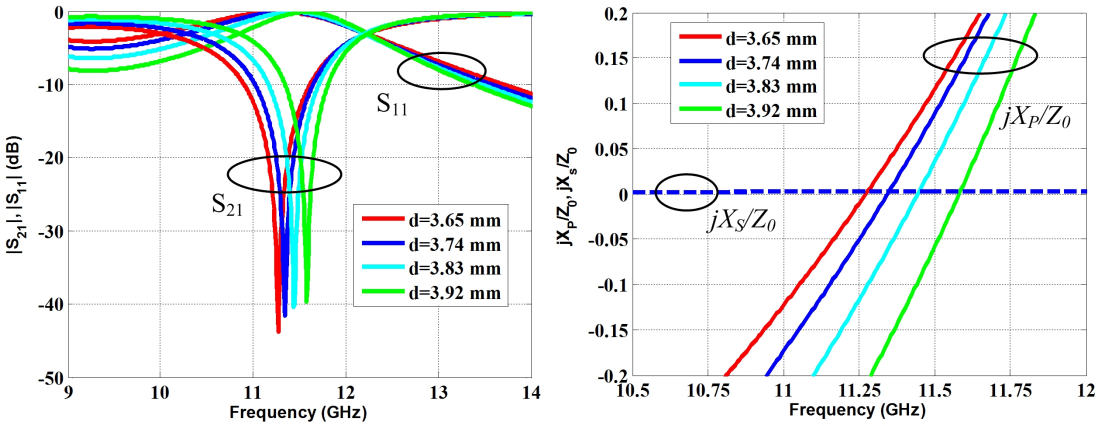

Figure 4.19: a) Scattering parameters of the circuit shown in Fig. 4.18a; b) variation of the equivalent circuit parameters shown in Fig. 4.18b with frequency.

The phase shifters between resonators are also realized by SIW sections with appropriate lengths. After estimating the initial values of the resonators heights and their offsets from the main waveguide's center, we employ μWave Wizard to simulate and optimize the filter in ridged SIW technology. To facilitate low-reflection feeds in the modeling and optimization steps, all-dielectric waveguide ports of equivalent width are used.

CST is used for verification, and the filter's three-dimensional (3D), top and bottom views in CST are shown in Figs. 4.20. Fig. 4.21 also shows a side view of the locations of the partial-height resonators in the substrate. The substrate selected for this application is RT/Duroid 6002 with dielectric constant of 2.94, loss tangent of 0.0012, conductor thickness of 17 μm and conductivity of 5.8×10^7 S/m. The substrate thickness is 3.048 mm because of the incorporation of partial-height vias. The diameter of all vias is 1 mm, their centre-to-centre longitudinal spacing is 1.4 mm and their lateral spacing is 11.9 mm. This leads to an equivalent waveguide width of 10.3 mm and a cutoff frequency of 8.48 GHz at the SIW ports.

Although we first chose J_1=1, during the optimization process we have to decrease the input coupling, shown in Fig. 4.20b, to improve the passband return loss. As depicted in Fig. 4.22, decreasing the input coupling does not significantly change the stopband characteristics, but gives an extra degree of freedom to properly optimize the RZs locations in the passband.

The final responses of the filter with those of the equivalent circuit, shown in Fig.

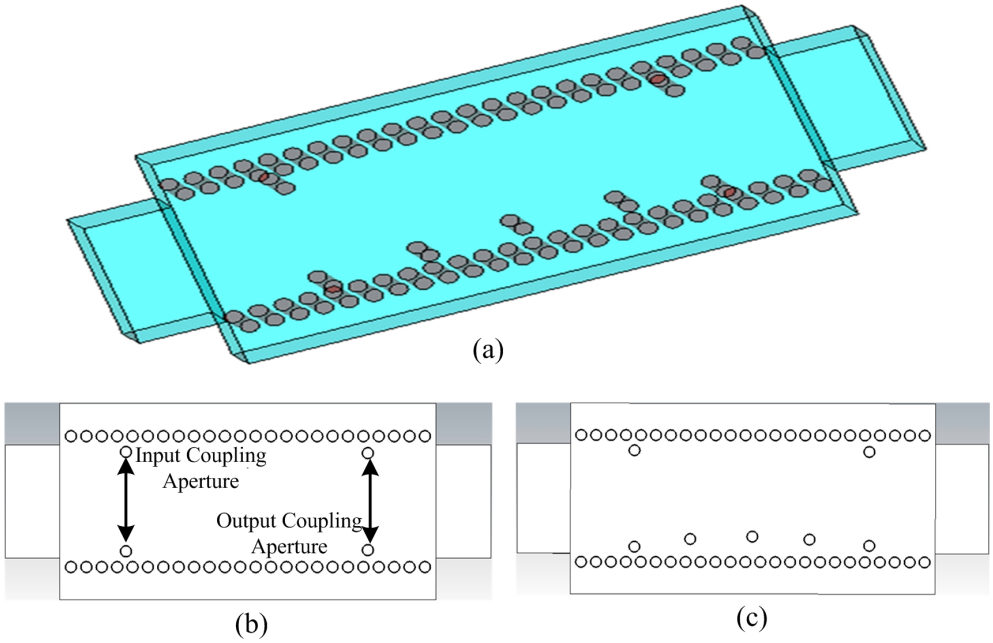

Figure 4.20: Third-order ridged SIW bandstop filter with waveguide ports; a) 3D view in CST, b) top view indicating the coupling apertures, c) bottom view.

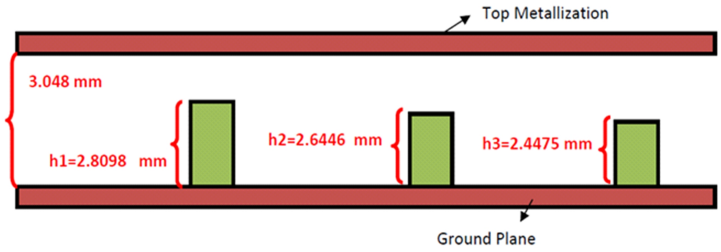

Figure 4.21: Side view of the positions of the partial-height posts in a 3.048 mm thick substrate.

4.17, are presented in Fig. 4.23 for comparison. The discrepancy in the passband between simulated and synthesized insertion losses is attributed to the fact that the phase shifters are generally frequency dependent whereas, in the equivalent circuit synthesis, they are assumed constant. The frequency dependence of the phase shifters is completely considered by the full-wave frequency solver of the CST. Moreover, the equivalent circuit is a narrow-band model focusing on the stopband. Therefore, the model becomes less accurate for frequencies away from the stopband. Note that the RZs of the equivalent circuit are well produced by the simulated filter.

A wider frequency response of the filter is shown in Fig. 4.24, using both μWave Wizard and CST. Good agreement between the two simulations confirms the integrity

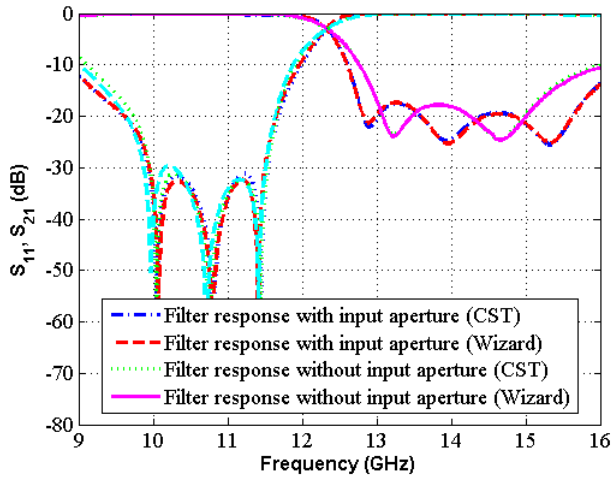

Figure 4.22: Effect of the input coupling on the final filter response.

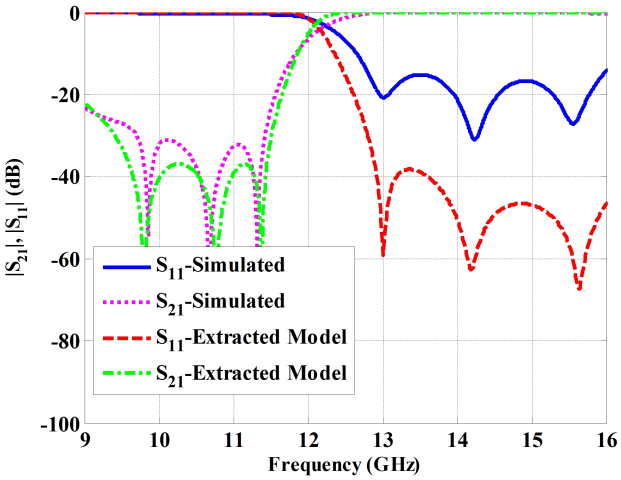

Figure 4.23: Comparison between the simulated and equivalent circuit scattering parameters of the third-order ridged SIW filter.

of the design process. As presented in Fig. 4.24, the cutoff frequency of the filter is 8.48 GHz which coincides with the cutoff frequency of the SIW ports. The designed filter creates an equi-ripple bandstop immediately after its cutoff frequency, followed by a passband extended up to the cutoff frequency of the next higher order mode at 16.96 GHz.

Note that although the designed filter has high-pass application, the design process is carried out for the stopband part of the filter response using bandstop resonators. Therefore, this filter can be categorised as bandstop filter with high-pass application.

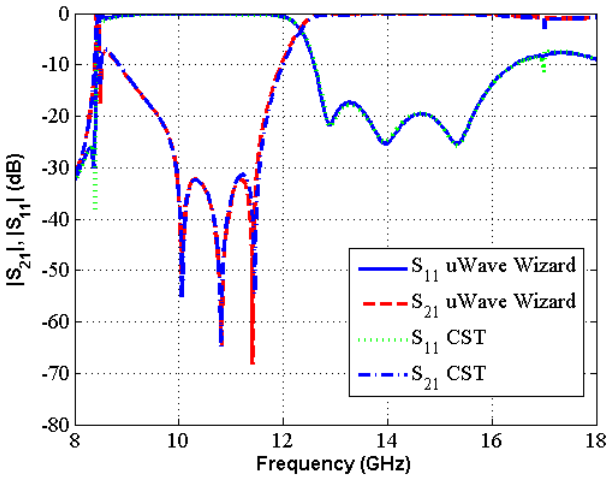

Figure 4.24: Wideband simulated scattering parameters of the third-order ridged SIW filter with waveguide ports using CST and μWave Wizard.

For comparison, the field distributions in the conventional SIW, the SIW with input and output apertures and the designed filter are presented in Fig. 4.25. At passband frequencies (Fig. 4.25c), the field is hardly disturbed by the partial-height via resonators. In the stopband, however, the electric fields are concentrated between the free ends of the posts and top metallic plate (Fig. 4.25d), resulting in a wide stopband.

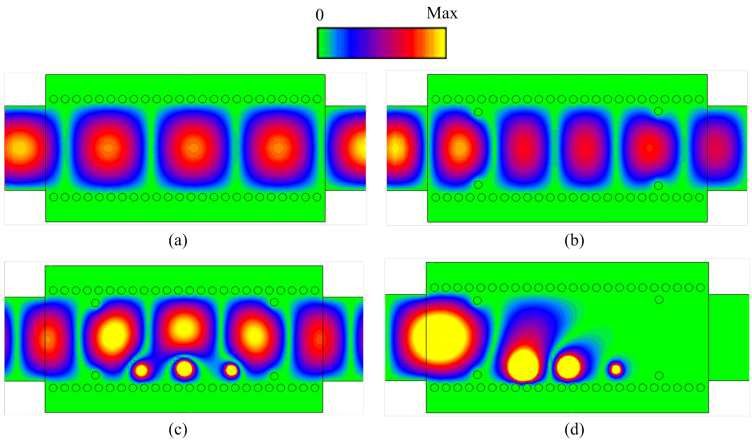

Figure 4.25: Electric field distributions for a) conventional SIW, b) conventional SIW with input and output apertures, c) designed filter at 14 GHz, d) designed filter at 10.70 GHz.

4.3.4 Tolerances Analysis of Partial-Height Resonators

Since in the designed filter, the resonators are partial-height posts, small changes in their heights can affect the filter response. Existing fabrication technologies are able to realize a partial-height via hole with ± 12 μm tolerances in its height. Fig. 4.26 shows the effects of changes, up to ± 12 μm, of each resonator height on the transmission and reflection coefficients of the filter. As depicted in Fig. 4.26, any tolerances in the heights of the resonators change the attenuation in the stopband and slightly the location of the TZs, but they have no significant effect on the location of the RZs or return loss in the passband.

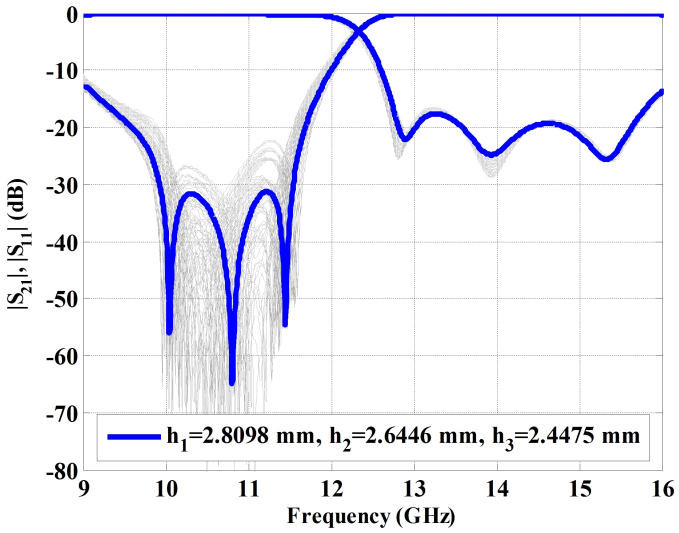

Figure 4.26: Effect of changes in resonators heights on the transmission and reflection coefficients of the filter.

4.3.5 Effects of SMA Coaxial Ports on Passband and Stopband Specifications

For access with measurement equipment, it is common practice to use microstrip ports. Therefore, the designed filter is also simulated in CST with microstrip ports. Conventional transitions to 50 Ω microstrip are tapered lines, starting with wider width at the SIW interface and ending in the width of the 50 Ω microstrip line. For this filter, however, because of the high substrate thickness, we need to use a wider and uniform 50 Ω microstrip line, as shown in Fig. 4.27, that is different from conventional transitions.

Figure 4.27: Top view of the designed SIW filter with microstrip ports.

On the other hand, the high substrate thickness prevents us from using a standard test fixture to measure the performance of the filter. Therefore, we have to use SMA launchers to connect the vector network analyzer to the filter. Soldering coaxial SMA connectors to the wide microstrip ports may affect the responses of the filter and the measurements as the SMA launchers will have to be connected to calibration standards as well. To reduce the influence of these connectors, the pins of the SMAs should be located exactly at the centers of the wide microstrip transitions. To investigate this effect, we simulate the filter with coaxial ports. The dimensions of the SMA connectors are chosen based on industry standards.

Fig. 4.28 shows the filter responses for different ports. We observe that connecting coaxial ports to the wide microstrip transitions reduces the attenuation in the stopband and return loss in the passband. However, both values remain better than 10 dB which is acceptable for many applications.

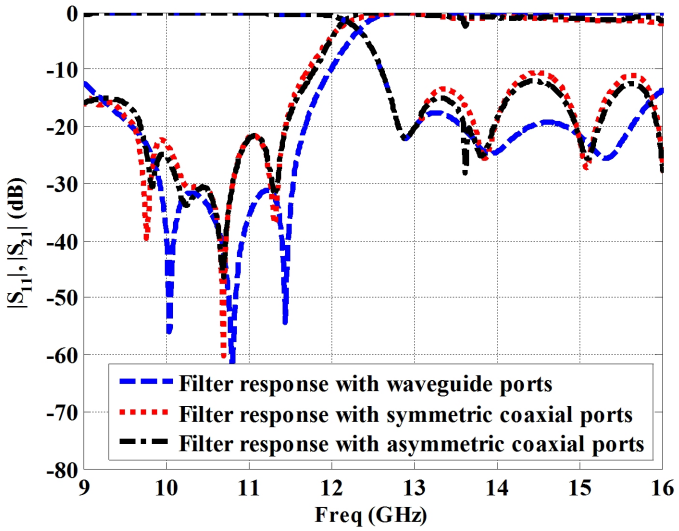

Figure 4.28: Investigation of the effect of coaxial ports on the filter response.

4.3.6 Fabrication and Experimental Results

The designed filter is prototyped and measured. Fig. 4.29a and Fig. 4.29b show the photographs of the bottom and top views of the fabricated filter. Fig. 4.29c shows the comparison between simulated and measured results. A Through-Reflect-Line calibration kit is used to deembed the effects of the microstrip transitions and soldered coaxial connectors. The measured results are in good agreement with simulations. The locations of the simulated TZs and RZs are well confirmed by measurements. The stopband attenuation is better than 20 dB, and the passband return loss is better than 12 dB up to 15.8 GHz. The maximum measured passband insertion loss is 1.8 dB at 12.68 GHz and remains below 1.5 dB between 12.68 and 15.9 GHz. Some discrepancies in the corresponding stopband attenuation and passband return loss levels are observed. They can be attributed to the following factors. First, since in this filter, the resonators are partial-height posts in a thick, but still relatively low-profile substrate, small tolerances in the post heights can change the attenuation in the stopband as demonstrated in Section 4.3.4. Second, the tolerances of the dielectric constant, 2.94 ± 0.04, can also affect the return loss and attenuation levels, but mainly result in a small frequency shift. Third, the effects of different (manual) soldering of coax connectors to the microstrip ports of both the filter circuit and calibration standards influence the calibration procedure and therefore the measurements. Nevertheless, the good agreement between simulation and experiment in Fig. 4.29c validates the design approach.

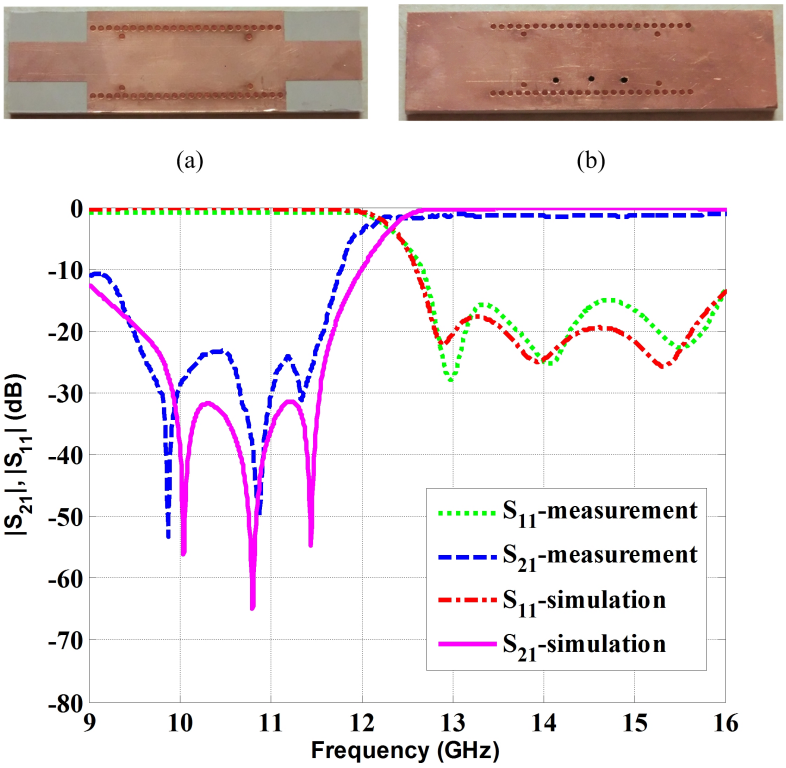

Figure 4.29: Prototyped third-order ridged SIW bandstop filter; a) top view, b) bottom view, c) simulated and measured transmission and reflection coefficients of the designed filter.

Chapter 5

Novel Tunable Bandstop Microwave Filters

A great effort has been recently conducted on implementation of fully reconfigurable and multipurpose RF and microwave systems in order to develop universal high-frequency transceiver modules. In addition, post-fabrication tuning is necessary in most cases to fine-tune the operating frequency of microwave devices to the desired one. Otherwise, these devices would have to be refabricated. Unlike multi-band/wideband microwave structures, tunable devices have better isolation and are more immune to the cross talks coming from neighbor channels. On the other hand, serving several frequency bands should not decrease the quality factor and selectivity of the device which is not true for multi-band structures.

Tunable microwave filters are one of the most critical and challenging components in systems that perform adaptive frequency band selections [92]. It is desirable for tunable filters to show tuning in terms of center frequencies, bandwidths, and even group delays, so that different signals with different spectrum specifications can be processed by them. In the last two decades, tunable RF/microwave filters have been widely proposed in different technologies depending on intended applications such as satellite communications, mobile communications, defense/military systems, etc; among them are waveguide, coaxial cavity, microstrip, and microwave monolithic integrated circuits (MMICs) [93, 94]. Planar microwave filters are more attractive, mainly because of their higher simplicity of experimental circuit verifications. Basically, tuning procedures are carried out electronically, magnetically, and mechanically depending on the tuning range, quality factor, linearity, fabrication complexity, and

integration potential.

Most of the conducted researches on tunable filters are focused on designing filters with tunable center frequency. This is mostly because of the simplicity of the principle idea that is changing the natural frequency of the filter's resonators by a variable reactance such as pin, Schottky, or varactor diodes, ferroelectric barium-strontium-titanate (BST) capacitors, or even microelectromechanical systems (MEMSs) when power-handling capability, linearity behavior, and preservation of unloaded quality factor across the entire frequency-tuning range are required [95–98]. In addition, the center frequency of microwave filters can be changed by varying the effective permittivity of the substrate employing piezoelectric principles, ferroelectric material, thin layers or multilayer liquid-crystal-polymer (LCP) structures. But the results show a moderate success up to now [99, 100].

Filters with tunable bandwidth are more sophisticated because they require adjustable couplings between resonators as well as tunable output/input couplings. Some bandwidth-tunable passband filters have been reported in [101–103].

The majority of the published papers on tunable filters are on microstrip tunable filters. Microstrip filters have low quality factors, and the achievable quality factor degrades more by integrating tuning elements with filters. Theses filters cannot be used in practical and stringent applications like satellites or base stations. Recent works on silicon micro-machined filters and tunable substrate integrated waveguide (SIW) [104–107] have better Q, but their quality factor is not comparable with a few papers reported on high-Q 3D coaxial, waveguide and dielectric resonators tunable filters [16].

Two important factors are always considered by researchers while designing tunable filters. One of them is the tunable range in terms of bandwidth, center frequency, and filtering functions such as switchable bandpass/bandstop responses or controllable single/multiband operations. The second one is the effect of tuning elements on filters specifications such as insertion loss, selectivity, power handling capability, and linearity deterioration over the tunable range.

In this chapter, we introduce two novel tunable bandstop filters using varactor diodes. In addition, the main specifications of varactor diodes and their equivalent circuits at high frequencies are discussed. The designed filters are fabricated and measured to verify the design methods.

5.1 Varactor Diode Modeling

Varactor diodes, as one of the many microwave semiconductor devices, are widely used for tuning purposes. Tuning varactors are voltage-controlled capacitors designed to provide electronic tuning of oscillators and filters. Varactor diodes are usually made of two semiconductors; one of them is silicon and another one is gallium arsenide. Silicon diodes typically offer lower manufacturing costs, while gallium arsenide diodes have higher quality factors and may be used at higher microwave frequencies.

An equivalent-circuit model of the SMV1232 varactor diode from its data sheet is presented in Fig. 5.1. Note that other varactor diodes might have different equivalent circuits. Where C_j and R_s are junction capacitor and series resistant of the diode,

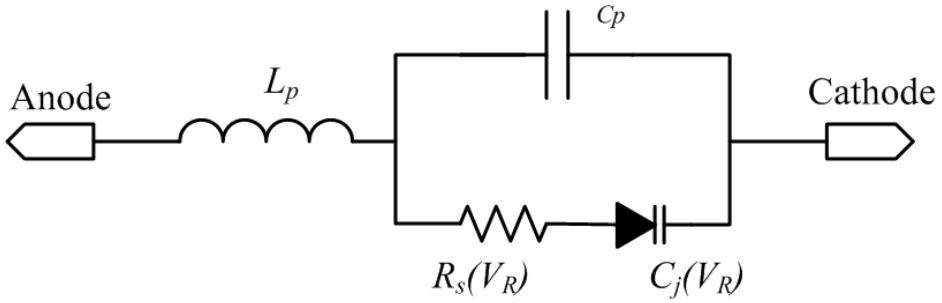

Figure 5.1: Equivalent circuit of a varactor diode.

respectively. The diode's packaging effects are taken into account and are presented by shunt capacitor C_p and series inductor L_p. The junction capacitor, C_j, varies with the applied reverse voltage across the diode, V_R, by

$$C_j(V_R) = \frac{C_{JO}}{(1 + \frac{V_R}{V_J})^M} \tag{5.1}$$

Where C_{JO}, V_J, and M are zero-bias junction capacitance, junction potential, and grading coefficient, respectively [108]. The unloaded quality factor of a varactor at frequency f is calculated by

$$Q_{Var} = \frac{1}{2\pi f C_j(V_R) R_s(V_R)} \tag{5.2}$$

As (5.2) indicates, the main disadvantage of tunable filters using varactor diodes, compared to regular filters, is their lower quality factor due to the series resistance of the varactor diode varying with reversed biasing voltage.

The spice model parameters of the SMV1232 varactor diode, which is used in the next sections as tuning element, are listed in Table 5.1. The parameters are general and are used for different types of varactor diodes. To obtained the junction

Table 5.1: Spice model parameters for the SMV1232 varactor diode

Parameter	Description	Unit	Typical Value
I_s	Saturation current. With N determines the DC characteristics of the diode.	A	1e-14
R_s	Series resistance.	Ω	1.5
N	Emission coefficient. With I_s determines the DC characteristics of the Diode.	-	1
T_T	Transit time.	sec	0
C_{JO}	Zero-bias junction capacitance. With M and V_j defines nonlinear junction capacitance of the diode.	PF	3.43
V_j	Junction potential. With C_{JO} and M defines nonlinear junction capacitance of the diode.	V	8.36
M	Grading coefficient. With C_{JO} and V_j defines nonlinear junction capacitance of the diode.	-	4.69
E_G	Energy gap. With X_{TI} helps define the dependence of I_s on temperature.	EV	1.11
X_{TI}	Saturation current temperature exponent. With E_G helps define the dependence of I_s on temperature.	-	3
K_F	Flicker noise coefficient.	-	0
A_F	Flicker noise exponent.	-	1
F_C	Forward-bias depletion capacitance coefficient.	-	0.5
B_V	Reverse Breakdown voltage.	V	infinity
I_{BV}	Current at reverse breakdown voltage.	A	1e-3
I_{SR}	Recombination current parameter.	A	0
N_R	Emmision coefficient for I_{SR} parameter.	-	2
I_{KF}	High injection knee current.	A	infinity
N_{BV}	Reverse breakdown ideality factor.	-	1
I_{BVL}	Low-level reverse breakdown knee current.	A	0
N_{BVL}	Low-level reverse breakdown ideality factor.	-	1
T_{NOM}	Nominal ambient temperature at which these model parameters are derived	c	27
F_{FE}	Flicker noise frequency exponent.	-	1

capacitance of a varactor diode, using its spice model, the circuit shown in Fig. 5.2 is used.

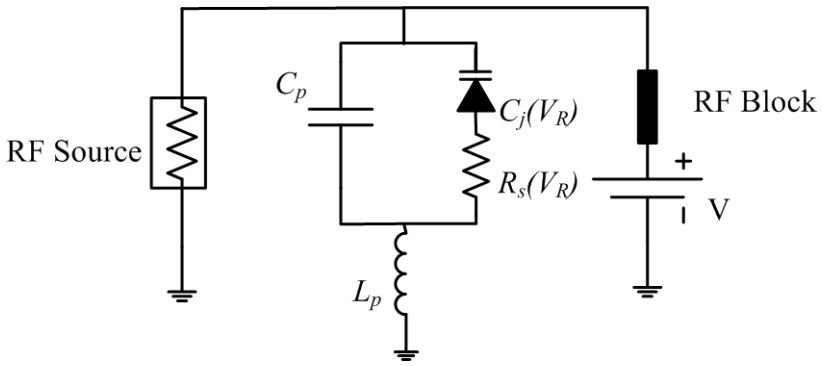

Figure 5.2: Circuit for varactor diode capacitance calculation.

The total capacitance of the varactor diode is obtained by

$$C = \frac{1}{-Im(Z_{11})2\pi f} \tag{5.3}$$

where Z_{11} is the input impedance seen by the RF source at frequency f. The junction capacitance versus applied reverse voltage is shown for the SMV1232 in Fig. 5.3. The

total capacitance of the diode decreases by increasing the reverse applied voltage. The tuning ratio of this varactor diode is $\frac{C_{max}}{C_{min}} = \frac{4.1}{0.7} = 5.85$.

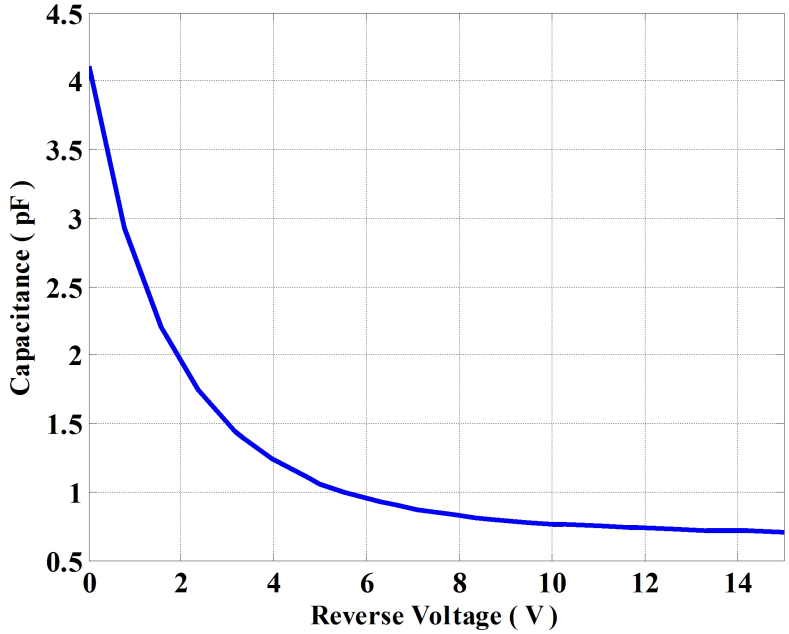

Figure 5.3: Capacitance vs. reverse biasing voltage for the SMV1232 varactor diode.

5.2 Tunable Ridged SIW Bandstop Resonator

High quality factor resonators are typical part of many high performance passive and active circuits. As a result, SIW structures are good candidates for developing planar microwave devices due to ease of fabrication, high-power handling, high linearity, and integrability of SIW filters with other sections of the microwave system. Tunable SIW filters, due to their resonant nature, have a narrower tunable range. In filters consisting of several resonators, the coupling coefficients between resonators and the external quality factors vary with frequency. Therefore, designing a tunable filter is more difficult than designing a tunable resonator. Tunable SIW bandpass microwave filters are investigated in several papers, and a recent review of all these techniques is presented in [109]. But only a handful bandstop SIW filters are reported in the literature and all of them use evanescent mode SIW cavities loaded with a metallic post at their centers, such as those reported in [110–113]. In this section, we outline the design process of a new tunable ridged SIW bandstop resonator.

5.2.1 Resonator Design

As presented in Chapter 4, a partial-height off-centered post inside a waveguide is a bandstop resonator whose resonant frequency is determined by the length of the post. This resonator can be modified properly to create a tunable bandstop resonator by employing varactor diodes. In the modified structure, as shown in Fig. 5.4, the length of the off-centered metallic post is equal to the SIW height. The post connects the bottom wall of the SIW to a patch which is isolated from the SIW's top wall. As presented in Fig. 5.4, the metallic post represents an inductor connected in parallel to a capacitor created by the spacing between the SIW's top wall and the isolated patch. The size of the larger patch and the spacing between that and the SIW top metalization is optimized to obtain the best in-band and out-of-band responses. The size of the smaller patch is chosen as small as possible, 2×2 mm^2, for soldering purposes. The spacing between the larger and the smaller patch is 0.15 mm which is the smallest possible value by current manufacturing facilities. A tunable bandstop resonator is achievable if this capacitor is replaced by a varactor diode as illustrated in Fig. 5.4. The resistances shown in Fig. 5.4 represent conductor, dielectric and radiation losses. Simulation results of the bandstop resonator shown in Fig. 5.4 (without varactor diode) is presented in Fig. 5.5a. The substrate height is 1.524 mm and it is filled with RT/Duroid 6002 with dielectric constant of 2.94 and loss tangent of 0.0012. The via diameters are 1 mm. The input impedance of the resonator, extracted from simulated scattering parameters and outlined in Fig. 5.5b, has a maximum at resonant frequency which indicates that the resonator represents a parallel RLC circuit. At resonant frequency, the input impedance of a parallel RLC circuit is purely real and equal to $|Z_{in}| = R$. The total resistance R of the designed resonator is calculated as 634.9 Ω. The loaded quality factor of the resonator is obtained as

$$Q_L = \frac{f_0}{\Delta f_{3dB}} \tag{5.4}$$

where f_0 and Δf_{3dB} are center frequency and 3 dB bandwidth of the resonator. The unloaded quality factor of the resonator, Q_U is obtained from Q_L by [114]

$$Q_U = \frac{Q_L}{1 - 10^{\frac{-IL}{20}}} \tag{5.5}$$

Here IL is the attenuation at resonant frequency. The Q_U for this resonator is calculated as 55. To make a tunable bandstop resonator, a varactor diode is connected

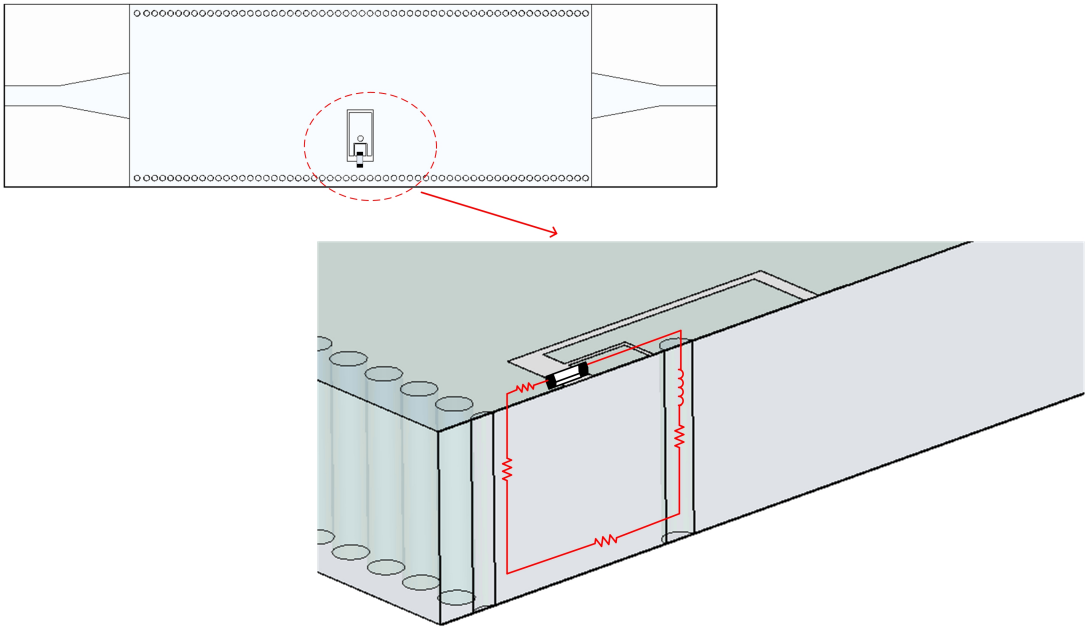

Figure 5.4: Tunable ridged SIW resonator.

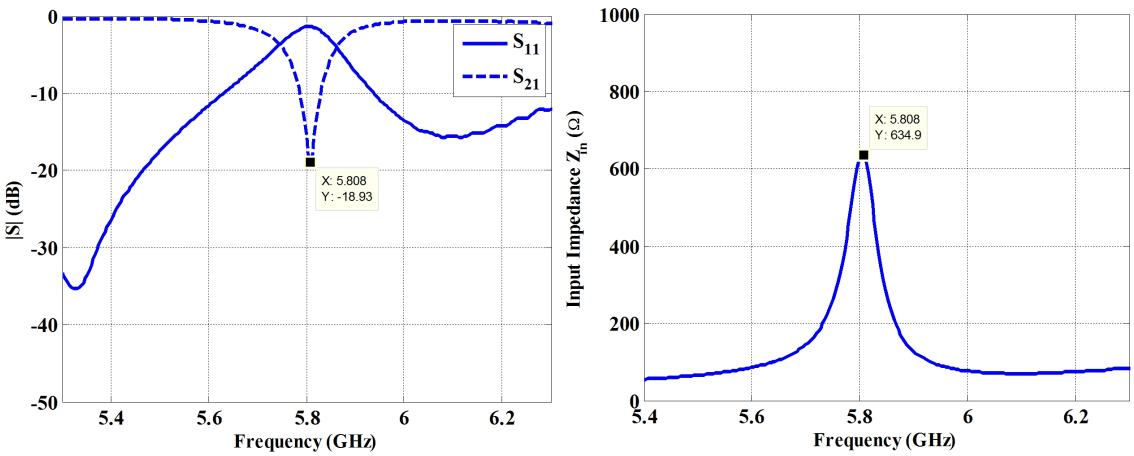

Figure 5.5: a) Scattering parameters of the bandstop ridge SIW resonator shown in Fig. 5.4; b) its input impedance.

between the top wall of the resonator and the isolated patch. For biasing purpose, a small patch is isolated from the larger patch on the top (c.f. Fig. 5.4). A 150 Ω resistor is used as RF blocking element. The SMV1232 varactor diode is employed for tuning procedure.

5.2.2 Simulated and Measured Results

The designed resonator is prototyped and measured. Fig. 5.6a shows the fabricated resonator with the biasing circuit and the varactor diode. The simulated and measured results are compared in Fig. 5.6b. For all simulations R_s is constant and equal

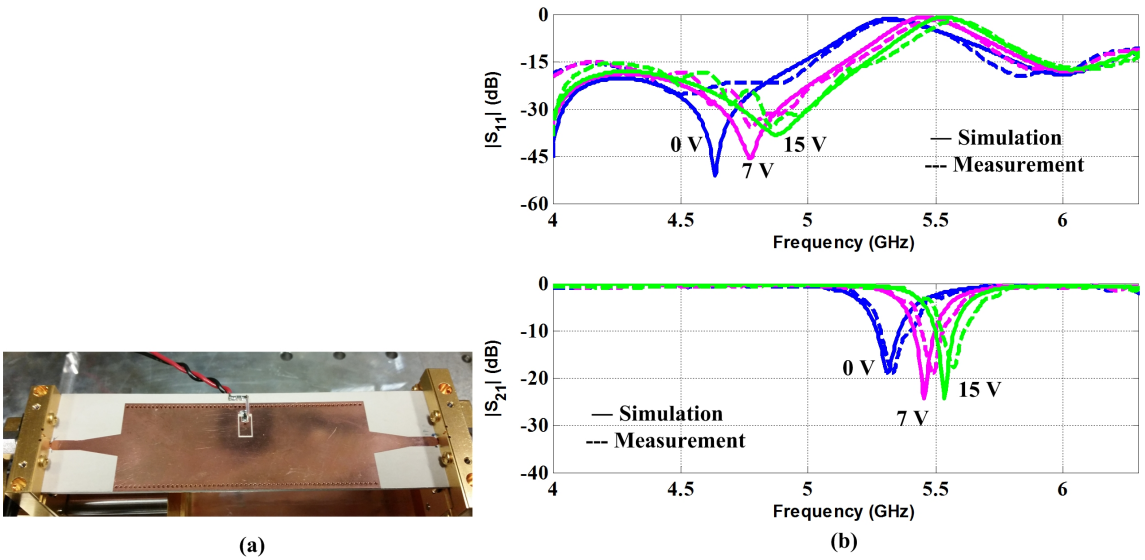

Figure 5.6: a) Prototyped tunable ridged SIW bandstop resonator; b) comparison between simulated and measured results.

to 1.5 Ω (Fig. 5.2). The simulated results show a tunable range of 1.05:1 which is in good agreement with that obtained from measurements, which is 1.04:1. An upward frequency shift is observed in the measured transmission zeros that is attributed to the manufacturing tolerances. The measured attenuation and return loss are better than 17.89 dB and 2.02 dB over the entire tunable range, respectively. The tuning range of the designed resonator is 4.1%. The number of ridged resonators can be increased. In this case, the couplings between resonators should be appropriately tuned as well.

5.3 Dual-Band Bandstop Filter with One Tunable Stopband

In this section, we combine two different bandstop resonating elements, open-ended CPW and ridged SIW resonators, to create a dual-bandstop SIW filter. One of the

resonators is loaded by varactor diodes to create a tunable stopband.

5.3.1 Open-Ended CPW Bandstop Resonator

The principals and applications of coplanar waveguides (CPWs) in microwave and millimeters integrated circuits (MMICs) has been widely investigated in the literature [115]. One of the interesting aspects of CPW components is that surface mount elements can be easily integrated due to their coplanar grounds. Therefore, CPW resonators are good candidates for tunable filter designs.

Several types of CPW resonators are analyzed in [116], including an open-ended CPW resonator. Fig. 5.7a shows an open-ended CPW resonator on a substrate integrated waveguide. The CPW resonator is loaded by two SMV1232 varactor diodes at both ends. The frequency responses of the resonator shown in Fig. 5.7a, for different applied reverse voltages over both varactor diodes, are presented in Fig. 5.8. The unloaded quality factor of the resonator varies between 24-35 over the tunable frequency range. The resonator has a tuning ratio of 1.17:1. The return loss and attenuation are obtained better that 2 dB and 15 dB, respectively, for different applied reverse biasing voltages. To make a dual-band bandstop filter, we use two

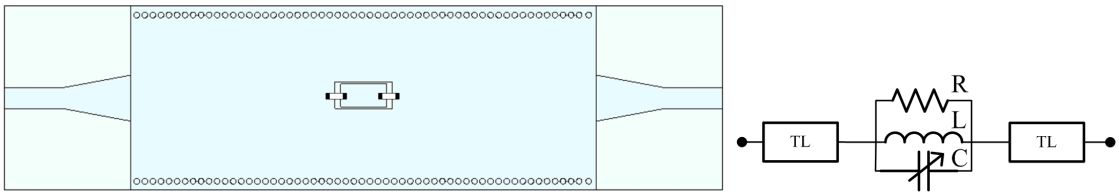

Figure 5.7: SIW transmission line loaded with tunable CPW resonator; b) equivalent circuit of the open-ended CPW resonator.

ridged SIW bandstop resonators, designed in Section 5.2, with a varactor diode-loaded open-ended CPW resonator between them, as outlined in Fig. 5.9. While the two ridged SIW resonators create the stopband at 5.6 GHz, the tunable CPW resonator provides a tunable stopband with tunable range of 3.5-4.1 GHz. The tuning range of this resonator is 15%. The designed filter is fabricated and measured. Fig 5.10a shows the fabricated component with biasing circuit. An inductor of 20 μH is used as RF block. As shown in Fig. 5.10b, good agreement is observed between simulated and measured results. The measured attenuation varies between 13.22 dB and 13.68 dB over the tunable range. The return loss is measured better than 4.9 dB for different

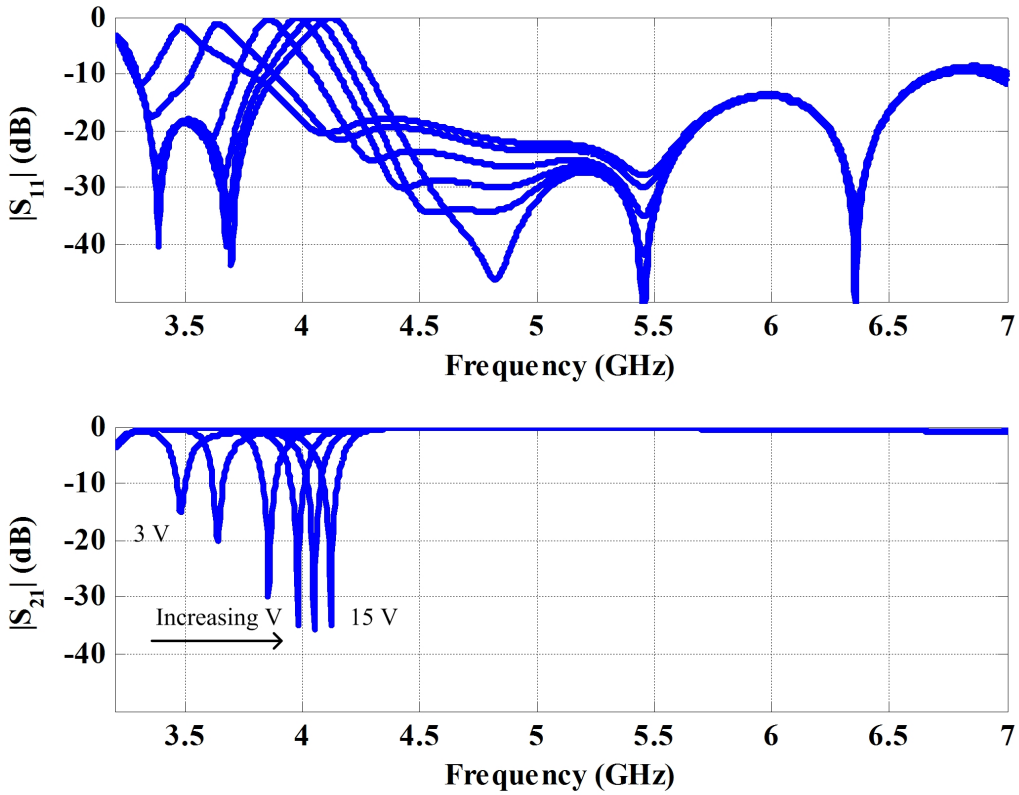

Figure 5.8: Frequency response of the tunable CPW resonator shown in Fig. 5.7a.

reversed applied voltages. The attenuation and the return loss are measured better than 14.7 dB and 1.7 dB, respectively, in the fixed stopband.

These results demonstrate that the tunable bandstop circuits, presented in this chapter, can be effectively used in reconfigurable SIW systems.

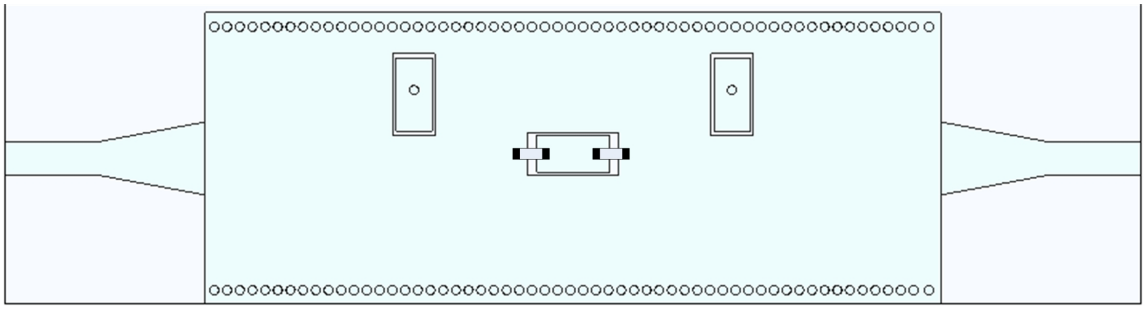

Figure 5.9: Dual-band bandstop filter created by combining two modified ridged SIW resonators and one open-ended CPW resonator.

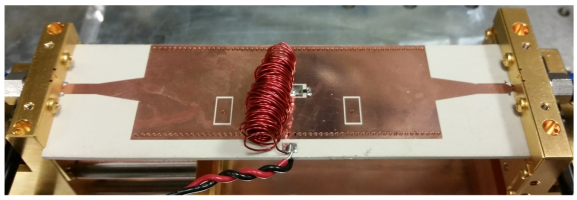

(a)

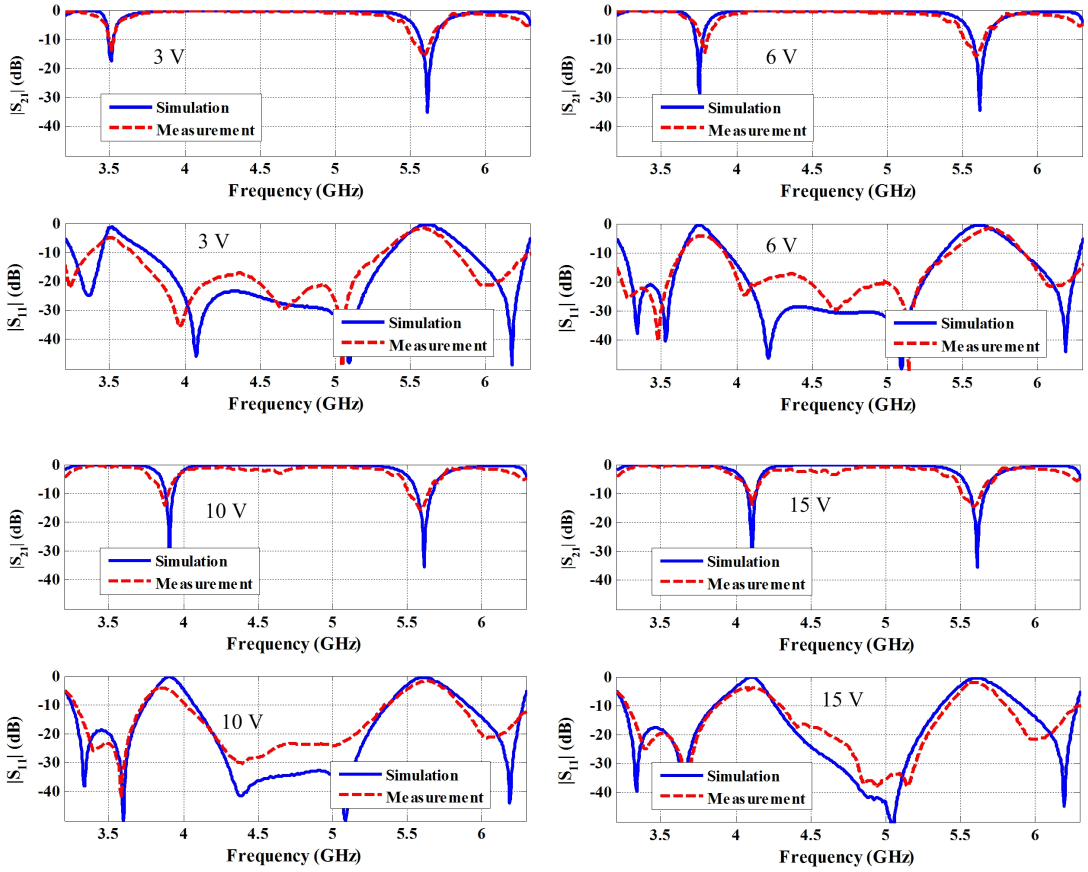

(b)

Figure 5.10: a) Prototyped dual-band bandstop filter with one tunable stopband; b) comparison between simulated and measured results.

Table 5.2 compares the tuning ranges of the designed resonators in this chapter with those of the evanescent-mode resonator filters reported in [110-113].

Table 5.2: Tuning range comparison

	Modified Ridged SIW	CPW	Ref. [110]	Ref. [111]	Ref. [112]	Ref. [113]
Tuning Range	4.1%	15%	12%	18%	18%	47%

The comparison shows that the designed tunable CPW resonator is comparable

with those reported in [110-112] while the design process and the circuit are much simpler. Though the tunable range of the modified ridged SIW resonator is limited, it has a good rejection in the stopband over the tuning range.

Chapter 6

Conclusions and Future Works

Microwave filters, as one the oldest and most critical parts of all microwave systems, have captivated researchers since 1930s. Emerging new technologies and materials helped develop different microwave resonators with different specifications and applications. Especially, advanced wireless communication and satellite systems demand new microwave filters with certain specifications regarding their seize, power handling capability, quality factor, and cost. The first objective of this thesis was to introduce novel bandstop filter design methods in planar technologies, especially in substrate integrated waveguide (SIW). These methods include both advanced coupling matrix and enhanced conventional filter design methods. In addition, today's wireless communication systems are developing to multi-standard systems that are able to cover different wireless systems by only one hardware setup. Therefore, the second objective of this thesis was developing bandstop microwave filters that can serve several frequency bands such as tunable or multi-band filters.

6.1 Advanced Coupling Matrix-Based Microwave Filters

The coupling matrix concept is one of the most powerful means in advanced filter designs. This concept can be employed to design single-band or multi-band, lossy or lossless, bandpass or bandstop filters without any limitation as far as the coupling mechanism between resonators are known. In addition, coupling matrices are applicable to filters involving nonresonating modes. We developed a hybrid analytic-optimization method to synthesize either single-band or multi-band band-

stop or bandpass filters with arbitrary located reflection or transmission zeros. Two novel multi-band bandstop filters were presented in Chapter 3 based on the coupling matrix concept. One of these filters is an in-line configuration and employs singlet modules and nonresonating modes while another is based on cross-coupled resonators.

Certain resonator configurations, such as cul-de-sac topologies, have interesting specifications to realize bandstop filters, but negative couplings are necessary to realize them. Analyzing and realizing multi-band bandstop filters involving negative couplings between some resonators can be investigated in the future. Moreover, synthesizing wideband frequency-dependent multi-band bandstop coupling matrices can be considered as another future work.

6.2 Enhanced Conventional Microwave Filters

A large amount of efforts is conducted to enhance the conventional filter design methods by introducing more accurate equivalent circuits as well as simpler and more robust design processes. The enhanced equivalent circuits are able to predict the filter responses more precisely by involving electromagnetic interaction between filter elements, thanks to advanced full-wave electromagnetic simulators. To address this subject, we presented three novel bandstop filters in Chapter 4 that were designed based on conventional bandstop stubs, microstrip L- and T-shaped microstip resonators, and the extracted-pole technique.

One of the interesting future works is using ridged SIW bandstop resonators to create multi-band bandstop filters by developing the equivalent circuit of the presented single-band ridged SIW bandstop filter.

6.3 Tunable SIW Bandstop Filters

Tunable filters are preferred to multi-band filter banks because they have less weight and smaller size. Moreover, serving several frequency bands by tunable filters, due to their better isolations, is preferred to employing multi-band filters. Due to ease of realization, center-frequency adjustable filters are interesting.

A ridged SIW bandstop resonator and a CPW resonator etched into a substrate integrated waveguide were introduced in Chapter 5. Tuning the center frequencies of these resonators is simply achieved electronically by employing varactor diodes. A dual-band bandstop filter was designed by combining two ridged SIW and one CPW

resonators. One of the filter's stopbands can be electronically tuned by loading the CPW resonator with varactor diodes.

Increasing the tunable range of these resonators can be considered as a future work. Moreover, the designed tunable ridged SIW resonator can be converted to a tunable ridged SIW filter by employing more resonators. In addition, in the dual-band bandstop filter, the ridged SIW resonators can be converted to tunable ones appropriately, to have two independent tunable stopbands.

Bibliography

[1] R. Levy, R. Snyder, and G. Matthaei, "Design of microwave filters," *IEEE Trans. Microw. Theory Tech.*, vol. 50, no. 3, pp. 783–793, 2002.

[2] R. Levy and S. Cohn, "A history of microwave filter research, design, and development," *IEEE Trans. Microw. Theory Tech.*, vol. 32, no. 9, pp. 1055–1067, 1984.

[3] S. B. Cohn, "Direct-coupled-resonator filters," *Proc. IRE*, pp. 187–195, 1957.

[4] P. Richards, "Resistor-transmission-line circuits," *Proc. IRE*, pp. 1945–1948, 1948.

[5] G. L. Matthaei, L. Young, and E. M. T. Jones, *Microwave Filters, Impedance Matching Networks and Coupling Structures*, Norwood, MA: Artech House, 1980.

[6] M. El Sabbagh, K. a. Zaki, H. W. Yao, and M. Yu, "Full-wave analysis of coupling between combline resonators and its application to combline filters with canonical configurations," *IEEE Trans. Microw. Theory Tech.*, vol. 49, no. 12, pp. 2384–2393, 2001.

[7] O. Monerris, P. Soto, S. Cogollos, V. Boria, J. Gil, C. Vicente, and B. Gimeno, "Accurate circuit synthesis of low-pass corrugated waveguide filters," *Proc. Eur. Microw. Conf.*, pp. 1237–1240, 2010.

[8] P. Soto, E. Tarín, V. E. Boria, C. Vicente, J. Gil, and B. Gimeno, "Accurate synthesis and design of wideband and inhomogeneous inductive waveguide filters," *IEEE Trans. Microw. Theory Tech.*, vol. 58, no. 8, pp. 2220–2230, 2010.

[9] S. Amari, U. Rosenberg, and R. Wu, "In-line pseudoelliptic band-reject filters with nonresonating nodes and/or phase shifts," *IEEE Trans. Microw. Theory Tech.*, vol. 54, no. 1, pp. 428–436, 2006.

[10] A. Morini, G. Venanzoni, T. Rozzi, and M. Villa, "A new prototype for the design of side-coupled coaxial filters with close correspondence to the physical structure," *IEEE Trans. Microw. Theory Tech.*, vol. 54, no. 3, pp. 1146–1152, 2006.

[11] A. E. Atia and A. E. Williams, "New type of waveguide bandpass filters for satellite transponders," *COMSAT Tech. Rev.*, vol. 1, no. 1, pp. 21–43, 1971.

[12] R. J. Cameron, "Advanced filter synthesis," *IEEE Microw. Mag.*, vol. 12, no. 6, pp. 42–61, 2011.

[13] R. V. Snyder, L. Fellow, A. Mortazawi, I. Hunter, S. Bastioli, G. Macchiarella, and K. Wu, "Present and future trends in filters and multiplexers," *IEEE Trans. Microw. Theory Tech.*, vol. 63, no. 10, pp. 3324–3360, 2015.

[14] S. F. R. Chang, W. L. Chen, S. C. Chang, C. K. Tu, C. L. Wei, C. H. Chien, C. H. Tsai, J. Chen, and A. Chen, "A dual-band RF transceiver for multistandard WLAN applications," *IEEE Trans. Microw. Theory Tech.*, vol. 53, no. 3 II, pp. 1048–1055, 2005.

[15] Z. Zakaria, N. Omar, A. R. Othman, M. S. Jawad, A. Salleh, and S. W. Yik, "Recent trends on dual- and triple-Band microwave filters for wireless communications," *Aust. J. Basic Appl. Sci.*, vol. 7, no. 10, pp. 235–243, 2013.

[16] R. R. Mansour, F. Huang, S. Fouladi, W. D. Yan, and M. Nasr, "High-Q tunable filters," *IEEE Microw. Mag.*, vol. 15, no. 5, pp. 70–82, 2014.

[17] J. S. Hong and M. J. Lancaster, *Microstrip Filters for RF / Microwave Applications*. New York: John Wiley and Sons, 2001.

[18] A. Antoniou and W. S. Lu, *Practical Optimization Algorithms and Engineering Applications*. New York: Springer, 2007.

[19] S. Amari, "Synthesis of cross-coupled resonator filters using an analytical gradient-based optimization technique," *IEEE Trans. Microw. Theory Tech.*, vol. 48, no. 9, pp. 1559–1564, 2000.

[20] R. J. Cameron, "Advanced coupling matrix synthesis techniques for microwave filters," *IEEE Trans. Microw. Theory Tech.*, vol. 51, no. 1, pp. 1–10, 2003.

[21] ——, "General coupling matrix synthesis methods for Chebyshev filtering functions," *IEEE Trans. Microw. Theory Tech.*, vol. 47, no. 4, pp. 433–442, 1999.

[22] A. Lamecki, P. Kozakowski, and M. Mrozowski, "Fast synthesis of coupled-resonator filters," *IEEE Microw. Compon. Lett.*, vol. 14, no. 4, pp. 174–176, 2004.

[23] S. Amari and U. Rosenberg, "Direct synthesis of a new class of bandstop filters," *IEEE Trans. Microw. Theory Tech.*, vol. 52, no. 2, pp. 607–616, 2004.

[24] R. J. Cameron, M. Yu, and Y. Wang, "Direct-coupled microwave filters with single and dual stopbands," *IEEE Trans. Microw. Theory Tech.*, vol. 53, no. 11, pp. 3288–3298, 2005.

[25] S. Awasthi, A. Biswas, and M. J. Akhtar, "Direct coupled quad-band band-stop filter synthesis using frequency transformation," *Proc. Asia-Pacific Microw. Conf.*, pp. 893–895, 2013.

[26] Y. Zhang, K. a. Zaki, J. a. Ruiz-Cruz, and A. E. Atia, "Analytical synthesis of generalized multi-band microwave filters," *IEEE MTT-S Int. Microw. Symp. Dig.*, pp. 1273–1276, 2007.

[27] D. Deslandes and F. Boone, "Iterative design techniques for all-pole dual-bandpass filters," *IEEE Microw. Compon. Lett.*, vol. 17, no. 11, pp. 775–777, 2007.

[28] Y. T. Kuo, J. C. Lu, C. K. Liao, and C. Y. Chang, "New multiband coupling matrix synthesis technique and its microstrip implementation," *IEEE Trans. Microw. Theory Tech.*, vol. 58, no. 7, pp. 1840–1850, 2010.

[29] J. Lee and K. Sarabandi, "Design of triple-passband microwave filters using frequency transformations," *IEEE Trans. Microw. Theory Tech.*, vol. 56, no. 1, pp. 187–193, 2008.

[30] K. S. Chin, J. H. Yeh, and S. H. Chao, "Compact dual-band bandstop filters using stepped-impedance resonators," *IEEE Microw. Compon. Lett.*, vol. 17, no. 12, pp. 849–851, 2007.

[31] Z. Ma, K. Kikuchi, Y. Kobayashi, T. Anada, and G. Hagiwara, "Novel microstrip dual-band bandstop filter with controllable dual-stopband response," *Proc. Asia-Pacific Microw. Conf.*, pp. 1177–1180, 2006.

[32] J. Wang, H. Ning, L. Mao, and M. Li, "Miniaturized dual-band bandstop filter using defected microstrip structure and defected ground structure," *IEEE MTT-S Int. Microw. Symp. Dig.*, pp. 8–10, 2012.

[33] X. P. Chen, K. Wu, and Z. L. Li, "Dual-band and triple-band substrate integrated waveguide filters with chebyshev and quasi-elliptic responses," *IEEE Trans. Microw. Theory Tech.*, vol. 55, no. 12, pp. 2569–2578, 2007.

[34] A. El Mostrah, B. Potelon, E. Rius, C. Quendo, and J.-F. Favennec, "C-band cross-coupled SIW filter using a novel topology of electric coupling," *Proc. Eur. Microw. Conf.*, pp. 188–191, 2010.

[35] W. Shen, L. S. Wu, X. W. Sun, W. Y. Yin, and J. F. Mao, "Novel substrate integrated waveguide filters with mixed cross coupling (MCC)," *IEEE Microw. Compon. Lett.*, vol. 19, no. 11, pp. 701–703, 2009.

[36] K. Gong, W. Hong, Y. Zhang, P. Chen, and C. J. You, "Substrate integrated waveguide quasi-elliptic filters with controllable electric and magnetic mixed coupling," *IEEE Trans. Microw. Theory Tech.*, vol. 60, no. 10, pp. 3071–3078, 2012.

[37] X. P. Chen and K. Wu, "Substrate integrated waveguide cross-coupled filter with negative coupling structure," *IEEE Trans. Microw. Theory Tech.*, vol. 56, no. 1, pp. 142–149, 2008.

[38] S. W. Wong, K. Wang, Z. N. Chen, and Q. X. Chu, "Design of millimeter-wave bandpass filter using electric coupling of substrate integrated waveguide (SIW)," *IEEE Microw. Compon. Lett.*, vol. 24, no. 1, pp. 26–28, 2014.

[39] B. Potelon, J. F. Favennec, C. Quendo, E. Rius, C. Person, and J. C. Bohorquez, "Design of a substrate integrated waveguide (SIW) filter using a novel topology of coupling," *IEEE Microw. Compon. Lett.*, vol. 18, no. 9, pp. 596–598, 2008.

[40] Z. Kordiboroujeni and J. Bornemann, "Designing the width of substrate integrated waveguide structures," *IEEE Microw. Compon. Lett.*, vol. 23, no. 10, pp. 518–520, 2013.

[41] L. Szydlowski, A. Lamecki, and M. Mrozowski, "Coupled-resonator waveguide filter in quadruplet topology with frequency-dependent coupling - A design based on coupling matrix," *IEEE Microw. Compon. Lett.*, vol. 22, no. 11, pp. 553–555, 2012.

[42] L. Szydlowski, A. Lamecki, and M. Mrozoowski, "Coupled-resonator filters with frequency-dependent couplings: Coupling matrix synthesis," *IEEE Microw. Compon. Lett.*, vol. 22, no. 6, pp. 312–314, 2012.

[43] L. Szydlowski, N. Leszczynska, and A. Lamecki, "A substrate integrated waveguide (SIW) bandpass filter in a box configuration with frequency-dependent coupling," *IEEE Microw. Compon. Lett.*, vol. 22, no. 11, pp. 556–558, 2012.

[44] M. Mokhtaari, J. Bornemann, K. Rambabu, and S. Amari, "Coupling-matrix design of dual and triple passband filters," *IEEE Trans. Microw. Theory Tech.*, vol. 54, no. 11, pp. 3940–3945, 2006.

[45] A. Williams, "A four-cavity elliptic waveguie filter," *IEEE Trans. Microw. Theory Tech.*, vol. 18, no. 12, pp. 1109–1114, 1970.

[46] A. Atia and A. Williams, "Narrow-bandpass waveguide filters," *IEEE Trans. Microw. Theory Tech.*, vol. 20, no. 4, pp. 258–265, 1972.

[47] V. E. Boria and B. Gimeno, "Waveguide filters for satellites," *IEEE Microw. Mag.*, vol. 8, no. 5, pp. 60–70, 2007.

[48] S. Bastioli, "Nonresonating mode waveguide filters," *IEEE Microw. Mag.*, vol. 12, no. 6, pp. 77–86, 2011.

[49] F. Arndt, T. Duschak, U. Papziner, and P. Rolappe, "Asymmetric iris coupled cavity filters with stopband poles," *IEEE MTT-S Int. Microw. Symp. Dig.*, pp. 215–218, 1990.

[50] S. Amari, U. Rosenberg, and J. Bornemann, "Singlets, cascaded singlets, and the nonresonating node model for advanced modular design of elliptic filters," *IEEE Microw. Compon. Lett.*, vol. 14, no. 5, pp. 237–239, 2004.

[51] S. Amari and U. Rosenberg, "New in-line dual- and triple-mode cavity filters with nonresonating nodes," *IEEE Trans. Microw. Theory Tech.*, vol. 53, no. 4, pp. 1272–1279, 2005.

[52] S. Amari and G. Macchiarella, "Synthesis of inline filters with arbitrarily placed attenuation poles by using nonresonating nodes," *IEEE Trans. Microw. Theory Tech.*, vol. 53, no. 10, pp. 3075–3081, 2005.

[53] W. Shen, X.-W. Sun, W.-Y. Yin, J.-F. Mao, and Q.-F. Wei, "A novel single-cavity dual mode substrate integrated waveguide filter with non-resonating node," *IEEE Microw. Compon. Lett.*, vol. 19, no. 6, pp. 368–370, 2009.

[54] S. Bastioli, C. Tomassoni, and R. Sorrentino, "A new class of waveguide dual-mode filters using TM and nonresonating modes," *IEEE Trans. Microw. Theory Tech.*, vol. 58, no. 12, pp. 3909–3917, 2010.

[55] P. Milano, "Direct synthesis of prototype filters with non-resonating nodes," *Proc. Eur. Microw. Conf.*, pp. 305–308, 2004.

[56] R. Wu, S. Amari, and U. Rosenberg, "Cross-coupled microstrip band reject filters with non-resonating nodes," *IEEE MTT-S Int. Microw. Symp. Dig.*, pp. 585–587, 2005.

[57] J. Malherbe, *Microwave Transmission Line Filters*. Norwood: Artech House Inc, 1979.

[58] W. H. Tu and K. Chang, "Compact microstrip bandstop filter using open stub and spurline," *IEEE Microw. Compon. Lett.*, vol. 15, no. 4, pp. 268–270, 2005.

[59] A. Görür, C. Karpuz, E. Güntürkün, M. Urhan, and A. K. Görür, "Design of microstrip bandstop filter with adjustable wide passband using folded open-circuited stub resonators," *Proc. Asia-Pacific Microw. Conf.*, pp. 15–18, 2009.

[60] P. S. Zhang, N. Y. Zhang, Q. X. Chu, and F. C. Chen, "Design of ultra-wideband bandstop filter using defected ground structure," *IET Electronics Lett.*, vol. 49, no. 16, pp. 1010–1011, 2013.

[61] A. Batmanov, E. Burte, and R. Mikuta, "Design of coplanar bandstop filter based on open-Loop-ring resonator and DGS for WLAN and UWB applications," *Proc. Eur. Microw. Conf.*, pp. 1123–1126, 2012.

[62] X. Chen, W. Hong, Z. Hao, and K. Wu, "Substrate integrated waveguide quasi-elliptic filter using extracted-pole technique," *Proc. Asia-Pacific Microw. Conf.*, pp. 5–7, 2005.

[63] M. K. Mandal, K. Divyabramham, and V. K. Velidi, "Compact wideband bandstop filter with five transmission zeros," *IEEE Microw. Compon. Lett.*, vol. 22, no. 1, pp. 4–6, 2012.

[64] Q.-X. Chu and L.-L. Qiu, "Sharp-rejection bandstop filter based on signal interference technique integrating with conventional open stubs," *IEEE MTT-S Int. Microw. Symp. Dig.*, pp. 31–33, 2014.

[65] W. Feng, W. Che, S. Shi, and J. Zhou, "Compact dual-wideband bandstop filter based on transversal signal-interference concept," *Proc. Asia-Pacific Microw. Conf.*, pp. 505–507, 2012.

[66] G. Eryilmaz, G. Elif, A. Gorur, and K. Ceyhun, "Dual-mode microstrip bandstop filters," *Proc. Asia-Pacific Microw. Conf.*, pp. 1–4, 2008.

[67] J. H. Lee, Y. C. Oh, and N. H. Myung, "A novel compact microstrip bandstop filter based on complementary split-ring resonators," *Proc. Asia-Pacific Microw. Conf.*, pp. 1435–1438, 2006.

[68] L. Slu and D. Lou, "The design of a novel 2.4 GHz microstrip stopband filter with PBG structure," *Proc. Asia-Pacific Microw. Conf.*, pp. 139–141, 2004.

[69] M. Y. Hsieh and S. M. Wang, "Compact and wideband microstrip bandstop filter," *IEEE Microw. Compon. Lett.*, vol. 15, no. 7, pp. 472–474, 2005.

[70] H. Shaman and J. S. Hong, "Wideband bandstop filter with cross-coupling," *IEEE Trans. Microw. Theory Tech.*, vol. 55, no. 8, pp. 1780–1785, 2007.

[71] M. K. Mandal, K. Divyabramham, and S. Sanyal, "Compact, wideband bandstop filters with sharp rejection characteristic," *IEEE Microw. Compon. Lett.*, vol. 18, no. 10, pp. 665–667, 2008.

[72] M. A. Sánchez-Soriano, G. Torregrosa-Penalva, and E. Bronchalo, "Compact wideband bandstop filter with four transmission zeros," *IEEE Microw. Compon. Lett.*, vol. 20, no. 6, pp. 313–315, 2010.

[73] K. Divyabramham, M. K. Mandal, and S. Sanyal, "Sharp-rejection wideband bandstop filters," *IEEE Microw. Compon. Lett.*, vol. 18, no. 10, pp. 662–664, 2008.

[74] L. B. Minakova and L. A. Rud, "Waveguide bandstop filters based on partially filled H-plane stubs," *Proc. Microw., Radar Wirel. Comm.*, pp. 77–80, 2002.

[75] W.-H. Tu and K. Chang, "Compact second harmonic-suppressed bandstop and bandpass filters using open stubs," *IEEE Trans. Microw. Theory Tech.*, vol. 54, no. 6, pp. 2497–2502, 2006.

[76] J. Malherbe and C. Reid, "Double resonant stub bandstop filter with pseudo-elliptic response," *IET Electronics Lett.*, vol. 46, no. 7, pp. 508–509, 2010.

[77] J. Malherbe, "Pseudo-elliptic bandstop filter with 1:2:3 harmonic ratio stubs," *IET Electronics Lett.*, vol. 49, no. 2, pp. 130–132, 2013.

[78] A. Görür and C. Karpuz, "Uniplanar compact wideband bandstop filter," *IEEE Microw. Compon. Lett.*, vol. 13, no. 3, pp. 114–116, 2003.

[79] K. Wu, "State-of-the-art and future perspective of substrate integrated circuits (SIC)," *Work. Notes Substrate Integr. Circuits, IEEE MTT-S Int. Microw. Symp*, pp. 1–40, 2010.

[80] H. Grubinger, H. Barth, and R. Vahldieck, "An LTCC-based 35-GHz substrate-integrated-waveguide bandpass filter," *IEEE MTT-S Int. Microw. Symp. Dig.*, pp. 1605–1608, 2009.

[81] Z. M. Liu, J. A. Ruiz-Cruz, C. Wang, and K. A. Zaki, "An extremely wideband ridge waveguide filter," *IEEE MTT-S Int. Microw. Symp. Dig.*, pp. 615–618, 2004.

[82] F. Vanin, E. Wollack, K. Zaki, and D. Schmitt, "Polarization-preserving quadruple-ridge waveguide filter and four-fold symmetric transformer," *IEEE MTT-S Int. Microw. Symp. Dig.*, pp. 127–130, 2006.

[83] J. A. Ruiz-Cruz, Y. Zhang, K. A. Zaki, A. J. Piloto, and J. Tallo, "Ultra-wideband LTCC ridge waveguide filters," *IEEE Microw. Compon. Lett.*, vol. 17, no. 2, pp. 115–117, 2007.

[84] W. Che, C. Li, P. Russer, and Y. L. Chow, "Propagation and band broadening effect of planar integrated ridged waveguide in multilayer dielectric substrates," *IEEE MTT-S Int. Microw. Symp. Dig.*, pp. 217–220, 2008.

[85] M. Bozzi, S. Winkler, and K. Wu, "Broadband and compact ridge substrate-integrated waveguides," *IET Microw. Antennas Propag.*, vol. 4, no. 11, pp. 1965–1973, 2010.

[86] J. Rhodes and R. Cameron, "General extracted pole synthesis technique with applications to low-loss TE011 mode filters," *IEEE Trans. Microw. Theory Tech.*, vol. 28, no. 9, pp. 1018–1028, 1980.

[87] R. J. Cameron, "General prototype network synthesis methods for microwave filters," *ESA J.*, vol. 6, pp. 193–206, 1982.

[88] S. Amari and U. Rosenberg, "Synthesis and design of novel in-line filters with one or two real transmission zeros," *IEEE Trans. Microw. Theory Tech.*, vol. 52, no. 5, pp. 1464–1478, 2004.

[89] G. Macchiarella, "Synthesis of an in-line prototype filter with two transmission zeros without cross couplings," *IEEE Microw. Compon. Lett.*, vol. 14, no. 1, pp. 19–21, 2004.

[90] J. Montejo-Garai, J. Ruiz-Cruz, J. Rebollar, M. Padilla-Cruz, A. Onoro-Navarro, and I. Hidalgo-Carpintero, "Synthesis and design of in-line N-order filters with N real transmission zeros by means of extracted poles implemented in low-cost rectangular H-plane waveguide," *IEEE Trans. Microw. Theory Tech.*, vol. 53, no. 5, pp. 1636–1642, 2005.

[91] U. Rosenberg and S. Amari, "A novel band-reject element for pseudoelliptic bandstop filters," *IEEE Trans. Microw. Theory Tech.*, vol. 55, no. 4, pp. 742–746, 2007.

[92] J.-S. Hong, "Reconfigurable planar filters," *IEEE Microw. Mag.*, vol. 10, no. 6, pp. 73–83, 2009.

[93] S. Darfeuille, J. Lintignat, R. Gómez-García, Z. Sassi, B. Barelaud, L. Billonnet, B. Jarry, H. Marie, and P. Gamand, "Silicon-integrated differential bandpass filters based on recursive and channelized principles and methodology to compute their exact noise figure," *IEEE Trans. Microw. Theory Tech.*, vol. 54, no. 12, pp. 4381–4395, 2006.

[94] B. Yassini, M. Yu, and B. Keats, "A Ka-band fully tunable cavity filter," *IEEE Trans. Microw. Theory Tech.*, vol. 60, no. 12, pp. 4002–4012, 2012.

[95] I. Hunter and J. Rhodes, "Electronically tunable microwave bandpass filters," *IEEE Trans. Microw. Theory Tech.*, vol. 30, no. 9, pp. 1354–1360, 1982.

[96] S. Courrèges, Y. Li, Z. Zhao, K. Choi, A. Hunt, and J. Papapolymerou, "A low loss X-band quasi-elliptic ferroelectric tunable filter," *IEEE Microw. Compon. Lett.*, vol. 19, no. 4, pp. 2009–2011, 2009.

[97] G. M. Rebeiz, K. Entesari, I. C. Reines, S. J. Park, M. A. El-Tanani, A. Grichener, and A. R. Brown, "Tune in to RF MEMS," *IEEE Microw. Mag.*, vol. 10, no. 6, pp. 55–72, 2009.

[98] R. Gomez-Garcia, M.-A. Sanchez-Soriano, K.-W. Tam, and Q. Xue, "Flexible filters," *IEEE Microw. Mag.*, vol. 15, no. 5, pp. 43–54, 2014.

[99] A. Deleniv, S. Abadei, and S. Gevorgian, "Tunable ferroelectric filter-phase shifter," *IEEE MTT-S Int. Microw. Symp. Dig.*, pp. 1267–1270, 2003.

[100] T. Yun and K. Chang, "Piezoelectric-transducer-controlled tunable microwave circuits," *IEEE Trans. Microw. Theory Tech.*, vol. 50, no. 5, pp. 1303–1310, 2002.

[101] C. Lugo Jr, D. Thompson, and J. Papapolymerou, "Reconfigurable bandpass filter with variable bandwidth at 5.8 GHz using a capacitive gap variation technique," *Proc. Eur. Microw. Conf.*, pp. 923–926, 2003.

[102] M. Sánchez-Renedo, R. Gómez-Garcia, J. I. Alonso, and C. Briso-Rodríguez, "Tunable combline filter with continuous control of center frequency and bandwidth," *IEEE Trans. Microw. Theory Tech.*, vol. 53, no. 1, pp. 191–199, 2005.

[103] C. Rauscher, "Reconfigurable bandpass filter with a three-to-one switchable passband width," *IEEE Trans. Microw. Theory Tech.*, vol. 51, no. 2, pp. 573–577, 2003.

[104] S. Sirci and J. D. Mart, "Analog tuning of compact varactor-loaded combline filters in substrate integrated waveguide," *Proc. Eur. Microw. Conf.*, pp. 257–260, 2012.

[105] E. J. Naglich, D. Peroulis, and W. J. Chappell, "Wide spurious free range positive-to-negative inter-resonator coupling structure for reconfigurable filters," *IEEE MTT-S Int. Microw. Symp. Dig.*, pp. 1–4, 2013.

[106] F. Mira, J. Mateu, S. Member, and C. Collado, "Mechanical tuning of substrate integrated waveguide resonators," *IEEE Microw. Compon. Lett.*, vol. 22, no. 9, pp. 447–449, 2012.

[107] H. Kang, S. Sam, I.-J. Hyun, C.-W. Baek, and S. Lim, "Silicon-based substrate-integrated waveguide-based tunable band-pass filter using interdigital MEMS capacitor," *Proc. Asia-Pacific Microw. Conf.*, pp. 456–458, 2013.

[108] R. Boylestad, L. Nashelsky, and F. Monssen, *Electronic Devices and Circuit Theory*, New Jersey: Prentice Hall International Inc., 2006.

[109] K. Entesari, A. P. Saghati, V. Sekar, and M. Armendariz, "Tunable SIW structures: antennas, VCOs, and filters," *IEEE Microw. Mag.*, vol. 16, no. 5, pp. 34–54, 2015.

[110] J. Lee, E. J. Naglich, and W. J. Chappell, "Frequency response control in frequency-tunable bandstop filters," *IEEE Microw. Compon. Lett.*, vol. 20, no. 12, pp. 669–671, 2010.

[111] K. Lee, T.-H. Lee, C.-S. Ahn, Y.-S. Kim, and J. Lee, "Reconfigurable dual-stopband filters with reduced number of couplings between a transmission line and resonators," *IEEE Microw. Compon. Lett.*, vol. 25, no. 2, pp. 106–108, 2015.

[112] S. Saeedi, J. Lee, and H. H. Sigmarsson, "Novel coupling matrix synthesis for single-layer substrate-integrated evanescent-mode cavity tunable bandstop filter design," *IEEE Trans. Microw. Theory Tech.*, vol. 63, no. 12, pp. 3929–3938, 2015.

[113] A. Anand and X. Liu, "Capacitively tuned electrical coupling for reconfigurable coaxial cavity bandstop filters," *IEEE MTT-S Int. Microw. Symp. Dig.*, pp. 9–11, 2015.

[114] A. R. Brown, P. Blondy, and G. M. Rebeiz, "Microwave and millimeter-wave high-Q micromachined resonators," *Int. J. RF Microw. Comput. Aided Eng.*, vol. 9, no. 4, pp. 326–337, 1999.

[115] W. Deal, "Coplanar waveguide basics for MMIC and PCB design," *IEEE Microw. Mag.*, vol. 9, no. 4, pp. 120–133, 2008.

[116] X. Wu, I. Awai, Z. Yan, K. Wada, and T. Moriyoshi, "Quality factors of coplanar waveguide resonators," *Proc. Asia-Pacific Microw. Conf.*, pp. 670–673, 1999.